PROCEEDINGS BOOK OF
THE10th INTERCONTINENTAL GEOINFORMATION DAYS
29 - 30 NOVEMBER 2025
Tehran, IRAN

MERSIN UNIVERSITY - ENGINEERING FACULTY
DEPARTMENT OF GEOMATICS ENGINEERING

Intercontinental Geoinformation Days

ISBN: 978-625-5604-32-3

The proceedings of the
10th Intercontinental Geoinformation Days

Editor-in-Chief

Prof. Dr. Murat Yakar

Editors

Assoc. Prof. Dr. Mohammadreza Jelokhani-Niaraki

Assoc. Prof. Dr. Meysam Argany

Prof. Dr. Saeid Hamzeh

Assoc. Prof. Dr. Najmeh Neysani Samany

ISBN: 978-625-5604-32-3

Tehran, 30.12.2025

Honor Board

Atilla TOROS – Governor of Mersin Province
Prof. Dr. Erol YAŞAR – Rector of Mersin University
Prof. Dr. Ali ÖZEN – Rector of Tarsus University
Prof. Dr. Ömer ARIÖZ – Rector of Toros University
Hakan GEDİKLİ – Director of Turkish Land Registry and Cadastre
Prof. Dr. Diane DUMASHIE– FIG President
Prof. Dr. Lena Halounová – ISPRS President
Prof. Dr. Chryssy POTSIOU – FIG Honorary President

Organizing Committee

Mersin University – Faculty of Engineering – Department of Geomatics Engineering
University of Tehran - Faculty of Geography - Department of Remote Sensing and GIS

Prof. Dr. Murat Yakar – Conference Chairman
Assoc. Prof. Mohammadreza Jelokhani-Niaraki - Co-Chairman
Assoc. Prof. Dr. Meysam Argany
Assoc. Prof. Dr. Saeid Hamzeh
Assoc. Prof. Dr. Najmeh Neysani Samany
Prof. Dr. Khalil Valizadeh Kamran
Asst. Prof. Dr. Fatma Bünyan Ünel
Asst. Prof. Dr. Lütfiye Kuşak
Dr. Bahare Sadat Mousavi
Erfan Motaghiyan
Ali Sadeghi
Mina Azimipanah
Avin Meysami
Mohadeseh Mohammadi
Atefeh Hesaraki
Mahdi Sheybani Amin

Scientific Committee

Prof. Dr. Seyed Kazem Alavi PANAH - University of Tehran, IRAN
Assoc. Prof. Dr. Farshad AMIRASLANI- University of Tehran, IRAN
Assoc. Prof. Dr. Majid Kiavarz MOGHADDAM- University of Tehran, IRAN
Assoc. Prof. Dr. Yousef ERFANIFARD- University of Tehran, IRAN
Assoc. Prof. Dr. Ata a. KAKROODI- University of Tehran, IRAN
Assoc. Prof. Dr. Saeid HAMZEH- University of Tehran, IRAN
Assoc. Prof. Dr. Sara ATTARCHI - University of Tehran, IRAN
Assoc. Prof. Dr. Shirin MOHAMMADKHAN- University of Tehran, IRAN
Assoc. Prof. Dr. Saeed BAZGEER - University of Tehran, IRAN
Prof. Dr. Abdurrahman EYMEN – Erciyes University, TURKIYE
Prof. Dr. Alexander SAGAYDAK – State University of Land Use Planning, RUSSIA
Prof. Dr. Alias Abdul RAHMAN – Universiti Teknologi Malaysia (UTM), MALAYSIA
Prof. Dr. Andreas GEORGOPOULOS – National Technical University of Athens, GREECE
Prof. Dr. Ariel BLANCO – University of Philippines at Diliman, PHILIPPINES
Prof. em. Dr.-Ing. Dr.h.c. Armin GRÜN – ETH Zürich, SWITZERLAND
Prof. Dr. Ashutosh MOHANTY – Shoolini University, INDIA
Prof. Dr. Aydın ÜSTÜN – Kocaeli University, TURKIYE
Prof. Dr. Aziz ŞİŞMAN – Ondokuz Mayıs University, TURKIYE the
Prof. Dr. Bashkim IDRIZI – University of Prishtina, KOSOVO

Assoc. Prof. Dr. Berk ANBAROĞLU – Hacettepe University, TURKIYE
Assoc. Prof. Dr. Beyhan KOCADAĞİSTAN – Atatürk University, TURKIYE
Assoc. Prof. Dr. Erman ŞENTÜRK – Kocaeli University, TURKIYE
Assoc. Prof. Dr. Esra TEKDAL YILMAZ – Nicholls State University, USA
Assoc. Prof. Dr. Faruk POLATCAN – Sinop University, TURKIYE
Assoc. Prof. Dr. Gordana KAPLAN – Eskisehir Technical University, TURKIYE
Assoc. Prof. Dr. Khalil Valizadeh KAMRAN – University of Tabriz, IRAN
Assoc. Prof. Dr. Lyubka PASHOVA – Bulgarian Academy of Sciences, BULGARIA
Assoc. Prof. Dr. Mahmut Oğuz SELBESOĞLU – Istanbul Technical University, TURKIYE
Assoc. Prof. Dr. Najmeh Neysani SAMANY– University of Tehran, IRAN
Assoc. Prof. Dr. Onur ER – Düzce University, TURKIYE
Assoc. Prof. Dr. Serdar BİLGİ – Istanbul Technical University, TURKIYE
Assoc. Prof. Dr. Süleyman Sefa BİLGİLİOĞLU – Aksaray University, TURKIYE
Assoc. Prof. Dr. Şükran YALPIR – Konya Technical University, TURKIYE
Assoc. Prof. Dr. Volkan YILMAZ – Artvin Çoruh University, TURKIYE
Asst. Prof. Dr. Hamid Reza Ghafarian MALAMIRI– Yazd University, IRAN
Asst. Prof. Dr. Hossein AGHIGHI– Shahid Beheshti University
Asst. Prof. Dr. Jorge ROCHA – University of Lisbon, PORTUGAL
Asst. Prof. Dr. Kemal ÇELİK – Gümüşhane University, TURKIYE
Asst. Prof. Dr. Khalid MAHMOOD – University of Punjab, PAKISTAN
Asst. Prof. Dr. Mehrdad JEIHOUNI – University of Tabriz, IRAN
Asst. Prof. Dr. Sadra KARIMZADEH – University of Tabriz, IRAN
Asst. Prof. Dr. Mustafa Utkan DURDAĞ – Artvin Çoruh University, TURKIYE
Asst. Prof. Dr. Mustafa ÜSTÜNER – Artvin Çoruh University, TURKIYE
Asst. Prof. Dr. Nizar POLAT – Harran University, TURKIYE
Asst. Prof. Dr. Osman Sami KIRTILOĞLU – İzmir Katip Çelebi University, TURKIYE
Asst. Prof. Dr. Samira ABUSHOVA – Azerbaijan National Academy of Science, AZERBAIJAN
Asst. Prof. Dr. Subija IZEIROSKI – Geo-SEE Institute, NORTH MACEDONIA **Asst.**
Prof. Dr. Surendra Pal SINGH – Wollega University, ETHIOPIA
Asst. Prof. Dr. Tae-Suk BAE– Sejong University, REPUBLIC OF KOREA
Asst. Prof. Dr. Tirthankar BANERJEE – Banaras Hindu University, INDIA
Dr. Adamu BALA – China University of Geosciences, CHINA
Dr. Ali KESHAVARZI - University of Tehran, IRAN
Dr. Behnam KHORRAMI – 9 Eylul University, TURKIYE
Dr. Abdel Aziz ELFADALY – Nat. Auth. for Remote Sensing and Space Science, EGYPT
Dr. Abdul-Lateef BALOGUN – Universiti Teknologi Petronas (UTP), MALAYSIA
Dr. Artur GIL – University of the Azores, PORTUGAL
Dr. Ajoy DAS – Gujarat University, INDIA
Dr. Bayartungalag BATSAIKHAN – Chairwoman of Mongolian Geo-spatial Association, MONGOLIA
Dr. Cesar CAPINHA – University of Lisbon, PORTUGAL
Dr. Gojko NIKOLIC – University of Montenegro, MONTENEGRO
Dr. Ismail KABASHI – Angst, AUSTRIA
Dr. İsmail ÇOBAN – Artvin Çoruh University, TURKIYE
Dr. Narendra KUMAR – HNB Garhwal University, INDIA
Dr. Krishna Prasad BHANDARI– Tribhuvan University, NEPAL
Dr. MD Firoz KHAN – University of Malaya, MALAYSIA
Dr. Muhammad IMZAN BIN HASSAN – Universiti Teknologi Malaysia, MALAYSIA
Dr. Eng. Colonel Altan YILMAZ – Turkish Gen. Directorate of Mapping, TURKIYE
Dr. Xin HONG - Koç University, TURKIYE
M.Sc. R.S. AJIN – Dpt. Of Disaster Management, Govt. Of Kerala, INDIA
M.Sc. Ochirkhuyag LKHAMJAV – Mongolian Geo-spatial Association, MONGOLIA
M.Sc. Mohamed Ahmed Badawi ATTALLAH – Higher Institute of Literary Studies, EGYPT
M.Sc. Abubakar BELLO – Islamic Learning Centre, NIGERIA
Dereje SUFA – Wollega University, ETHIOPIA
Byeong-Hyeok YU – Korean Soc. of Environment & Ecology, REPUBLIC OF KOREA
International Association of Turkish Literature Culture Education (TEKE Derneği)

IGD-10 Oral Presentations

Designing a Spatial-Climatic Resilience Framework for The Tehran Metropolitan Area: A Meta-Method Approach

Somayeh Ahani[1], Zahra Pahlavan[2]
[1] Assistant Professor of Urban Planning, Faculty of Fine Arts, University of Tehran, Somaye.ahani@ut.ac.ir
[2] Master's Student of Regional Planning, University of Tehran, zahra.pahlavan@ut.ac.ir

Abstract

The Tehran metropolitan area faces escalating spatio-climatic pressures driven by multi-hazard conditions, institutional limitations, and persistent spatial inequalities. Existing resilience frameworks remain constrained by data-spatial, institutional-governance, and prospective-analytical gaps, limiting their ability to support adaptive, evidence-based, and place-sensitive policymaking. Using a meta-methodological analysis, this study integrates spatial data analytics, institutional learning, and scenario-based foresight to develop a comprehensive four-level transdisciplinary framework for regional climate-resilience planning. The proposed architecture systematically bridges theory, data, and governance by translating climate scenarios into spatial decision layers and embedding continuous feedback cycles within institutional processes. By linking spatial analysis with foresight approaches and adaptive governance, the framework enhances the capacity to interpret complex risk dynamics, manage long-term uncertainties, and redesign policies accordingly. Overall, this model provides a scalable foundation for spatially explicit, adaptive, and equity-oriented resilience strategies, offering practical value for Tehran and other metropolitan regions confronting comparable climatic, spatial, and institutional challenges in an era of accelerating environmental change.

Keywords: Spatial–climatic resilience; Meta-methodology; Scenario-based foresight; Tehran metropolitan region; Adaptive governance.

1. Introduction

Over recent decades, the Tehran metropolitan area has evolved into a highly complex multi-hazard landscape, shaped by recurrent droughts, declining rainfall and groundwater, expanding heat islands, and land subsidence (IPCC, 2019; Almheiri et al., 2024). These trends reflect not only global climate change but also long-term patterns of unsustainable development, weak resource governance, and entrenched spatial inequalities, disproportionately affecting vulnerable groups and raising issues of climate and spatial justice (Fereshtehpour & Najafi, 2025; Byskov et al., 2019).

Although the literature on resilience and spatial planning is expanding, many existing frameworks rely on static indicators and linear or sectoral analyses, limiting their ability to capture the multi-causal interactions across climatic, spatial, and institutional systems (Wardekker, 2021; Laurien et al., 2022). Conversely, foresight and scenario-based methods can only become operational policy tools when integrated with spatial data and governance structures (Ritchey, 2022; Saritas et al., 2022). Meanwhile, advances in remote sensing, GIS, and climate big data have strengthened monitoring capacities, yet the absence of an integrative analytical logic prevents their translation into effective policy (Amani et al., 2020; Makokha et al., 2025).

At the governance level, research underscores the need for institutional learning, cross-level coordination, and participatory approaches to support adaptive policies (Pedde et al., 2025; Tschanz et al., 2022), while climate justice scholarship cautions against resilience strategies that reproduce inequalities (Pellerey et al., 2025).

Taken together, these insights show that Tehran's primary challenge is not the scarcity of data or tools but the lack of an integrative, transdisciplinary logic capable of simultaneously addressing:

1)Data-driven spatial analysis, 2) Institutional and justice-oriented assessment, 3) Scenario-based foresight.

Accordingly, this paper aims to develop a transdisciplinary framework for Tehran’s spatial-climatic resilience one that bridges theory, data, and policy and supports adaptive, equitable, and place-sensitive decision-making.

2. **Materials and Methods**

This research employs a Meta-Methodological Analysis approach; an approach that, instead of relying on a single method, focuses on the critical rethinking of the logic of knowledge production and the synergistic combination of methods (Afanasyev et al., 2014; Wardekker et al., 2020). This approach enables the integration of epistemological, methodological, and applied levels and is suitable for managing the complexity, uncertainty, and multiscalarity of urban–regional systems.

The research process was designed in five stages:

Stage One: Identification and compilation of frameworks. Through a systematic literature review of the past two decades, index-based resilience models and data-driven approaches including remote sensing, GIS, and Google Earth Engine were extracted, and a “current state methodological map” was developed (Amani et al., 2020; Garschagen et al., 2021).

Stage Two: Comparative Analysis and Methodological Critique. The frameworks were compared based on three axes: spatial-institutional coverage, climatic-systemic logic, and capacity for learning and foresight. The results showed that most frameworks lack an integrative logic among space, climate, and institutions, or tend to oversimplify the relationships.

Step Three: Deriving Synthesizing Principles. The following three principles were identified:

(1) Spatial Data-Driven (remote sensing + climatic indices + GIS),
(2) Institutional Learning (feedback, coordination, distributive justice),
(3) Adaptive Foresight (multiple scenarios, morphological analysis).

Step Four: Designing the Transdisciplinary Framework. The final framework was integrated across four domains:

1) Conceptual-Critical, 2) Prospective-Analytical, 3) Data-Driven-Spatial, 4) Learning-Institutional.
This taxonomy indicates that the proposed model is an open and dynamic architecture for linking theory, data, and governance.

Step Five: Monitoring, Learning, and Readjustment. In this step, spatial monitoring and impact assessment were combined with the readjustment of scenarios and decision rules to form a cycle of continuous learning and refinement.

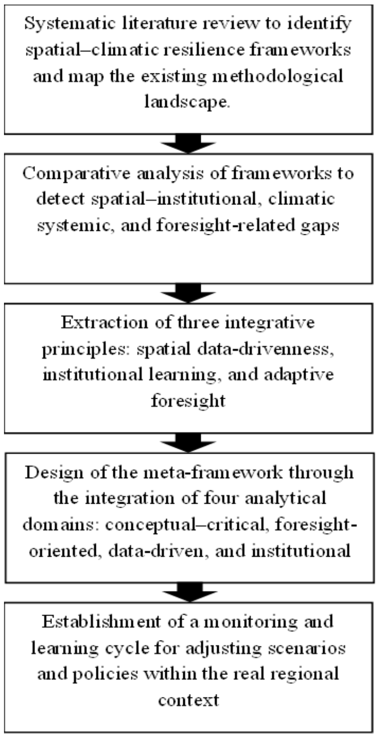

Figure 1: Meta-Methodological Research Cycle

3. Results

Findings from the meta-analysis show that existing spatial–climatic resilience frameworks, despite their diversity, are confronted with three core gaps in dealing with the structural, climatic, and institutional complexities of metropolitan Tehran:

1) a data-spatial gap, 2) an institutional-governance gap, and 3) a prospective–analytical gap.
These gaps, intensified by Tehran's multi-hazard profile, spatial inequalities, and limited institutional capacity, underscore the need for an integrated, multi-layered framework (Tyler & Moench, 2012; Wardekker, 2021).

The data–spatial gap reflects the absence of mechanisms to translate the high analytic potential of remote sensing, GIS, and GEE into spatially actionable decisions, leaving a disconnect between "spatial observability" and "spatial intervencibility" (Amani et al., 2020; Wilson et al., 2025). The institutional-governance gap stems from weak cross-level coordination, insufficient organizational learning, and limited attention to spatial justice, all of which constrain regional resilience (Pedde et al., 2025; Ordóñez Llancce et al., 2025). The prospective-analytical gap arises where climate scenarios remain poorly linked to local spatial and institutional contexts, and thus rarely evolve into usable policy tools (Ritchey, 2022; Saritas et al., 2022).
To address these gaps, the meta-analysis identifies three core axes as the foundation of the proposed framework:

(1) a data-spatial axis integrating remote sensing, climate indicators, and GIS into decision maps and spatial scenario assessments (Amani et al., 2020; Pomortseva et al., 2020);
(2) an institutional-governance axis aimed at strengthening decision-making capacity, cross-level coordination, institutional learning, and distributive justice (Pedde et al., 2025; Hoeben et al., 2025);

(3) a prospective–analytical axis focused on multi-scenario design, morphological analysis, and adaptive pathway assessment for managing long-term uncertainties (Ritchey, 2022; Afanasyev et al., 2014).

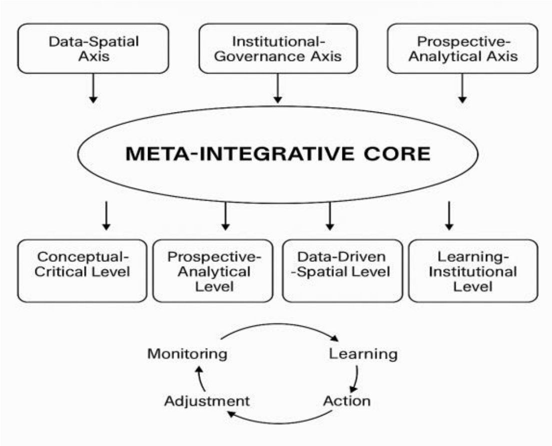

Figure 2: Integrative Conceptual Model for Spatial–Climatic Resilience

Building on these axes, an integrated four-level framework links issue diagnosis to policy design: (1) a conceptual-critical level explaining causal, spatial, and institutional mechanisms of risk production;
(2) a prospective-analytical level structuring uncertainty and generating alternative scenarios;
(3) a data-driven-spatial level translating scenarios into geospatial layers and assessing spatial interventions;
(4) a learning-institutional level organizing feedback, gradually adjusting policies, and enhancing adaptive capacity at the regional scale.

Overall, the proposed model is not a single method but a flexible analytical architecture that bridges data, institutions, and future-oriented analysis, integrating spatial analytics, climate scenarios, and multi-level governance into a dynamic learning cycle. This framework can support place-sensitive decision-making and adaptive policies in Tehran and comparable metropolitan regions (Global Commission on Adaptation, 2019; Chaiya, 2025).

4. Conclusion

The findings demonstrate that the climatic–spatial complexities of metropolitan Tehran cannot be addressed through single-method or purely technical approaches, as these remain descriptive and fail to capture the causal, institutional, and spatial mechanisms of risk production. Fuzzy-set assessment confirms that although GIS analyses, statistical models, and standalone climate scenarios each illuminate parts of the system, they lack the integrative logic needed to represent multi-factor, multi-scale dynamics. Accordingly, a meta-approach functions as an “analytical architecture” that connects theory, data, and policy by enabling the simultaneous integration of spatial analysis, foresight methods, and governance perspectives.

The proposed integrated framework structured around three core axes (data–spatial, institutional–governance, and future-oriented–analytical) and four operational levels offers a robust foundation for spatial development planning in Tehran. In water and drought management, this framework can synthesize remote sensing, climate indicators, and scenarios to produce spatial vulnerability maps and anticipate impacts across scales, supporting more realistic adaptive pathways. In governance, it can identify institutional capacities and weaknesses, informing policy reform and strengthening learning mechanisms.

More broadly, the results show that resilience in megacities is not primarily a technical challenge but an analytical and institutional one: resilience emerges when spatial data are incorporated into decision systems, scenarios are spatialized, and governance structures adjust policies through feedback. Thus, the meta-approach is not a substitute for existing methods but a coordinating logic that links diverse tools within a continuous learning cycle.

Ultimately, the study concludes that enhancing Tehran's spatio-climatic resilience requires shifting from sectoral, single-method approaches to hybrid, interdisciplinary frameworks capable of jointly explaining climatic processes, spatial structures, and institutional mechanisms. The proposed transdisciplinary framework provides a basis for place-sensitive policymaking, adaptive scenario design, and next-generation analytical tools, and should be further refined through empirical and policy-oriented research at the regional scale.

References

[1] Afanasyev, M., Cervantes, M., & Meissner, D. (2014). Towards FET concept: Pathway to evaluation of foresight effectiveness, efficiency and validity .National Research University Higher School of Economics.

[2] Almheiri, A., Montenegro, J. F., Ewane, E. B., & Mohan, M. (2024). Climate change hazards and the resilience of coastal cities in the Gulf Cooperation Council countries: A systematic review. City and Environment Interactions, 24, 100177. https://doi.org/10.1016/j.cacint.2024.100177

[3] Amani, M., Moghimi, A., Ghorbanian, A., Ahmadi, S. A., Kakooei, M., Mirmazloumi, S. M., Alizadeh Moghaddam, S. H., Mahdavi, S., Ghahremanloo, M., Parsian, S., Wu, Q., & Brisco, B. (2020). Google Earth Engine cloud computing platform for remote sensing big data applications: A comprehensive review. IEEE Journal of Selected Topics in Applied Earth Observations and Remote Sensing, 13, 5326–5350. https://doi.org/10.1109/JSTARS.2020.3021052

[4] Byskov, M. F., Hyams, K., Satyal, P., Anguelovski, I., Benjamin, L., Blackburn, S., Borie, M., Caney, S., Chu, E., Edwards, G., Fourie, K., Fraser, A., Heyward, C., Jeans, H., McQuistan, C., Paavola, J., Page, E., Pelling, M., Priest, S., … Venn, A. (2019). An agenda for ethics and justice in adaptation to climate change. Climate and Development, 13(1), 1–9. https://doi.org/10.1080/17565529.2019.1700774

[5] Chaiya, C. (2025). Empowering climate resilience: A people-centered exploration of Thailand's greenhouse gas emissions trading and sustainable environmental development through climate risk management in community forests. Heliyon, 11(2), e41844. https://doi.org/10.1016/j.heliyon.2025.e41844

[6] Fereshtehpour, M., & Najafi, M. R. (2025). Urban stormwater resilience: Global insights and strategies for climate adaptation. Urban Climate, 59, 102290. https://doi.org/10.1016/j.uclim.2025.102290

[7] Garschagen, M., Doshi, D., Reith, J., & Hagenlocher, M. (2021). Global patterns of disaster and climate risk: An analysis of the consistency of leading index-based assessments and their results. Climatic Change. https://doi.org/10.1007/s10584-021-03209-7

[8] Global Commission on Adaptation. (2019). Adapt now: A global call for leadership on climate resilience. Global Center on Adaptation. https://gca.org/reports/adapt-now-a-global-call-for-leadership-on-climate-resilience

[9] Hoeben, A. D., Lautrup, M., Willig, J., García-Jácome, S. P., Jankovský, M., Toppinen, A., Vuletić, D., Peltoniemi, M., & Stern, T. (2025). Stakeholder views of adaptation measures to improve climate resilience: Case study evidence from European wood value chains. Forest Policy and Economics, 170, 103379. https://doi.org/10.1016/j.forpol.2024.103379

[10 IPCC. (2019). Climate Change and Land. Cambridge University Press. https://doi.org/10.1017/9781009157988

[11 Laurien, F., Martin, J. G. C., & Mehryar, S. (2022). Climate and disaster resilience measurement: Persistent gaps in multiple hazards, methods, and practicability. Climate Risk Management, 36, 100443. https://doi.org/10.1016/j.crm.2022.100443

[12 Makokha, J. W., Barasa, P. W., & Khamala, G. W. (2025). Enhancing climate resilience: A data-driven north rift weather prediction system for real-time forecasting and agricultural decision support. Heliyon, 11(4), e42549. https://doi.org/10.1016/j.heliyon.2025.e42549

[13 Ordóñez Llancce, A., Lim, Y., Esteban, T. A. O., van Leeuwen, J., & Ninan, J. (2025). From silos to synergy: Integrated infrastructure design for climate resilience in Rotterdam. Climate Risk Management, 47, 100691. https://doi.org/10.1016/j.crm.2025.100691

[14 Pedde, S., Grendelman, R., Vinke-de Kruijf, J., Cumiskey, L., Hölscher, K., & McCullagh, D. (2025). Leveraging climate resilience capacities by (un)learning from transdisciplinary research projects. Climate Risk Management, 47, 100675. https://doi.org/10.1016/j.crm.2024.100675

[15 Pellerey, V., Torabi Moghadam, S., & Lombardi, P. (2025). A systematic review of justice integration to climate resilience: Current trends and future directions. Urban Climate, 59, 102250. https://doi.org/10.1016/j.uclim.2024.102250

[16 Pomortseva, O., Kobzan, S., Yevdokimov, A., & Kukhar, M. (2020). Use of geoinformation systems in environmental monitoring. E3S Web of Conferences, 166, 01002. https://doi.org/10.1051/e3sconf/202016601002

[17 Ritchey, T. (2022). General Morphological Analysis: An overview. Academia Letters, 4620. https://doi.org/10.20935/AL4620

[18 Saritas, O., Burmaoglu, S., & Ozdemir, D. (2022). The evolution of foresight: What evidence is there in scientific publications? Futures, 137, 102916. https://doi.org/10.1016/j.futures.2022.102916

[19 Tschanz, L., Arlot, M.-P., Philippe, F., Vidaud, L., Morin, S., Maldonado, E., George, E., & Spiegelberger, T. (2022). A transdisciplinary method, knowledge model and management framework for climate change adaptation in mountain areas. Regional Environmental Change, 22. https://doi.org/10.1007/s10113-021-01862-3

[20 Tyler, S., & Moench, M. (2012). A framework for urban climate resilience. Climate and Development, 4(4), 311–326. https://doi.org/10.1080/17565529.2012.745389

[21 Wardekker, A. (2021). Contrasting the framing of urban climate resilience. Sustainable Cities and Society, 75, 103258. https://doi.org/10.1016/j.scs.2021.103258

[22 Wardekker, A., Wilk, B., Brown, V., Uittenbroek, C., Mees, H., Driessen, P., Wassen, M., Molenaar, A., Walda, J., & Runhaar, H. (2020). A diagnostic tool for supporting policymaking on urban resilience. Cities, 101, 102691. https://doi.org/10.1016/j.cities.2020.102691

[23 Wilson, D. D., Tefera, G. W., & Ray, R. L. (2025). Application of Google Earth Engine to monitor greenhouse gases: A review. Data, 10(1), 8. https://doi.org/10.3390/data10010008

Applications of Integrating HBIM and GIS in Architectural Heritage

Somayeh. Sadrykia[1]
[1]University of Urmia,
s.sadrykia@urmia.ac.ir

Abstract

The integration of Historic Building Information Modelling (HBIM) and Geographic Information Systems (GIS) offers a powerful approach for documenting, analyzing, and managing heritage buildings and sites. HBIM provides accurate parametric and semantic representations of built environment, while GIS supplies storing, analyzing, and representing spatial context, environmental layers, and multiscale analysis capabilities. Integration these methods enables richer digital records, improved parametric modelling of complex geometries, enhanced multiscale visualization, and more informed and digital protection and conservation planning. This study reviews the principal applications reported in the literature, including digital documentation and cataloguing, parametric reconstruction of structures, platform design for conservation and protection, historic center management, heritage impact assessment, and vulnerability and risk analyses for hazards such as flooding, seismic events, and fire. Despite numerous case studies and specialized tools, existing research lacks a unified description that systematically categorizes the strategies, methods, aims and application domains of HBIM–GIS integration. To address this gap, the paper tried to synthesizes documented practices and classifies core applications according to purpose, scale and data requirements and their acquisition. By incorporating applications and proposing a structured taxonomy, the study provides a roadmap for researchers, conservators, and urban managers to adopt integrated HBIM–GIS workflows and to prioritize future research and capacity-building efforts.

Keywords: Geographic Information Systems, Historic Building Information Modelling, parametric representations.

1. Introduction

Innovative technologies and multidisciplinary approaches are recently emerging as valuable tools for supporting the conservation and regeneration of Cultural Heritage (CH) buildings[1].

The concept of the "Building Information Model was developed in the early 1990s [2], when Charles M. Eastman proposed the idea of the Building Product Model" [3] later termed "Building Information Modeling" (BIM). Since then, BIM has gained growing attention and widespread acceptance [4], reaching the built Cultural Heritage field as the so-called Heritage BIM (HBIM) in 2009 [5]. In recent years, the surge of digital survey research has expanded opportunities in this field.

Integrating GIS (Geographic Information System) and HBIM (Building Information Modeling) aims to combine the geometric and spatial information of buildings models with the spatial and geographical data of GIS. On the other hand, GIS-HBIM integration concentrates on historic protection, preservation and documentation of architectural heritage; historical documents, architectural surveys, and data of preservation, emphasizing on the unique historic aspects of structures, is used with the goal of preserving, protecting and managing architectural and urban heritage, ensuring that cultural and historical significance is mentioned, preserved and understood in their environmental context.

To provide suitable models, 3D maps developed based on point clouds are useful for producing comprehensive documentation for the current state of architectural and urban heritage. 3D models provide important information about heritage buildings from different perspectives and aspects and also at different levels of detail. for examples from material analysis to structural elements, which allows the development of simplified structural analysis [6].

This article aims to explore the potential of integrating HBIM and GIS highlighting its most importing applications. So the structure of this paper is as follows: First, the concepts and background related to digital modeling of buildings are explained. In the next section, the theoretical foundations, i.e. a general introduction to BIM, H-BIM and GIS approaches, are explained. Then, the integration of these two main platforms and their differences and distinctions are clarified. Next, the most important data extraction strategies and integration methods are discussed. Finally, in the results section, the most important applications of this integration are presented.

2.Material and Methods

2.1. Digital modelling of constructions

A complete three-dimensional model can offer valuable information about materials and geometric aspects of the structural elements. This may constitute a first approach to estimating tensional states in the whole structure, permitting to develop simplified structural analysis [7] as well as roughly estimate the energy needed to activate diverse mechanisms of collapse, e.g., partial or global façade overturning. Once a simple model is obtained (i.e., a general urban model), the single entities can be enhanced with further surveys and detailing. This might permit to perform a first contact study of the elements that have been identified as the critical ones. Such elements might be further assessed through BIM modelling and even reaching the design of accurate finite element models. This capacity permits to have a phased project in which some parts are more detailed than others[8].

2.1.1.BIM & HBIM approach

Building Information Modelling (BIM) is an integrated process based on creating digital models that represent a building through its entire lifecycle, by containing and relating different layers of information. Models are mostly composed of parametric instances and objects that incorporate reliable information from various sources, able to be managed by an interdisciplinary team [9]. For this reason, BIM models constitute a shared tool for several professionals that work on the same project others [8].The work of several specialists in the same model is possible because of the capacity of semantic enrichment, in which a determinate entity (namely components in a model) can store different layers of information meant for different operators. This also makes possible the interoperability of the same model with different platforms. Most of this semantical enrichment may be found in collective libraries that are continuously updated [10]. BIM methodology is useful for modelling existing entities as well, such as historic buildings, permitting to document and analyses their current situation and to support future interventions. The adaptation of BIM methodology for representing the numerous singularities of the historic buildings led to the development of the so-called Historic Building Information Methodology (or HBIM), a term proposed by Murphy *et al*. (2009) [8].

HBIM assumes the use of digital scanning and involves three main stages: data collection, processing, and modeling.

Data collection is primarily conducted through Terrestrial Laser Scanning (TLS) and Unmanned Aerial Vehicles (UAVs). Photogrammetry techniques using UAV imagery are particularly advantageous when combined with point clouds generated by TLS, as demonstrated in studies by Dore and Murphy (2012), Trisyanti et al. (2019) and Suwardhi et al. (2016) [1].

2.1.2. Geographic Information Systems (GIS) approach

Geographic Information System (GIS) tools are a particular case of databases that works with geographically referenced data [11] GIS tools allow relating spatial coordinates with several layers of attributes, permitting to develop multiple mappings in a unified coordinated and referenced framework. GIS tools are collections of information about the real world, integrating semantic and geometric data for its analysis and applications [12].

2.2. Integration of GIS and HBIM

GIS and BIM approaches have conceptually differences in their origins but there is an increasing interest in their interoperability. Since HBIM models are a particular case of BIM, the generalities for their integration in a GIS environment would be applicable for both. However, it is important to keep in mind that HBIM models can represent physical decays that might be related to multiple environmental phenomena, such as water flows, wind, solar incidences or presence of vegetation, for example. Hence, the generation of proper links between environmental information in GIS databases and specific decays in HBIM models suggest a promising opportunity for the assessment and diagnosis of vulnerabilities, finding valuable it is possible to insert simplified BIM entities in GIS models. Nevertheless, those simplified BIM models can be linked with more complex representation (as external references), through a controlled decrease in their level of detail [8]. Examples of integration, showing that the HBIM-GIS integration process often involves filtering data to ensure that only the most relevant information is transferred. For example, architects may prioritize detailed geometric and material information, while conservators and archaeologists focus on historical attributes. Engineers, on the other hand, may require structural data [13]. The effective integration of BIM data into a GIS environment depends not only on the accuracy of the data transfer but also on the ability of the GIS to manage and visualize this information appropriately. The domain of a BIM model within a GIS environment means that essential geometric and semantic information can be accessed and manipulated with precision, ensuring that the full potential of the BIM model is realized within the broader territorial context offered by the GIS [13].

GIS-HBIM integration, on the other hand, emphasizes historic preservation, documentation, and protection of historic buildings; it uses historical documents, architectural surveys, and preservation data, focusing on the unique aspects of historic structures, with the goal of protecting, preserving, and managing heritage buildings, ensuring that their historical and cultural significance is preserved and understood in their environmental context [6].

2.2.1. Differences of two platforms: GIS & HBIM

One of the most important differences that must be taken into account when working between BIM and GIS platforms is the level of detail that each system can represent and handle [8].
HBIM focuses on the micro scale of individual buildings, GIS addresses the macro scale of the territory. Together, these approaches facilitate the creation of a database that combines geo-referenced HBIM information, adapting the application from the micro to the macro scale, as proposed by Murphy et al. (2019) [13].

While BIM and HBIM models are intended to represent a building as accurate as possible, GIS copes with larger scales and, consequently, with lower levels of accuracy. There exist, however, a normalized index where BIM, HBIM and GIS (among others) tools may be framed to share information [14].

2.3. Strategies of data collection

The most recent and promising techniques for urban and architectonic surveying are based on the acquisition of cloud points to be treated and manipulated as three-dimensional spatial descriptions. The usual acquisition of these points is made through processes such as photogrammetry and laser scan, sometimes assisted with external devices for covering broad areas [8]. Point clouds can be the base of further developments, such as generating surfaces and volumes through adequate processing. The most usual approaches for obtaining point clouds from physical objects are photogrammetry and laser scan [15].

In Data acquisition techniques some hardware and software can be used. The most important ones mentioned below.

2.3.1. Hardware

Data collection is primarily conducted through Terrestrial Laser Scanning (TLS) and Unmanned Aerial Vehicles (UAVs). Photogrammetry techniques using UAV imagery are particularly advantageous when combined with point clouds generated by TLS, as demonstrated in studies by Dore and Murphy (2012), Trisyanti et al. (2019) and Suwardhi et al. (2016) [13].

2.3.2. Software

Different software tools are used to process both aerial triangulation data and TLS data. For aerial triangulation data, tools such as Metashape, Pix4D, and CloudCompare are commonly employed. These software applications facilitate the processing and integration of images captured by UAVs. Geo referencing, which ensures that spatial data is aligned with realworld geographic coordinates, is a crucial component of this process. According to Przybilla et al. (2020), for example, Metashape can perform georeferencing by aligning aerial images with real-world coordinates using control points. Conversely, the processing of TLS data often involves softwares such as Faro Scene and RecapPRO, which also support geo referencing to ensure the spatial alignment of the scanned data [13].

2.3.3. Driven data for GIS

The attributes to be coded in a GIS database can come from different sources. The suitability of on-site surveys with proper documentation tools can permit to acquire accurate descriptions directly from the primary source. However, this process is constrained by the scale of the surveyed territory. For this reason, information must be acquired from territorial-scale three-dimensional models [8].

The representation of three-dimensional objects by means of point clouds is based on assuming that the physical surfaces can be represented through a sufficiently dense group of points that hypothetically tends to infinite. Then, a finite number of points is saved with information regarding relative or absolute spatial coordinates, which permits the spatial reconstruction of the object when assembling the sets of points.

The GIS database would be able to be fed from different sources, such as on-site surveys and from data extracted directly from BIM-HBIM models by using a proper interface. Expectedly, the origin of BIM-HBIM models might be variable, since there is a vast number of actors interested in their creation and update, namely contractors, designers, government instances or academic institutions [8]**.**

2.4. Methods for integrating HBIM and GIS

One of the methodologies adopted for the purpose, is carried a systematic analysis of data and metadata related to HBIM-GIS integration. three primary methods for integrating HBIM and GIS presented in some previous studies are as below.

2.4.1 Scan-to-HBIM-GIS

This method is used for the collection, processing, modeling, and integration of data for HBIM-GIS. It explores the entire process, from data capture to the creation and integration of the HBIM-GIS model. three approaches are presented to the integration between HBIM
and GIS in the case study of Rafael et al. (2024) [13].

2.4.1.1. Direct integration

research conducted by El-Meouche, Rezoug and Hijazi (2013) [16] and Matrone et al. (2019)[14] evaluate the direct integration between Revit software (version 2024) and ArcGIS Pro (version 2024.3.0).

This study utilizes the most recent advancements in ArcGIS technologies, including ArcGIS Online, to enhance the dissemination and management of knowledge pertaining to the architectural heritage of the Pampulha Complex [13].

2.4.1.2. Conversion of HBIM to Shape file

Based on the work of Matrone et al. (2019), it can be employed Safe Software FME (version 3.0) to validate and convert data from the IFC 4 format to shapefile. Subsequently, the converted data can import into ArcGIS Pro.

2.4.1.3. Conversion of HBIM to Geodatabase

It is utilized Safe Software FME to convert the HBIM model to the Geodatabase format, and then imported the data into ArcGIS Pro. The resulting HBIM-GIS data are subsequently made available through a Web-GIS platform to facilitate access and visualization.

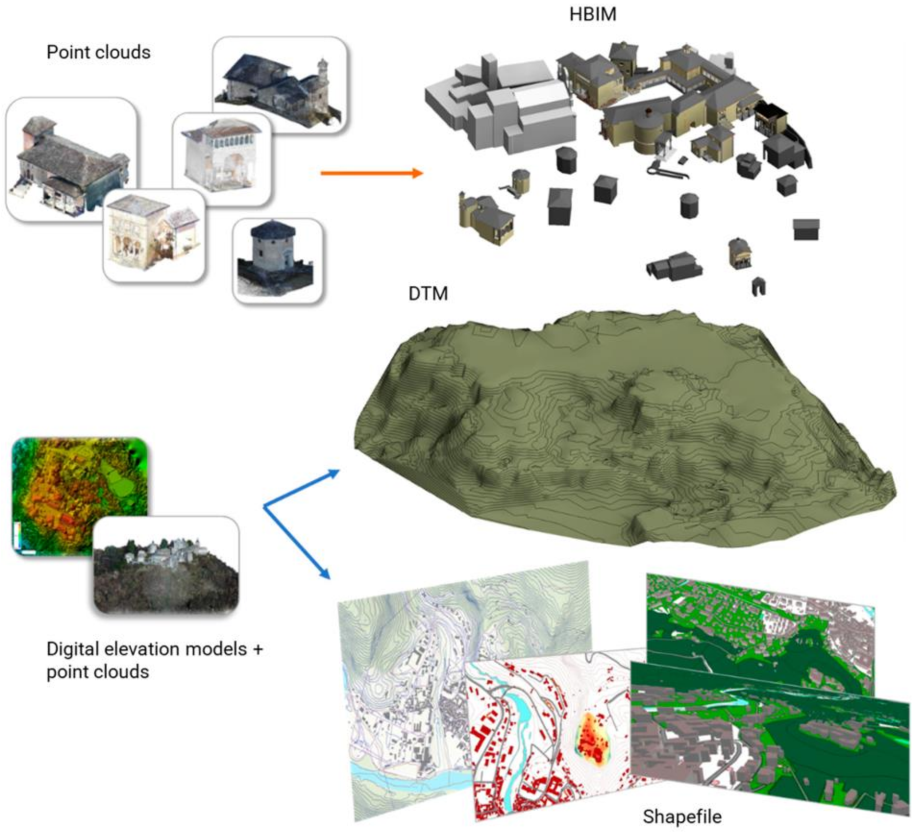

Figure 1. Data workflow from point clouds to HBIM models and GIS environment [17]

3. Result

The integration of HBIM and GIS is a new discipline that have potential applications and opportunities. these interplay between historic buildings modelling and geographical information systems have utilized in in the field of built heritage management and conservation.

A compelling ability of GIS is to document former urban configurations. there is a framework to develop retroactive models that can receive historical hypotheses and add new data [18] helping to integrate a continuous narrative for historical centers.

Although the HBIM models in the context of a GIS database is a very significant challenge, this issue has been solved through the use of a controlled reduction of details in the Level of Detail framework.

There are notable examples of HBIM-GIS integration that discuss its developing applications. The most mentioned applications in different studies are;

- Digital representations of cultural heritage
- Reading, documentation and cataloguing of historic buildings and monuments
- Parametrization of complicated geometry of architectural heritage
- Digital conservation and protection
- Maintenance and conservation
- Analysis and assessment of Vulnerability of historic buildings
- Analysis and assessment of urban risk
- Simulation of phenomena's and predictions of behaviors affected by Structural behaviors, soil settlement, load changes and material erosion.
- Heritage management
- Integrating multiscale spatial information
- Semantic modelling and parametric modelling
- Creating geometric models with semantic and parametric information in different levels of detail (LOD)
- To Prepare a risk map from the perspective of gradual destruction by collecting information about decay processes in the building's façades – such as cracks or lack of verticality –, which is then used for mapping an overall risk indicator [19]. so representing risks and hazards, with regard to risk analysis is because of the suitability of HBIM-GIS integration which considered in reviews and reveals the integrated framework application and its usefulness [20].
- Testing diverse environmental agents related to physical decays, including wind, solar incidence and water flow [7].
-

4. Conclusion

The integration of HBIM and GIS have many common benefits for the protection of architectural and urban heritage and the sustainability and structural retrofitting of constructed buildings and structures. This integration is also used in multi-criteria decision-making in the selection of appropriate methods for the documentation, management, conservation, and retrofitting of cultural heritage.

References

1. Lovell, L.J., R.J. Davies, and D.V. Hunt, *The application of historic building information modelling (HBIM) to cultural heritage: a review.* Heritage, 2023. **6**(10): p. 6691-6717.
2. van Nederveen, G.A. and F.P. Tolman, *Modelling multiple views on buildings.* Automation in Construction, 1992. **1**(3): p. 215-224.
3. Eastman, C.M., *Building product models: computer environments, supporting design and construction*. 2018: CRC press.
4. Li, X., et al., *Mapping the knowledge domains of Building Information Modeling (BIM): A bibliometric approach.* Automation in Construction, 2017. **84**: p. 195-206.
5. Murphy, M., E. McGovern, and S. Pavia, *Historic building information modelling (HBIM).* Structural Survey, 2009. **27**(4): p. 311-327.
6. Pepe, M., et al., *Toward to Combination of GIS-HBIM Models for Multiscale Representation and Management of Historic Center.* Heritage, 2024. **7**(12): p. 6966-6980.
7. Pelliccio, A., M. Saccucci, and E. Grande, *HT_BIM: Parametric modelling for the assessment of risk in historic centers.* Disegnarecon, 2017. **10**(18): p. 5-1-5.12.
8. Ramírez Eudave, R. and T.M. Ferreira, *On the suitability of a unified GIS-BIM-HBIM framework for cataloguing and assessing vulnerability in Historic Urban Landscapes: a*

critical review. International Journal of Geographical Information Science, 2021. **35**(10): p. 2047-2077.
9. Strafaci, A., *What does BIM mean for civil engineers?* CE News, 2008. **20**(9).
10. Quattrini, R., et al., *From TLS to HBIM. High quality semantically-aware 3D modeling of complex architecture.* The International Archives of the Photogrammetry, Remote Sensing and Spatial Information Sciences, 2015. **40**: p. 367-374.
11. Fischer, M.M., *From conventional to knowledge-based geographic information systems.* Computers, environment and urban systems, 1994. **18**(4): p. 233-242.
12. Wate, P., et al. *Formulation of hierarchical framework for 3D-GIS data acquisition techniques in context of Level-of-Detail (LoD)*. in *2013 IEEE Second International Conference on Image Information Processing (ICIIP-2013)*. 2013. IEEE.
13. Fernandes Dionizio, R. and E. Dezen-Kempter, *From data and metadata to HBIM-GIS integration.* International Journal of Architectural Heritage, 2025. **19**(10): p. 2443-2456.
14. Matrone, F., et al., *HBIM in a semantic 3D GIS database.* The International Archives of the Photogrammetry, Remote Sensing and Spatial Information Sciences, 2019. **42**: p. 857-865.
15. Lerma, J.L., et al., *Modelado fotorrealístico 3D a partir de procesos fotogramétricos: láser escáner versus imagen digital.* Cuadernos de arte rupestre, 2013. **6**(85-90): p. 86.
16. El Meouche, R., M. Rezoug, and I. Hijazi, *Integrating and managing BIM in GIS, software review.* The International Archives of the Photogrammetry, Remote Sensing and Spatial Information Sciences, 2013. **40**: p. 31-34.
17. Matrone, F., et al., *The HBIM-GIS Main10ance platform to enhance the maintenance and conservation of historical built heritage.* Sensors, 2023. **23**(19): p. 8112.
18. Yang, M., R. Brumana, and M. Previtali, *Heritage & development" strategy on historic urban landscape (HUL): The added value of multi-Temporal hub application.* ISPRS Annals of the Photogrammetry, Remote Sensing and Spatial Information Sciences, 2019. **42**(2): p. 1151-1158.
19. Campanaro, D.M., et al., *3D GIS for cultural heritage restoration: A ‘white box’workflow.* Journal of Cultural Heritage, 2016. **18**: p. 321-332.
20. De Ruvo, V., *Indagini sull’interoperabilità HBIM–GIS in un database europeo per la resilienza dei beni culturali= HBIM-GIS interoperability investigations in a european database for Cultural Heritage resilience*. 2019, Politecnico di Torino.

A review of the plant chlorophyll parameter retrieval through hyperspectral data in remote sensing

Amir Mohammad Ghalenovi[1] and Elahe Akbari[2]*
[1]MSc. Student. Department of Remote sensing and GIS, Faculty of Geography and Environmental sciences, Hakim sabzevari University, Sabzevar, Iran. E-mail: amir.ghalenovi@sun.hsu.ac.ir
[2]Assistant Professor, Department of Remote sensing and GIS, Faculty of Geography and Environmental sciences, Hakim sabzevari University, Sabzevar, Iran. E-mail: e.akbari@hsu.ac.ir

Abstract

Estimating chlorophyll content of vegetation plays a critical role in assessing plant physiological conditions, health status, nutrient requirements, and water stress levels. Remote sensing technologies offer valuable tools for estimating biophysical and biochemical vegetation parameters. This review paper introduces and classifies the primary methods used for estimating chlorophyll content through remote sensing. These methods are typically divided into three main categories: empirical–statistical approaches (including parametric and non-parametric regression such as linear models and machine learning algorithms), physical-based methods, and hybrid techniques that combine both. The strengths and limitations of each method are discussed, along with a critical analysis of existing research in this domain. Furthermore, the potential of hyperspectral remote sensing in chlorophyll estimation is explored by comparing different methodological approaches. Recent studies reveal a growing tendency toward the application of machine learning algorithms and UAV-derived data, often in combination with spectroscopic measurements. Among these machine learning techniques, kernel-based methods—particularly Gaussian Process Regression (GPR)—have gained notable attention. Researchers have also explored the integration of radiative transfer models with machine learning algorithms, aiming to reduce computational complexity while benefiting from the strengths of both methodologies. By reviewing the current body of research, this paper aims to provide researchers with a deeper understanding of leaf chlorophyll estimation techniques. The unique capabilities of remote sensing—especially when used in a time-series framework—enable accurate, cost-effective monitoring of chlorophyll dynamics throughout the plant growth cycle. This knowledge supports precision agriculture and improved decision-making in crop management under changing environmental conditions.

Keywords: Plant parameter, Remote Sensing, Chlorophyll, Hyperspectral data

1. Introduction

In the context of climate change, water scarcity, and population growth, enhancing crop productivity and advancing precision agriculture in arid regions has gained increasing attention (Zhao & Wang, 2020). Estimating plant biophysical/biochemical parameters is essential for understanding plant physiological status and ecosystem health. Moreover, identifying stress conditions such as water stress and improving resource management are additional advantages of retrieving plant parameters (Lu & He, 2019).

Chlorophyll is the most critical pigment involved in photosynthetic activity (Xu et al., 2019), and it is considered one of the most fundamental biophysical parameters in plants. This parameter is closely related to plant phenology and is indicative of plant health status (Wang et al., 2022). Additionally, due to the strong relationship between chlorophyll content and plant nitrogen levels, estimating chlorophyll enables assessment of plant nitrogen concentration, which is vital for crop growth, health, and productivity (Gitelson et al., 2014). This estimation can subsequently support the monitoring and management of nitrogen fertilizer applications. Furthermore, leaf chlorophyll content is closely linked to plant stress and senescence (Gitelson et al., 2003).

Although plant parameters can be estimated accurately through laboratory-based methods, limitations such as time consumption, high costs, and the inability to scale up to larger areas, so, restrict their practical use (Peyghari et al., 2020). In contrast, remote sensing technology—ranging from multispectral to hyperspectral sensors—has emerged as a reliable approach for estimating plant parameters. It offers advantages such as high spatial and temporal resolution, lower time requirements, easier data accessibility, and wide-area coverage, making it superior to traditional methods (Croft et al., 2015; Akbari et al., 2020).

Spectroscopy data typically consist of hundreds to thousands of narrow and contiguous spectral bands, enabling highly accurate detection of absorption features in leaf reflectance. The availability of such data has led to the development of advanced methods for monitoring and retrieving plant parameters such as Leaf Chlorophyll Content (LCC) (Zhao et al., 2013; Peyghari et al., 2020; Huang et al., 2023). In this regard, empirical-statistical methods (including parametric and non-parametric regressions—both linear and machine learning approaches), physical-based models, and hybrid methods have been proposed.

This study provides a comprehensive review of the strengths and limitations of these methods, focusing on the retrieval of chlorophyll content using remote sensing techniques. The potential of hyperspectral remote sensing for chlorophyll estimation using different methods is discussed, along with their respective advantages and disadvantages. By reviewing relevant studies, this study aims to enhance researchers' understanding of LCC estimation, emphasizing that remote sensing can enable cost-effective and timely assessment of chlorophyll content across crop growth stages through time-series analysis.

2. Methods for Chlorophyll Retrieving by Remote Sensing: Advantages & Dis-advantages

Methods for retrieving plant parameters from remote sensing data are generally classified into three categories: empirical-statistical approaches (including parametric and non-parametric regression methods—both linear and machine learning-based), physical-based methods, and hybrid approaches (Verrelst et al., 2018) (Fig 1).

Empirical-statistical methods are widely employed due to their capability to establish regression relationships between vegetation indices and target variables. These relationships are then used to estimate the plant parameters (Clevers, 2014). However, these algorithms do not provide uncertainty estimations, and the presence of multiple plant parameters and various environmental factors introduces considerable complexity that can hinder their performance. Additionally, model training in these methods is highly region-specific, requiring retraining when applied to new study areas (Verrelst et al., 2012; Akbari et al., 2020).

Linear non-parametric algorithms (such as multivariate linear regression), despite being popular due to their simplicity and ease of implementation, face limitations when dealing with hyperspectral data because of the high multicollinearity among spectral bands (Verrelst et al., 2018).

Physical-based methods, such as Radiative Transfer Model (RTM) inversion, offer greater generalization potential by relying on fundamental physical laws rather than empirical correlations. This enables their application across diverse ecosystems and sensor configurations, making them highly valuable for large-scale retrieval of biophysical parameters such as chlorophyll content or LAI. Although their computational complexity and need for detailed prior knowledge about canopy structure, soil properties, and illumination geometry can pose significant challenges, these approaches provide physically interpretable results and demonstrate moderate to high accuracy (R^2 values typically ranging from 0.6 to 0.8). Such robustness and transferability, despite slightly lower predictive performance compared to data-driven models, highlight RTM inversion as a reliable and scientifically transparent approach in remote sensing studies (Verrelst et al., 2012; Akbari et al., 2020).

As a result, machine learning algorithms (non-linear, non-parametric methods) have gained more attention for retrieving plant biophysical/biochemical variables from hyperspectral data (Verrelst et al., 2015). These algorithms are highly effective in handling the strong nonlinearity often observed between reflected radiation and plant parameters, and they offer greater flexibility. However, it is important to note that such flexibility can lead to overfitting. Therefore, techniques such as cross-validation and hyperparameter tuning must be applied to reduce model complexity and mitigate overfitting (Verrelst et al., 2018; Akbari et al., 2020).

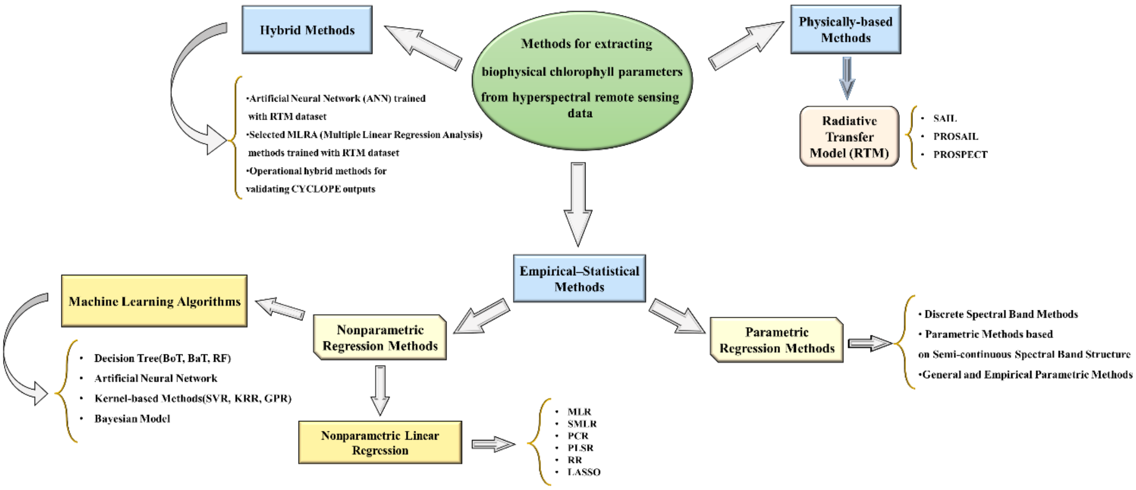

Figure 1. List of all methods used in estimating of chlorophyll parameter from hyperspectral data of remote sensing

3. Review of Studies on Chlorophyll Retrieving by Remote Sensing

A review of studies on chlorophyll retrieval using parametric regression reveals limited usage, mostly relying on spectroscopy and narrow-band indices, with fewer using satellite data like Hyperion and CHRIS-PROBA. Recent trends show growing interest in combining UAV and Sentinel-2 imagery with spectroscopic data to enhance chlorophyll estimation accuracy.

Parametric methods are favored for their simplicity and processing speed but struggle with nonlinear relationships, noise sensitivity, and limited adaptability to complex environments. Their region-specific nature and lack of uncertainty estimation further reduce reliability.

Non-parametric regression methods, particularly machine learning (ML), have seen broader adoption. Techniques like Partial Least Squares Regression (PLSR), Support Vector Machines (SVM), Random Forest (RF), and especially Gaussian Process Regression (GPR) are frequently used due to their accuracy and ability to quantify uncertainty. Spectroscopy—especially UAV-based—is commonly utilized in these studies.

Researchers often enhance performance by combining multiple ML algorithms. For instance, Zhao et al. (2013) introduced Bayesian Model Averaging (BMA) to improve retrieval accuracy by integrating multiple models and reducing overfitting.

While nonlinear ML methods offer high accuracy and flexibility, they require intensive computation and overfitting risk. A significant challenge remains in managing the large volume of hyperspectral bands and identifying optimal subsets. Tools like GPR-BAT have proven effective in reducing dimensionality by selecting the most informative bands, ultimately improving chlorophyll estimation under noisy data conditions.

A review of studies utilizing Radiative Transfer Models (RTMs) for chlorophyll estimation shows a comparable number to parametric methods, with increasing interest in recent years. Due to the computational complexity of RTMs, hybrid approaches combining RTMs with machine learning have become more common. These combinations maintain RTMs' accuracy while benefiting from data-driven efficiency.

RTMs are valuable in estimating biophysical variables, thanks to their solid physical basis and ability to simulate energy transfer in vegetation. Though demanding in terms of input accuracy and computation, integrating RTMs with machine learning significantly enhances chlorophyll estimation performance.

Recent advances, particularly in satellite-based hyperspectral data, have led to frameworks where RTMs simulate training data for machine learning models. This reduces dependence on fieldwork and supports scalable, automated parameter retrieval for agricultural monitoring. Moreover, studies highlight the importance of selecting optimal spectral bands—especially in the visible to near-infrared range—for accurate chlorophyll estimation. Integrating algorithms like Kernel Ridge Regression (KRR) and Gaussian Process Regression (GPR) with RTM outputs improves estimation precision while ensuring regional applicability and reduced field dependency. Figure 2 and table 1 showed the methods frequency and types which used in studies in each time period for chlorophyll retrieval by remote sensing.

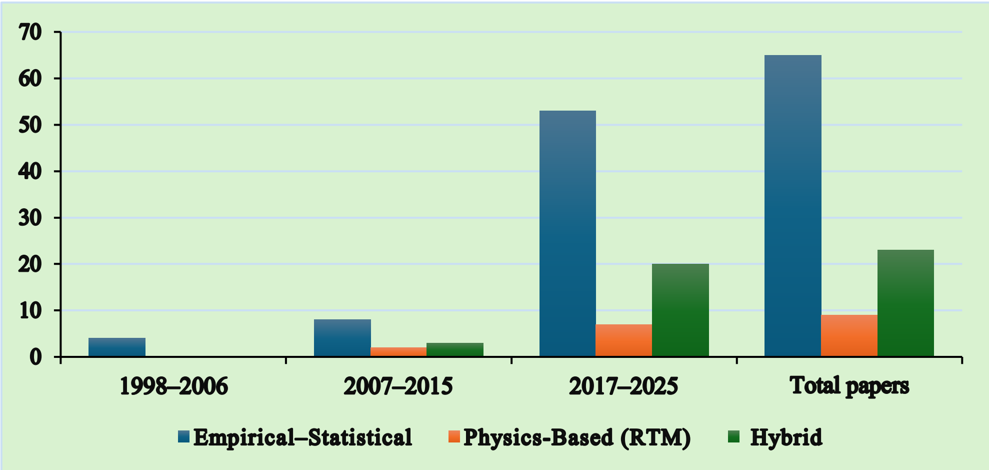

Figure 2. Methods Frequency for Chlorophyll Retrieval by remote sensing per Time Period
Table 1. Methods Types Used for Chlorophyll retrieval by remote sensing in Each Time Period

Time Period	Methods Used
1998–2006	VI, Derivatives, Simple Regressions
2007–2015	VI, PLSR, SMLR, RTM, RSI, NAOC
2017–2025	MLAs (RF, SVM, GPR, SVR, etc.), Hybrid (RTM + ML), GA + PLSR, BMA, PROSAIL, FOD, MRMR

4. Conclusion

This study provides a concise review of key methods for estimating leaf chlorophyll content using hyperspectral remote sensing, focusing on three main categories: empirical–statistical (parametric and non-parametric), physical-based (Radiative Transfer Models – RTMs), and hybrid approaches. Each method's strengths, limitations, and generalizability are comparatively assessed.

With rising demand for precision agriculture, water scarcity, and climate change, the need for accurate, fast, and non-destructive chlorophyll estimation has intensified. Hyperspectral data offer an efficient alternative to traditional techniques, enabling regional and temporal monitoring at lower cost and effort. Thus, evaluating these methods is vital for advancing practical monitoring tools.

Review showed that while parametric models were simple and fast, their reliance on linear assumptions and regional training restricts broader application. Non-parametric methods, especially machine learning, improve accuracy through flexibility in modeling nonlinear relationships but face challenges like overfitting and computational load. RTMs, grounded in physical theory, offer good generalization but require complex inputs.

Hybrid approaches combining RTMs with machine learning present a compelling solution. They balance accuracy and efficiency by uniting physical rigor with data-driven modeling, proving especially effective with high-quality hyperspectral inputs for scalable, operational chlorophyll monitoring.

References

Akbari, E., Darvishi Boloorani, A., Neysani Samany, N., HAMZEH, S., SOUFIZADEH, S., & Pignatti, S. (2020). Estimating the Spatial-Temporal Distribution of Leaf Area Index Using Sentinel-2 Satellite Images (Case Study: Silage Maize Farms of South of Tehran). IRANIAN JOURNAL OF IRRIGATION AND DRAINAGE, 13(3), 967-980. SID. https://sid.ir/paper/399694/en

Clevers, J. G. P. W. (2014). Beyond NDVI: extraction of biophysical variables from remote sensing imagery. In *Land use and land cover mapping in Europe: practices & trends* (pp. 363-381). Dordrecht: Springer Netherlands.

Croft, H., Chen, J. M., Zhang, Y., Simic, A., Noland, T. L., Nesbitt, N., & Arabian, J. (2015). Evaluating leaf chlorophyll content prediction from multispectral remote sensing data within a physically-based modelling framework. *ISPRS Journal of Photogrammetry and Remote Sensing*, *102*, 85-95.

Gitelson, A. A., Gritz, Y., & Merzlyak, M. N. (2003). Relationships between leaf chlorophyll content and spectral reflectance and algorithms for non-destructive chlorophyll assessment in higher plant leaves. *Journal of plant physiology*, *160*(3), 271-282.

Gitelson, A. A., Peng, Y., Arkebauer, T. J., & Schepers, J. (2014). Relationships between gross primary production, green LAI, and canopy chlorophyll content in maize: Implications for remote sensing of primary production. *Remote Sensing of Environment*, *144*, 65-72.

Huang, X., Guan, H., Bo, L., Xu, Z., & Mao, X. (2023). Hyperspectral proximal sensing of leaf chlorophyll content of spring maize based on a hybrid of physically based modelling and ensemble stacking. *Computers and Electronics in Agriculture*, *208*, 107745.

Lu, B., & He, Y. (2019). Evaluating empirical regression, machine learning, and radiative transfer modelling for estimating vegetation chlorophyll content using bi-seasonal hyperspectral images. *Remote Sensing*, *11*(17), 1979.

Piegari, E., Gossn, J. I., Juárez, Á., Barraza, V., Trilla, G. G., & Grings, F. (2020, March). Radiometric Characterization of a Marsh Site at the Argentinian Pampas in the Context of Hypernets Project (A New Autonomous Hyperspectral Radiometer). In *2020 IEEE Latin American GRSS & ISPRS Remote Sensing Conference (LAGIRS)* (pp. 591-596). IEEE.

Verrelst, J., Camps-Valls, G., Muñoz-Marí, J., Rivera, J. P., Veroustraete, F., Clevers, J. G., & Moreno, J. (2015). Optical remote sensing and the retrieval of terrestrial vegetation bio-geophysical properties–A review. *ISPRS Journal of Photogrammetry and Remote Sensing*, *108*, 273-290.

Verrelst, J., Muñoz, J., Alonso, L., Delegido, J., Rivera, J. P., Camps-Valls, G., & Moreno, J. (2012). Machine learning regression algorithms for biophysical parameter retrieval: Opportunities for Sentinel-2 and-3. *Remote Sensing of Environment*, *118*, 127-139.

Verrelst, J., Rivera-Caicedo, J. P., & Moreno, J. (2018, July). Progress in Emulation for Radiative Transfer Modeling and Mapping. In *IGARSS 2018-2018 IEEE International Geoscience and Remote Sensing Symposium* (pp. 1688-1691). IEEE.

Wang, T., Gao, M., Cao, C., You, J., Zhang, X., & Shen, L. (2022). Winter wheat chlorophyll content retrieval based on machine learning using in situ hyperspectral data. *Computers and Electronics in Agriculture*, *193*, 106728.

Xu, M., Liu, R., Chen, J. M., Liu, Y., Shang, R., Ju, W., ... & Huang, W. (2019). Retrieving leaf chlorophyll content using a matrix-based vegetation index combination approach. *Remote Sensing of Environment*, *224*, 60-73.

Zhao, J., & Wang, Z. (2020). Future trends of water resources and influences on agriculture in China. PLoS One, 15(4), e0231671.

Zhao, K., Valle, D., Popescu, S., Zhang, X., & Mallick, B. (2013). Hyperspectral remote sensing of plant biochemistry using Bayesian model averaging with variable and band selection. *Remote Sensing of Environment*, *132*, 102-119.

Production and Validation of Digital Elevation Models from UAV and Satellite Imagery

Eren Uzunoglu[1, *], Ugur Alganci[2], Dursun Zafer Şeker[2],
[1] Istanbul Technical University, Graduate School, Türkiye, uzunoglu19@itu.edu.tr
[2] Istanbul Technical University, Geomatics Engineering Department, Türkiye
alganci@itu.edu.tr, seker@itu.edu.tr

Abstract

Digital Elevation Models (DEMs) are essential for urban geospatial analysis, yet their accuracy varies depending on the acquisition method. This study compares DEMs generated from stereo unmanned aerial vehicle (UAV) imagery and stereo satellite data over Istanbul Technical University's Ayazağa Campus, an area characterized by complex topography and dense built structures. UAV data were captured using a DJI Mavic 2 Pro at an altitude of 80 m, producing 619 images with an approximate ground sampling distance (GSD) of 7 cm. Satellite imagery was sourced from the Airbus Pleiades system at 0.5 m resolution. Both datasets were processed using commercial photogrammetric software following an identical workflow, including image alignment, dense point cloud generation, mesh modeling, and DSM/DTM extraction. Accuracy was assessed using 12 independent GNSS control points. The UAV-derived DEM achieved a vertical RMSE of 1.94 m, whereas the satellite-derived DEM yielded 6.46 m. To evaluate resolution effects, elevation profiles were extracted from UAV, satellite, and SRTM (30 m) DEMs along identical transects. The UAV DEM preserved abrupt elevation changes such as rooftops, walls, and vegetation. In contrast, the satellite DEM exhibited smoothed terrain and systematic underestimation, while SRTM failed to capture local detail. Findings highlight the critical role of spatial resolution in urban morphology modeling. The UAV DEM provided the most detailed and realistic representation, making it suitable for infrastructure design, hydrological studies, and applications requiring precise elevation data. By integrating quantitative accuracy metrics with visual profile analysis, this study establishes a framework for DEM selection in urban environments.

Keywords: Digital Elevation Model (DEM), Unmanned Aerial Vehicle (UAV) Photogrammetry, Satellite Stereo Imagery, Accuracy Assessment, Geospatial Analysis

1. Introduction

Digital Elevation Models (DEMs) have become indispensable tools in geospatial sciences, providing three-dimensional (3D) representations of the Earth's surface. A DEM is represented in a raster grid format where each cell corresponds to an elevation value, and these models are highly versatile tools that can also be displayed using contours or triangulated irregular networks (TINs) (Ravibabu & Jain, 2008). DEMs historically originated as a computational tool in the 1950s at MIT, developed for the purpose of optimizing highway design (Doyle, 1978). Today, DEMs are divided into two main components: the Digital Surface Model (DSM), which represents the entire surface including features like buildings and vegetation, and the Digital Terrain Model (DTM), which represents only the bare-earth surface.

With advancements in remote sensing technologies, the resolution and accuracy of DEMs have significantly increased. These models are essential for tackling complex challenges in urban planning, environmental management, and infrastructure projects. The accuracy and precision of DEMs are paramount, especially for sensitive applications like rooftop solar energy potential estimation in urban environments (Kugler & Wendt, 2021).

The creation of DEMs primarily relies on photogrammetry, a technique that reconstructs the 3D terrain from 2D imagery obtained from UAVs, aerial photography, and satellite imaging.

- UAV Imagery: Offers finer spatial resolution due to low flight altitude and high sensor resolution, making it ideal for detailed analyses of urban morphology. UAV DEM production requires ensuring adequate overlap (minimum 60-70% between images) to generate a sufficiently dense point cloud (Ajayi et al., 2017).

- Satellite Imagery: Provides global coverage and cost-effectiveness for mapping large areas and environmental monitoring essential for hydrology, geology, and infrastructure planning (Kayadibi, 2009). Pleiades and similar satellite systems utilize stereo-photogrammetry to produce DEMs with high resolutions, often as fine as 0.5 meters, which, combined with the satellites' rapid revisit frequencies, ensures up-to-date data for precise geospatial applications. (Subramanian et al., 2003). However, satellite DEMs face limitations such as reduced vertical accuracy in complex terrains and susceptibility to cloud cover.

The core objective of this study is to compare the vertical accuracies and representation fidelities of UAV-derived DEMs and satellite-based DEMs to determine which data set provides more accurate results for urban applications. The İTÜ Ayazağa Campus, with its diverse terrain characteristics and dense urban structure, provides an ideal study area for this comparison. The findings of this research will guide the selection of the most suitable DEM source for urban planning and infrastructure management.

2. Materials and Methods

This study utilizes high-resolution stereo satellite images and UAV data to create Digital Elevation Models (DEMs). The UAV imagery provides higher resolution for extracting building heights and local details, while satellite data is preferred for monitoring large areas and conducting topographic analyses. Separate DEMs were generated from these two datasets to evaluate their accuracy and utility in modeling building heights and other features.

2.1. Study area and data acquisition

The study area is the Ayazağa Campus of Istanbul Technical University (ITU), located in Maslak, Istanbul. The area is characterized by a mix of landscaped green areas and densely built academic and administrative structures. A network of 84 Ground Control Points (GCPs) was established across the campus using high-precision GNSS instruments to support photogrammetric processing and ensure the accuracy of derived spatial models.

UAV Imagery: The aerial imagery was acquired by the DJI Mavic 2 Pro from a flight altitude of 80 meters. A total of 619 images were obtained, providing a high-resolution dataset with a camera resolution of 5472 times 3648 pixels. The UAV images were acquired with high overlap (at least 80% forward and 70% side overlap) to ensure sufficient redundancy for reliable 3D reconstruction.

Satellite Imagery: The imagery was sourced from the Airbus Pleiades satellite system, featuring a spatial resolution of 0.5 meters. The data were provided in GeoTIFF format and projected using the WGS 84 UTM Zone 35N coordinate system. For high-resolution satellite imagery, achieving accurate georeferencing often requires using ancillary data or GCPs to correct Rational Polynomial Coefficients (RPCs) and minimize potential misalignment.

2.2. Photogrammetric processing workflow

The DEM creation utilized Agisoft Metashape Professional, a software chosen for its capability to process high-accuracy 3D models from both UAV and satellite imagery, including its capacity to import RPC data for satellite scenes. The identical methodological approach was applied to both datasets to maintain consistency and comparability. The workflow involved the following steps:

a. Image Alignment and Georeferencing: Tie points were matched among overlapping images to estimate orientation parameters. The 84 GCPs, measured with high-precision GNSS, were incorporated prior to the alignment stage to ensure accurate georeferencing and minimize distortions. The high-overlap UAV imagery yielded a dense tie point network, allowing for robust camera alignment with minimal error.

b. Dense Point Cloud Generation: The dense point cloud was created using "High" quality for the UAV data and "Medium" quality for the satellite data to balance detail level and processing time.

c. DSM and DTM Generation: A Triangulated Irregular Network (TIN) surface was generated from the point cloud for the DSM. The DTM was produced by classifying the point cloud to isolate the ground class, followed by manual editing to refine ground point selection in vegetated or built-up areas.
d. Model Export: Both DSMs and DTMs were exported in GeoTIFF format. The output raster resolution was set to 7 cm/pixel for the UAV DEM which is shown in Figure 1 (a) and 0.5 m/pixel for the satellite DEM which is shown in Figure 1 (b).

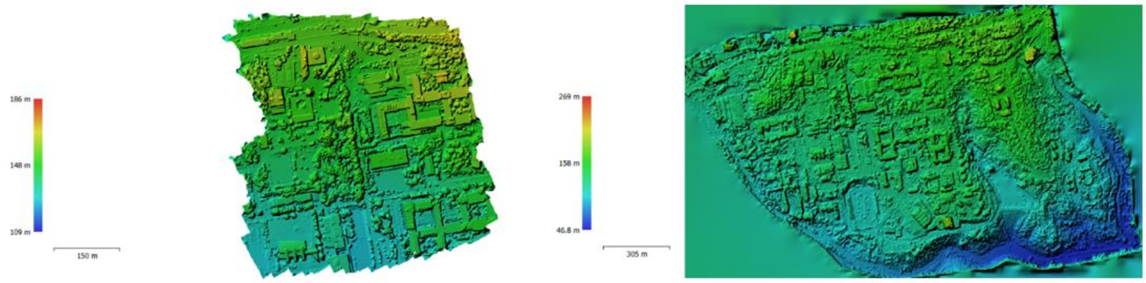

Figure 1.UAV DEM (a) and Satellite DEM (b).

2.3. Accuracy assessment

The vertical accuracy of the resulting DEMs was assessed using 12 independent GNSS points with a high-accuracy GNSS receiver. Error Calculation: The elevation values from both DEMs were retrieved at the exact GNSS locations using bilinear interpolation. The difference (Error) was calculated as:

$$\text{Error} = \text{DEM Elevation} - \text{GNSS Elevation}$$

Statistical Metrics: Model performance was quantified using standard statistical metrics, providing a comprehensive assessment of DEM quality and error magnitude.

Mean Error (ME): Measures the average bias relative to GNSS.
Root Mean Square Error (RMSE): Commonly used for DEM validation, giving more weight to larger errors. The RMSE provides a robust measure of overall vertical accuracy.

3. Results and Discussion

The DEM generation process yielded two distinct models with varying spatial resolutions: the UAV-derived DEM at 7 cm/pixel and the Satellite-derived DEM at 0.5 m/pixel. Following the generation, a detailed quantitative and qualitative assessment was conducted to compare their vertical accuracy and surface representation fidelity over the complex urban terrain.

3.1. Vertical accuracy assessment

The comparison results are presented in Table 1 below, showing the GNSS heights the elevations extracted from both DEMs, and the calculated errors:

Table 1. Height Accuracy Table from both DEMs

Point ID	GNSS Height (m)	UAV DEM Height (m)	UAV Error (m)	Satellite DEM Height (m)	Satellite Error (m)
N1001	152.874	150.943	-1.931	146.403	-6.471
N1016	135.24	133.303	-1.937	128.748	-6.492
N1018	143.98	142.094	-1.886	137.545	-6.435
N1020	148.212	146.246	-1.966	141.719	-6.493
N1022	145.169	143.186	-1.983	138.626	-6.543
N1036	132.102	130.156	-1.946	125.669	-6.433
N1037	153.855	151.899	-1.956	147.408	-6.447
N1041	130.018	128.086	-1.932	123.623	-6.395
N1042	150.709	148.788	-1.921	144.258	-6.451
N1065	155.269	153.35	-1.919	148.87	-6.399
N1073	131.837	129.915	-1.922	125.448	-6.389
N1084	136.378	134.416	-1.962	129.955	-6.423

Table 2. Error metric results

Metric	UAV DEM	Satellite DEM
ME	≈ -1.93 m	≈ -6.45 m
RMSE	≈ 1.94 m	≈ 6.46 m

The UAV DEM exhibited a narrow range of vertical error values (ranging from -1.88 m to -1.98 m), demonstrating high internal reliability and minimal deviation from the true ground surface. In contrast, the satellite DEM showed a wider and more significant error range (between -6.39 m and -6.54 m), resulting in an RMSE value over three times larger than that of the UAV model. Both DEMs consistently showed a negative mean error, indicating a systematic underestimation of elevation relative to the GNSS benchmarks.

3.2. Elevation profile comparison

To qualitatively evaluate the impact of spatial resolution on urban morphology representation, elevation profiles were extracted along an identical transect that crossed buildings, roads, and vegetated areas, covering approximately 60 m. The profiles of the UAV DEM, Satellite DEM, and the global SRTM DEM (30 m) were compared with horizontal pixel in Figure 2 and vertical pixels in Figure 3.

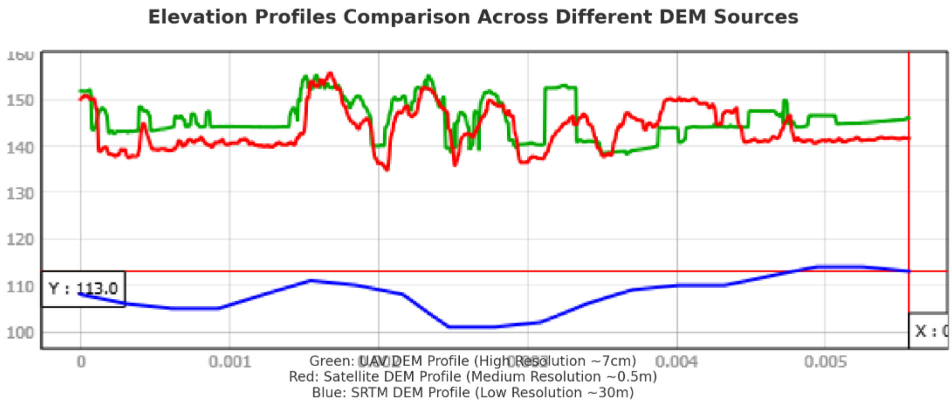

Figure 2. Elevation Profile Comparison from Horizontal Pixels

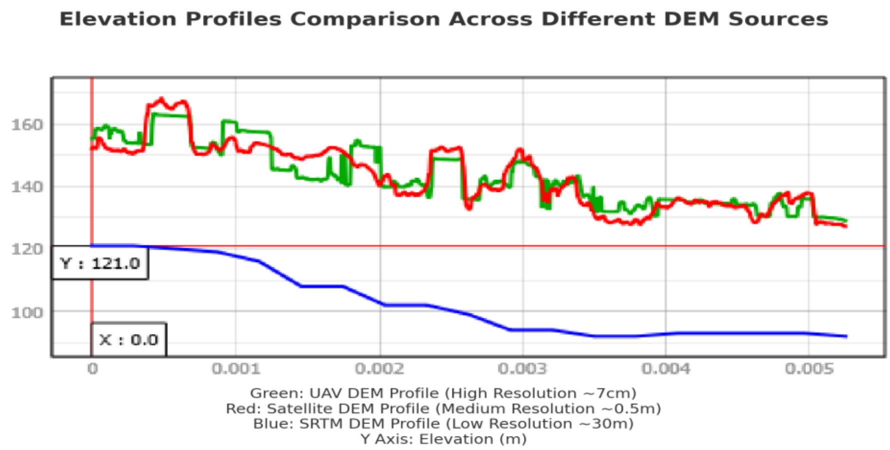

Figure 3. Elevation Profile Comparison from Horizontal Pixels

UAV DEM (Green Line): The profile exhibited high-frequency oscillations, precisely capturing abrupt elevation changes caused by individual building edges, walls, and subtle terrain variations.
Satellite DEM (Red Line): This profile followed the general terrain form of the UAV profile but lacked fine textural details. Building blocks were partially discernible, but sudden elevation changes appeared rounded or plateaued, a clear sign of resolution-based generalization.

SRTM DEM (Blue Line): This was the least dynamic profile, displaying only general elevation trends due to its 30-meter resolution. It failed to identify any recognizable urban structures and consistently displayed a smooth curve with minimal variation.

The comparison of "curve roughness" directly reflects the sampling density, emphasizing that higher resolution (UAV) yields more detailed and realistic surface curves.

The comparative analysis reveals that -based photogrammetry provides a significantly more accurate terrain representation compared to satellite-derived data in the context of local-scale urban mapping.

The accuracy achieved with UAV data of 1.94 m consistently outperforms the satellites data that is 6.46 m. This is attributed to the high spatial resolution and the low flight altitude of imagery, which enable the capture of finer terrain features and results in more reliable elevation models. Furthermore, data processing using dense point cloud generation and Structure-from-Motion algorithms contributes to higher vertical precision. This low supports the suitability for high-precision applications such as engineering surveys and urban planning.

In contrast, the satellite-based DEM, although adequate for large-scale overviews, suffers from coarser spatial resolution and potential geolocation inaccuracies. The systematic underestimation observed across all points suggests a need for vertical bias correction. Such elevation discrepancies are in line with reported limitations of medium-resolution satellite-derived s, particularly those generated without rigorous ground control. Sources of potential error in satellite data include misalignment during orthorectification, smoothing and terrain shadowing across hills, and the sensor's inherent low spatial resolution. Improving the georeferencing accuracy of such imagery often requires using ancillary data or highly accurate.

Qualitative analysis using elevation profiles further underscores the influence of resolution. While UAV data captures the micro-topography essential for urban infrastructure studies, satellite-derived models introduce smoothing and positional inaccuracies due to limited pixel size and constraints in stereo reconstruction. The 30 m DEM is highly generalized and unsuitable for projects requiring elevation accuracy below 10 m.

This study provides a framework for selecting appropriate data sources in urban environments. UAV-based photogrammetry stands out for its ability to resolve individual features such as building edges, offering the most accurate representation of real terrain. This makes it an ideal solution for applications like building-level energy modeling and precision urban mapping. Despite limitations in spatial coverage per flight and dependency on weather conditions, the UAV approach remains a cost-effective and highly accurate option.

4. Conclusion

This study compared the performance and usability of s derived from imagery, stereo satellite imagery, and global data. The performance was assessed based on statistical metrics of accuracy and profile-based elevation portrayals across the Ayazağa Campus. The UAV based data with spatial resolution of 7 cm provided superior vertical accuracy, achieving of 1.94 m. This confirms its suitability for applications requiring very detailed and localized topographic representation, such as building-level energy modeling. The Satellite based result with a spatial resolution of 0.5 m yielded an accuracy of 6.46 m. While adequate for large-area coverage, its low vertical accuracy makes it insufficient for engineering applications that cannot tolerate meter-level variations in height.

This comparative exercise emphasizes the importance of choosing a source aligned with the intended spatial scale. accuracy aspects, particularly the spatial structure of errors and the choice of accuracy metrics like, must always be considered when evaluating data quality for spatial analysis. For future work, researchers are encouraged to adopt a hybrid approach by combining satellite and data to balance accuracy and coverage. Further studies could also explore the use of data for comparative validation.

References

Ajayi, O. G., Salubi, A. A., Angbas, A. F., & Odigure, M. G. (2017). Generation of accurate digital elevation models from UAV acquired low percentage overlapping images. *International journal of remote sensing, 38*(8-10), 3113-3134.

Doyle, F. J. (1978). Digital terrain models: An overview. *Photogrammetric Engineering and Remote Sensing*, *44*(12), 1481-1485.

Kayadibi, O. (2009, June). Recent advances in satellite technologies using to generate the Digital Elevation Model (DEM). In *2009 4th International Conference on Recent Advances in Space Technologies* (pp. 380-385). IEEE.

Kugler, T., & Wendt, L. (2021). Evaluation of Digital Elevation Models Derived from Multi-Date Satellite Stereo Imagery for Urban Areas. *GI_Forum 2021*, 9, 60-67.

Ravibabu, M. V., & Jain, K. (2008). Digital elevation model accuracy aspects. *Journal of Applied Sciences, 8*(1), 134–139.

Subramanian, K. S., Singh, A., & Sudhakar, M. (2003). Evaluation of Digital elevation models created from different satellite images. *Map India in Technology.*

Optimal location of rescue bases on the Chalous road: a deep learning-based approach

Bahare Sadat Mousavi[1*], Meysam Argany[2] and Najme Neysani Samany[2], Ahmad Soltani[3,4], Mohsen Forouzande [5]

[1] PhD In Geographic Information Systems and Remote Sensing, Faculty of Geography, Kish International Campus, University of Tehran, Iran. (First Author). Email: Bahare.mousavi@ut.ac.ir

[2] Assistant Professor and Master Candidate, Department of Remote Sensing and GIS, Faculty of Geography, University of Tehran, Iran. Emails: argany@ut.ac.ir, nneysani@ut.ac.ir

[3] Iran Helal Applied Science Higher Education Institute, IRCS, Tehran, Iran.

[4] Department of Health in Emergencies and Disasters, School of Public Health, Tehran University of Medical Sciences, Tehran, Iran.

[5] M.Sc. in Geographic Information Systems and Remote Sensing, Faculty of Geography, University of Tehran, Iran.

Abstract

Road accidents, especially on mountainous roads, pose significant traffic safety challenges that require accurate prediction and optimal management. In Iran, as a disaster-prone country, road accidents rank as the second-highest risk in terms of occurrence frequency, after earthquakes, highlighting the critical importance of road accidents as a significant risk factor. In this study, using data from the Red Crescent mission reports along with road, environmental, and traffic features, a deep learning transformer model was developed to identify accident-prone locations on the Chalous road corridor. This model extracted complex nonlinear patterns with considerable accuracy and predicted high-risk points categorized into three accident severity classes (fatal, injured, treated on site). Subsequently, using the Grey Wolf Optimizer algorithm, the optimal placement of rescue bases was performed to increase road coverage and reduce response time. Results showed that rescue coverage on the Chalous corridor increased from 22.77% to 86.91%, and average response time decreased from approximately 14 minutes 45 seconds to 8 minutes 22 seconds, representing a 64% improvement in coverage and a 43% reduction in reaction time, respectively. This study demonstrated that integrating real-world data, advanced deep learning models, and optimization algorithms provides an effective tool for improving rescue management, enhancing safety on high-traffic and high-risk corridors, and reducing injuries and fatalities. The findings can serve as a basis for designing intelligent crisis management systems and developing preventive programs in other regions of the country.

Keywords: Road Accidents, Deep Learning Transformer, Grey Wolf Optimizer Algorithm, Rescue Coverage, Response Time.

1. Introduction

The increasing number of vehicles has made road accidents a major global safety concern, with costs equivalent to 3% of annual GDP (Zheng et al., 2019). In Iran, road accidents rank second in frequency after earthquakes (Soltani et al., 2021). Machine learning models, particularly transformers, are more effective than traditional methods in identifying complex accident patterns (Zhang, 2019; Astarita et al., 2023).

In recent years, numerous studies have been conducted on predicting road accidents and optimizing rescue base locations. For example, Goli and Malmir reduced the response time of rescue vehicles using a coordination search algorithm and credibility theory optimization. They stated that optimization algorithms are essential for determining the optimal locations of rescue bases in crisis management (Goli & Malmir, 2019). Li et al. presented a combined LSTM and CNN model to predict the risk of accidents on urban roads (Li & Yuan, 2020). Shang et al. employed RF-RFE algorithms, LSTM networks, and BOA optimization for automatic accident detection in intelligent transportation systems (Shang et al., 2020). Guo et al. improved rescue response time in urban search and rescue operations using a transformer and attention-based LSTM (Guo et al., 2021). Yang et al. used reinforcement learning to reduce the response time of rescue vehicles in mountainous regions (Yang et al., 2021). Zhao et al. enhanced the prediction accuracy of the LSTM model by optimizing it with the Grey Wolf Optimization (GWO) algorithm (Zhao et al., 2022). Astarita et al. proposed a combined GWO-ANN model to predict accident severity and optimize the location of rescue bases (Astarita et al., 2023). Wang et al. introduced the Dual-Transformer model to predict spatio-temporal relations of accidents (Wang et al., 2023). Al-Thani et al. developed a multi-attention transformer model for accident prediction (Al-Thani et al., 2024). Huang et al. used the DGWO-F2OPT algorithm to increase the response speed of emergency vehicles (Huang et al., 2024). Ahmadi et al. used the GIS-ACO-QAP model for optimal location of rescue bases, which reduced response time and improved access to emergency services (Ahmadi et al., 2024). Jiang et al. predicted the severity of injuries in accidents using a transformer model (Jiang et al., 2025). Peng and Yan introduced the TTT-Enhanced Transformer model, which improved road accident prediction performance (Peng & Yan, 2025). Based on these studies, this study uses a transformer model for optimal location of rescue bases in mountainous corridors to compare road coverage and response times in the current and proposed states.

2. Materials and Methods

This study focuses on the mountainous Chalous corridor, a key transportation route between Mazandaran and Alborz provinces. Due to its unique geographic location, its role in northern travel routes, and high traffic volume, especially during peak seasons, the corridor is known for its high accident rate and hazardous areas (Mousavi et al., 2023). These factors make it a priority for road rescue and emergency planning. Figure 1 shows the distribution of road accidents on the Chalous corridor from March 2017 to January 2024.

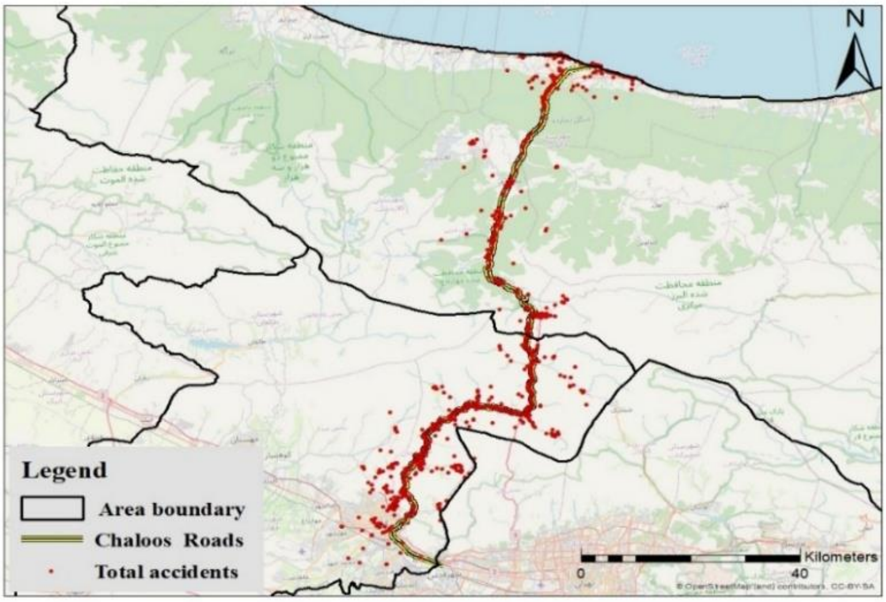

Figure 1. Distribution of road accidents in the studied corridor.

In this study, road accident data, including fatalities, injuries, and on-site treatments, were collected from the Red Crescent Rescue Organization, along with environmental, traffic, and road characteristics from the Road Maintenance and Transportation Organization, for the period from March 2017 to January 2024, to identify accident-prone locations along the studied corridor (Table 1). Finally, to evaluate and compare the coverage percentage of rescue bases and response times in both current and proposed scenarios, the optimal placement of rescue bases was determined using the GWO algorithm.

Table 1. Characteristics and Categorization of Input Features for the Deep Learning Model

Data Provider Organization	**Feature Names**	**Feature Categories**
Road Maintenance and Transport Organization	Rainfall, snow and blizzards, landslides and ground subsidence, fog and visibility reduction, slipperiness, floods and waterlogging, dust storms, normal conditions	Environmental Features
Road Maintenance and Transport Organization	Blocked and heavy, flowing and semi-flowing, unclear status	Traffic Features
Road Maintenance and Transport Organization	Night or day conditions, road type (main, secondary, rural, etc.), road surface condition, presence or absence of tunnels, presence or absence of bridges, road slope, altitude above sea level, route type (one-way or two-way), proximity to arterial roads, days of the week, start time, end time, incident time, start date, end date, and other related features	Road Features

The features were input into the model as raster data and numerical codes, which were then divided into two parts: training (70%) and testing (30%). The model output was presented as a raster map in four different classes: fatalities, injuries, on-site treatment, and no accident. Subsequently, to improve emergency response, the optimal placement of Red Crescent bases was carried out using the GWO algorithm, aiming to reduce the response time to road accidents to less than 14 minutes. The inputs to the algorithm included the map of accident-prone locations, the positions of the bases, and their operational radius from accident hotspots.

The deep learning model used in this study is the Transformer, which, unlike RNN and LSTM, relies on an attention-based structure, enabling parallel processing and learning long-term dependencies. This makes it suitable for time series analysis and traffic data, outperforming traditional models like LSTM and CNN in detecting accident-prone areas (Vaswani et al., 2017; Wu et al., 2021). Given the significant role of metaheuristic algorithms in solving complex problems, the Grey Wolf Optimization algorithm was used in this study for optimal base placement. Introduced by Mirjalili et al. in 2014, this algorithm is inspired by the social behavior and hunting strategy of grey wolves (Astarita et al., 2023). After predicting accident-prone locations with the Deep Transformer model, the optimal placement of rescue bases was determined to improve road coverage and reduce response time.

3. Results

To evaluate the performance of deep learning-based classification models, several models were trained. Among them, satellite_classification_tversky_2 showed the best performance in terms of accuracy and loss on the training, validation, and test datasets. In Figure 2, the accuracy and loss graphs of this model are presented, where the continuous reduction in loss and the maintenance of high accuracy across different data sets indicate successful learning and the model's ability to generalize to new data. The model was able to predict accident-prone locations in three categories: fatalities in red, injuries in green, and on-site treatment in blue, using environmental and traffic features (Figure 3). To evaluate the coverage of Red Crescent bases, the operational radius of the existing rescue bases was first determined based on their geographic locations in the road network. Then, using the Network Analysis tool, the coverage of roads and response times of the existing and proposed bases were compared. This analysis enabled the calculation of the coverage percentage and response times for each base based on access through the road network (Figure 4).

The results of the analysis provide a basis for comparing the current situation with the proposed base locations to quantitatively assess the improvement in road coverage and response time. In this context, the optimal location of rescue bases was determined using the Grey Wolf Optimization algorithm. Figure 5 shows the accident density and the positions of both existing and proposed bases. The algorithm suggested five optimal base locations for the Chalous corridor, which are situated near high-density accident areas, thereby improving access and response time in the mountainous routes.

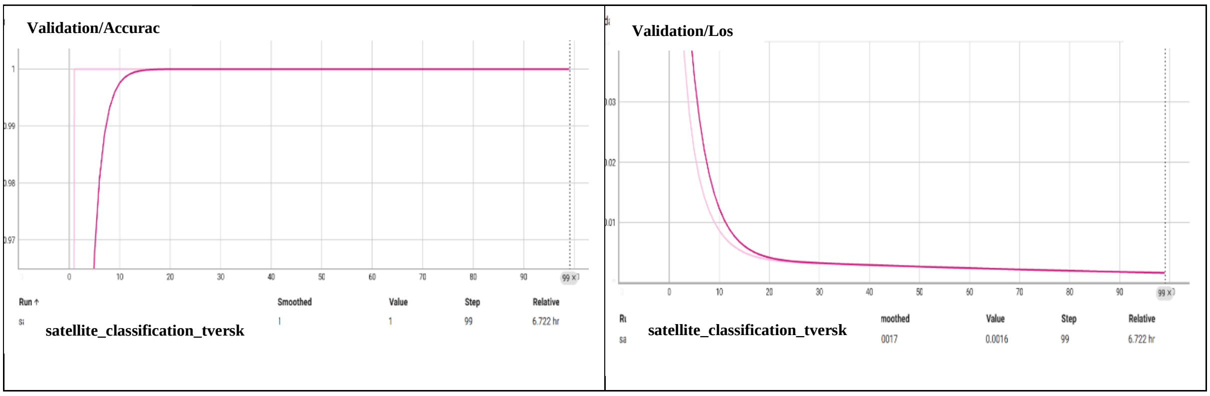

Figure 2. Accuracy and Loss Graphs of the Model

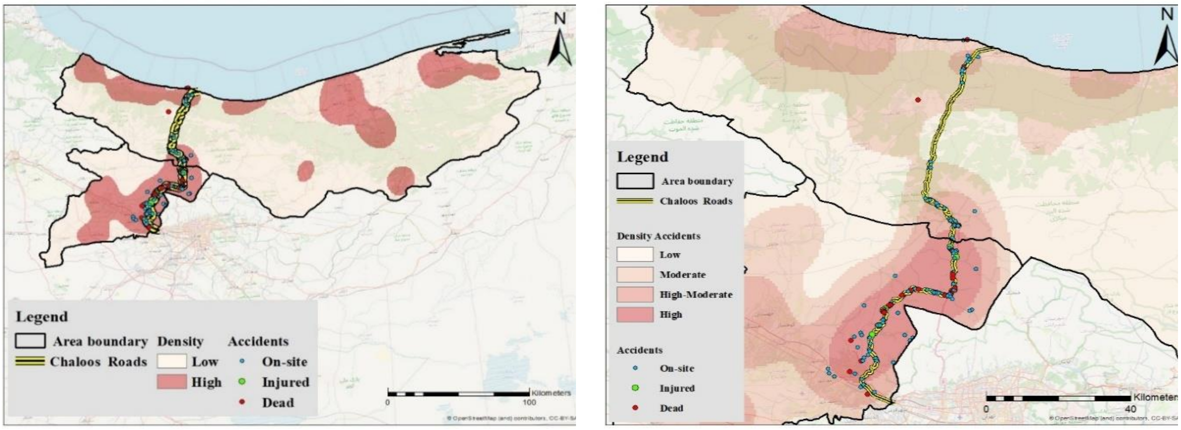

Figure 3. Predicted Road Accidents by the Deep Learning Transformer Model

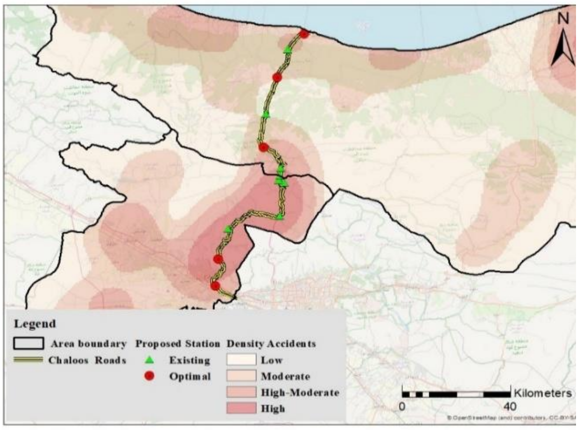

Figure 5. Optimal Location of Rescue Bases

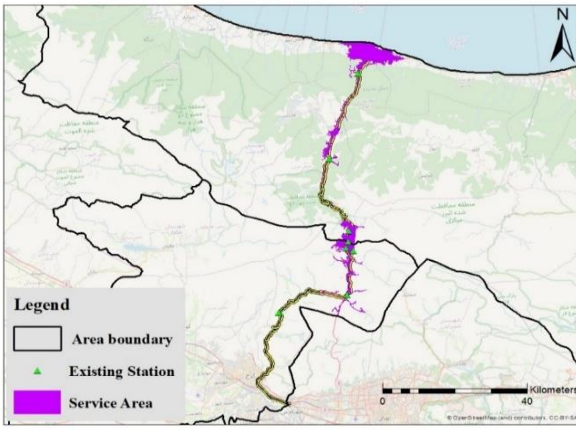

Figure 4. Operational Radius of Existing Bases

The results of the comparison of response time and rescue coverage on the Chalous corridor showed that the average response time for the identified accident-prone locations was approximately 14 minutes and 45 seconds (884.66 seconds), which is close to the 14-minute standard. In contrast, sections of the corridor without rescue coverage had less impact on the average response time due to a lower number of recorded accident-prone locations. Therefore, while the average response time of the current situation seems satisfactory, it does not fully reflect the coverage and efficiency of the entire corridor. The current rescue coverage on the Chalous corridor is 22.77%, which increased to 86.91% with the proposed optimal location of bases. This represents an absolute increase of about 64% in total coverage. Thus, the proposed coverage is nearly 3.8 times that of the current situation. Furthermore, with the optimal location, the response time decreased from approximately 884.66 seconds to around 501.06 seconds (8 minutes and 22 seconds), showing an improvement of about 43% in the speed of emergency response, as shown in Table 2. This significant reduction could directly impact the reduction of injuries and fatalities and enhance the quality of emergency services.

Table 2. Comparison of Response Time and Coverage of Routes in the Current and Proposed Scenarios

Rescue and Relief Base	Chalous Axis		Length of Covered Main Axes (km)	Total Length of Axes (km)
	Covered Axis %	Average Response Time (seconds)		
Existing Status	22.77%	884.66	6795.6803	19349.78
Proposed Status	86.91%	501.055	14673.08	

4. Conclusion

In this study, accident-prone locations on the Chalous corridor were identified using the Transformer deep learning model and real Red Crescent mission data. Then, the optimal placement of rescue bases was determined using the Grey Wolf Optimization algorithm, resulting in the establishment of five new bases in high-accident areas. These changes led to an increase in rescue coverage from 22.77% to 86.91% and a 43% reduction in response time. Overall, the findings of this study demonstrate significant improvements in the quality and speed of rescue services on the Chalous corridor, which could contribute to reducing fatalities and accident-related injuries.

References

[1] Zheng, M., Li, T., Zhu, R., Chen, J., Ma, Z., Tang, M., Cui, Z., & Wang, Z. (2019). Traffic accident's severity prediction: A deep-learning approach-based CNN network. IEEE Access, 7, 45613-45620. https://doi.org/10.1109/ACCESS.2019.2903319.

[2] Soltani, A., Alaedini, F., Shamspour, N., & Ahmadi Marzaleh, M. (2021). Hazard assessment of Iran provinces based on the Health Ministry tool in 2019. Iran Red Crescent Medical Journal, *23*(1), e204. https://doi.org/10.32592/ircmj.2021.23.1.204

[3] Zhang, J.H. (2019). Integration Theory and Optimal Application of the Traffic Accident Management System. In Proceedings of the International Conference on Cyber Security Intelligence and Analytics (CSIA), Shenyang, China, February 2019; Springer International Publishing Ag: Shenyang, China, 2019; pp. 99–104. DOI:10.1007/978-3-030-15235-2_16

[4] Astarita, V., Shaffiee Haghshenas, S., Guido, G., & Vitale, A. (2023). Developing new hybrid grey wolf optimization-based artificial neural network for predicting road crash severity. Transportation Engineering, 12, 100164. https://doi.org/10.1016/j.treng.2023.100164

[5] Goli, A., & Malmir, B. (2019, May 4). A covering tour approach for disaster relief locating and routing with fuzzy demand. International Journal of Intelligent Transportation Systems Research. https://doi.org/10.1007/s13177-019-00185-2

[6] Li, P., Abdel-Aty, M., & Yuan, J. (2020). Real-time crash risk prediction on arterials based on LSTM-CNN. Accident Analysis and Prevention, 135,105371. https://doi.org/10.1016/j.aap.2019.105371

[7] Shang, Q., Feng, L., & Gao, S. (2020). A hybrid method for traffic incident detection using Random Forest-Recursive Feature Elimination and Long Short-Term Memory network with Bayesian Optimization Algorithm. IEEE Access, 8,223513-223522. https://doi.org/10.1109/ACCESS.2020.3047340.

[8] Guo, Y., Jena, R., Hughes, D., Lewis, M., & Sycara, K. (2021). Transfer learning for human navigation and triage strategies prediction in a simulated urban search and rescue task. *Proceedings of the 2021 IEEE International Conference on Robotics and Automation (ICRA),* 1-8. https://doi.org/10.1109/ICRA48506.2021.9562203

[9] Yang, J., Wang, P., Yuan, W., Ju, Y., Han, W., & Zhao, J. (2021). Automatic generation of optimal road trajectory for the rescue vehicle in case of emergency on mountain freeway using reinforcement learning approach. *IET Intelligent Transport Systems*, *15*(10), 1281–1289. https://doi.org/10.1049/itr2.12037
[10] Zhao, W., Yang, Y., & Lu, Z. (2022). Interval short-term traffic flow prediction method based on CEEMDAN-SE noise reduction and LSTM optimized by GWO. Wireless Communications and Mobile Computing, 2022, Article ID 5257353, 16 pages. https://doi.org/10.1155/2022/5257353
[11] Wang, D., Peng, J., Zhao, J., Teng, Y., Xue, W., & Tao, X. (2023, October 10–13). Dual-Transformer: A general model for traffic accident prediction. In 2023 IEEE 98th Vehicular Technology Conference (VTC2023-Fall). IEEE. https://doi.org/10.1109/VTC2023-Fall60731.2023.10333613
[12] Al-Thani, M. G., Sheng, Z., Cao, Y., & Yang, Y., "Traffic Transformer: Transformer-based framework for temporal traffic accident prediction," AIMS Mathematics, vol. 9, no. 5, pp. 12610–12629, Apr. 2024. doi: 10.3934/math.2024617.
[13] Huang, G., Qi, Y., Cai, Y., Luo, Y., & Huang, H. (2024). A Grey Wolf Optimizer Algorithm for Multi-Objective Cumulative Capacitated Vehicle Routing Problem Considering Operation Time. Biomimetics, 9(6), 331. https://doi.org/10.3390/biomimetics9060331
[14] Ahmadi, H., Jelokhani-Niaraki, M., Argany, M., & Ghanbari, A. (2024). Optimizing locations of emergency medical stations for rural areas: A case study in Iran. *International Journal of* Disaster Risk Reduction, 79, Article 104336. https://doi.org/10.1016/j.ijdrr.2024.104336
[15] Jiang, Y., Qu, X., Zhang, W., Guo, W., Xu, J., Yu, W., & Chen, Y. (2025). Analyzing crash severity: Human injury severity prediction method based on transformer model. Vehicles, 7(1), 5. https://doi.org/10.3390/vehicles7010005
[16] Peng, D., & Yan, W. (2025). Test-Time Training with Adaptive Memory for Traffic Accident Severity Prediction. Computers, 14(5), 186. https://doi.org/10.3390/computers14050186
[17] Mousavi, B.S., Jahangir, E., Neysani Samani, N., & Argany, M. (2023). Spatial Analysis of Rescue and Relief Bases in Alborz Province in order to Reduce Hazards. Sci J Rescue Relief, 2023; 15(3): 194-206. acceptance: 27 Jun. 2023. Doi: 10.32592/jorar.2023.15.3.5.
[18] Vaswani, A., Shazeer, N., Parmar, N., Uszkoreit, J., Jones, L., Gomez, A. N., Kaiser, Ł., & Polosukhin, I. (2017). Attention Is All You Need. Proceedings of the 31st Conference on Neural Information Processing Systems (NIPS 2017), Long Beach, CA, USA. https://doi.org/10.48550/arXiv.1706.03762
[19] Wu, H., Xu, J., Wang, J., & Long, G. (2021). Auto former: Decomposition Transformers with Auto-Correlation for Long-Term Series Forecasting. Advances in Neural Information Processing Systems, 34. https://doi.org/10.48550/arXiv.2106.13008

Computational Fluid Dynamics for Sand and Dust Storm Modelling: Physics, Methods, and Real-World Applications

Iraj Gholami[1*], Ali Al-Dousari[2], Ali Al-Hemoud[2], Hassan Al-Dashti[3], Najmeh Neysani Samany[1,4], Ali Darvishi Boloorani[1,4]
[1]GeoAI Environmental Engineering Consultancy L.L.C, Abu Dhabi, UAE,
[2]Kuwait Institute for Scientific Research (KISR), Environmental and Life Sciences Research Center (ELSRC),
[3]Department of Meteorology of Kuwait, Kuwait
[4]Department of Remote Sensing and GIS, Faculty of Geography, University of Tehran, Tehran, Iran.
[*] Corresponding author: igholami@gmail.com, ig@geoai-consulting.com

1. Introduction and Objectives

Sand and dust storms (SDS) are major atmospheric hazards in arid and semi-arid regions, with significant impacts on air quality, human health, critical infrastructure, renewable energy systems and transport safety. Epidemiological and exposure studies show that SDS episodes are associated with increased respiratory and cardiovascular stress, degraded visibility and higher accident risk (Middleton and Kang, 2017). At the same time, SDS play an important role in the Earth system by transporting nutrients, affecting cloud microphysics and altering radiative forcing.
Operational early warning is usually based on numerical weather prediction (NWP) models coupled with dust emission and transport schemes, such as those coordinated under the WMO Sand and Dust Storm Warning Advisory and Assessment System (SDS-WAS) (World Meteorological Organization, 2015). These models resolve synoptic-scale circulation and long-range dust transport at grid spacings of order 10–50 km. However, their coarse resolution prevents them from capturing the detailed interaction between turbulent winds, complex terrain and built infrastructure that controls where erosion initiates, how dust penetrates urban areas, and where sand and dust are deposited around assets.

Computational Fluid Dynamics (CFD) offers a complementary, high-resolution approach. By solving the Navier–Stokes equations in realistic three-dimensional geometries, coupled to sand and dust transport models, CFD can explicitly resolve flow separation, recirculation, near-surface shear and particle trajectories. A recent review by Zong and Wu (2024) demonstrates that CFD has matured into a key tool for studying airflow and sand transport over aeolian landforms, while practitioners increasingly employ CFD for engineering problems such as infrastructure protection and the design of desert solar farms.

The objectives of this contribution are to:

1. Outline the key physical processes and CFD methodologies relevant to SDS modelling;
2. Illustrate, through representative examples, how CFD is used for urban exposure assessment, protection of transport infrastructure, photovoltaic (PV) systems and aviation brownout;
3. Highlight the role of CFD as a bridge between regional dust forecasts and asset-scale risk and mitigation design.

2. Methods and Modelling Framework

2.1 Physical processes

Wind erosion begins when the surface shear stress, often expressed via a friction velocity u_*, exceeds a threshold determined by grain size, density, surface roughness and moisture (Bagnold, 1941). For sand-sized particles (≈70–500 μm), transport is dominated by saltation and creep: grains are lifted, follow ballistic paths and eject further grains upon impact. Finer dust particles (<20 μm) are mobilised either directly by turbulent eddies or indirectly by saltation bombardment. Once lofted, dust can be transported over long distances by mesoscale and synoptic winds (Shao et al., 2002).

Near the ground, the flow is turbulent and strongly influenced by surface roughness, topography and obstacles. Shear layers, separation and recirculation cells generate strong spatial gradients in shear stress and pressure, which in turn control local erosion and deposition patterns. Capturing these structures is essential for realistic prediction of SDS impacts on assets.

2.2 CFD formulation

In SDS applications, the air phase is typically modelled as an incompressible or weakly compressible turbulent flow. The Reynolds-averaged Navier–Stokes (RANS) equations with turbulence closures such as standard/realizable k-ε or k-ω SST (Shear Stress Transport) are widely used for engineering-scale problems because of their robust performance and moderate computational cost (Zong and Wu, 2024). Large-eddy simulation (LES) is applied in cases where unsteady coherent structures are critical, for example in rotorcraft brownout flows, but with higher computational requirements.
Sand and dust are represented either as:

- **Eulerian–Eulerian multiphase flow**, treating the particulate phase as a continuum with its own transport equations for volume fraction and momentum; or
- **Eulerian–Lagrangian discrete particle models**, tracking individual particle parcels through the CFD-resolved flow field under drag, gravity and, where relevant, additional forces.

For saltation and dilute dust clouds around infrastructure and vehicles, the Eulerian–Lagrangian approach is most common. Erosion and deposition are parameterized using threshold friction velocities and empirical or semi-empirical relations, while boundary conditions at the ground specify whether impacting particles stick, rebound or slide.

Boundary conditions are set using atmospheric surface-layer similarity for inflow profiles, rough-wall functions or resolved roughness for the ground, and appropriate pressure or convective conditions at the top and outflow boundaries. Geometries are constructed from digital elevation models (DEMs), GIS data and CAD models of infrastructure and buildings.

3. Representative Applications

3.1 Urban dust exposure

Regional dust models can forecast SDS arrival and bulk concentrations over cities but cannot resolve street-scale variability. Luo et al. (2016) used CFD with RANS turbulence and Lagrangian particle tracking to simulate dust-laden flow in a realistic urban neighborhood. Their results show strong spatial variations in dust concentration at pedestrian height created by building-induced recirculation zones, channeling along street canyons and sheltered courtyards. Such simulations support the siting of sensitive facilities (schools, hospitals), the design of green barriers or dust fences, and the assessment of mitigation strategies in SDS-prone cities.

3.2 Photovoltaic systems in desert environments

Large PV farms in deserts are exposed to both increased mechanical loads and performance losses due to wind-blown sand and dust. Zhang et al. (2024) carried out CFD simulations of wind-blown sand impacting PV modules for different tilt angles and wind directions. They quantified non-uniform pressure fields and particle concentrations around the modules, finding that sand significantly increases drag and uplift forces compared with clean air, particularly at leading edges and corners. Coupled with studies of dust deposition and re-suspension, such simulations support structural design, layout optimization and cleaning strategies for PV systems in dusty regions.

3.3 Transport infrastructure: roads and railways

Roads and railways crossing sandy areas suffer from sand encroachment, ballast fouling and reduced visibility. Raffaele, Coste and Glabeke (2022) introduced a hybrid experimental–numerical framework in which wind-tunnel tests and CFD simulations are combined with structural reliability and life-cycle cost analysis to evaluate sand-mitigation measures. By resolving the flow and particle transport around embankments, fences and berms, CFD helps identify configurations that effectively reduce sand flux onto infrastructure while minimizing costs and avoiding adverse effects elsewhere.

3.4 Aviation and rotorcraft brownout

Brownout arises when rotorcraft operate over loose sand or dust surfaces, lifting dense dust plumes that severely reduce visibility. Caprace et al. (2025) developed an Eulerian dust-transport model coupled with CFD to simulate the brownout plume generated by NASA's Ingenuity helicopter on Mars. Their simulations reproduce observed dust clouds and quantify plume structure as a function of rotor thrust and atmospheric conditions. Similar CFD frameworks are applied to terrestrial helicopters, informing helipad design and operational procedures under dusty conditions.

4. Discussion and Conclusions

CFD has become an essential component of the SDS modelling toolkit, complementing regional dust forecasts and observations by providing high-resolution insight into near-surface flow, sand transport and dust deposition around specific assets. In urban areas, CFD reveals street-level variations in dust exposure that are invisible to coarser models. For PV systems and transport infrastructure, it supports the structural design and optimization of sand-mitigation measures. For aviation, it enables detailed analysis of rotor-induced dust clouds in brownout scenarios, including planetary exploration.

Significant challenges remain. Input uncertainties in surface properties and boundary-layer conditions, empirical entrainment and deposition parameterizations, and limited field data for validation all affect model accuracy (Middleton and Kang, 2017; Zong and Wu, 2024). Computational cost constrains domain size and the use of high-fidelity LES or CFD–DEM. Nevertheless, CFD is already providing actionable comparative assessments between alternative designs and mitigation options, even where absolute prediction is uncertain (Raffaele et al., 2022; Zhang et al., 2024).

Future work will likely focus on tighter multi-scale coupling between regional dust-forecast systems and local CFD "nests", expanded use of CFD–DEM to improve process parameterizations, and machine-learning-based surrogates to accelerate scenario exploration (Alshammari, Alrwais and Aksoy, 2022). As SDS risks grow with land-use change and climate variability, integrating CFD into operational SDS services and infrastructure planning will be increasingly important.

References

Alshammari, R.K., Alrwais, O. and Aksoy, M.S. (2022) 'Machine learning applications to dust storms: A meta-analysis', *Aerosol and Air Quality Research*, 22(12), p. 220183.

Bagnold, R.A. (1941) *The Physics of Blown Sand and Desert Dunes*. London: Methuen.

Caprace, D.-G., Baker, E., Ventura Diaz, P. and Yoon, S. (2025) 'Planetary helicopter brownout simulation of Ingenuity using a Eulerian dust transport model', *AIAA Journal*, 63(10), pp. 4393–4408.

Luo, K., Yu, H., Dai, Z., Fang, M. and Fan, J. (2016) 'CFD simulations of flow and dust dispersion in a realistic urban area', *Engineering Applications of Computational Fluid Mechanics*, 10(1), pp. 228–242.

Middleton, N. and Kang, U. (2017) 'Sand and dust storms: Impact mitigation', *Sustainability*, 9(6), p. 1053.

Raffaele, L., Coste, N. and Glabeke, G. (2022) 'Life-cycle performance and cost analysis of sand mitigation measures: Toward a hybrid experimental–computational approach', *Journal of Structural Engineering*, 148(7), p. 04022082.

Shao, Y., Jung, E. and Leslie, L.M. (2002) 'Numerical prediction of Northeast Asian dust storms using an integrated wind erosion modelling system', *Journal of Geophysical Research: Atmospheres*, 107(D24), p. 4814.

World Meteorological Organization (2015) *Sand and Dust Storm Warning Advisory and Assessment System (SDS-WAS): Science and Implementation Plan 2015–2020*. Geneva: WMO.

Zhang, K., Zhang, H., Liu, B. et al. (2024) ‘Numerical simulation study on the impact of wind-blown sand action on the loading of photovoltaic systems’, *Physics of Fluids*, 36(7), p. 075166.
Zong, Q. and Wu, X. (2024) ‘A review of computational fluid dynamics (CFD) methodology and analysis on airflow and sand transport over aeolian landforms’, *Catena*, 241, p. 108010.

Advancing Turbidity Monitoring in Gorgan Bay: Integrating Landsat-8 Data with Regression and Machine Learning for Water Quality Mapping

Salar Khani [1], Ata A. Kakroodi[1], Sara Attarchi [1]

1-Department of Remote Sensing and GIS, University of Tehran, P.O. Box 14155-4665, Tehran, Iran

Abstract

Gorgan Bay, an important ecosystem in the southeast Caspian Sea, supports rich biodiversity, sustainable water resources, and regional economic stability. However, in recent years, there has been a notable decrease in the volume and degradation of water quality owing to increasing human activities and climate change. This study introduces an approach for monitoring the turbidity of the bay using satellite imagery. In the first step, regression models were created to establish linear, polynomial, and exponential relationships between in-situ turbidity measurements and Landsat-8 band reflectance data. To evaluate the model's performance on unseen test data, metrics such as the Root Mean Squared Error (RMSE), coefficient of determination (R^2), and scatter plots of estimated versus observed turbidity values were used. With $R^2 = 0.84$, the linear model outperformed polynomial ($R^2 = 0.72$) and exponential ($R^2 = 0.54$) fits, demonstrating the effectiveness of Landsat-8 green, red, and blue bands for estimating turbidity. Subsequently, a Random Forest (RF) machine learning model was used to further improve the accuracy of turbidity estimation. This model performed better than the conventional regression fits, increasing the accuracy of turbidity estimation by 11%. It also produced the lowest RMSE for all methods and an improved $R^2 = 0.93$. The best-performing models were used to generate turbidity distribution maps across the bay. This approach offers reliable and real-time water quality evaluation, which provides practical insights for environmental management, policymaking, and conservation strategies in dynamic coastal waters.

Keywords: Gorgan Bay, Water Turbidity, Satellite Imagery, Regression Fit, Random Forest

1. Introduction

Water is one of the most important elements of nature, and the survival of humans and other creatures depends heavily on clean water resources. Water-related studies have historically focused on the quantity and trends of available water. However, the declining quality of water resources worldwide has, in recent decades, brought increased attention to the necessity of water quality monitoring in conjunction with quantitative assessments (Wang et al., 2024).

Turbidity is one of the crucial and widely used indicator for water quality status of a water body (Ma et al., 2025). It refers to the extent to which light is scattered or blocked by particulate matter suspended in the water (Ma et al., 2021). Elevated suspended particulate matter levels increase turbidity level,s hindering light penetration, which is critical for photosynthesis (Ma et al., 2025).

Monitoring the turbidity of coastal waters is essential because it influences marine ecosystems and human health (Kong et al., 2025). Owing to the significant correlation between turbidity and total suspended solids, cost-effective turbidity monitoring techniques may be utilized to approximate total suspended solids (Ayana, 2019). The main purposes of any turbidity monitoring program include determining whether the water is safe for drinking, detecting increased pollution caused by storms and river discharges, monitoring the extent of erosion and sediment load, and identifying links with the biological features of water, such as primary production (Voichick et al., 2017).

Conventional methods for quantifying the turbidity of a water body include turbidimeters, nephelometric analyses, and spectrophotometric techniques (Santos et al., 2025). However, these methods are costly, time consuming, susceptible to human error, and lack the capability for real-time turbidity monitoring (Matos et al., 2024). In contrast, remote sensing serves as a cost-effective source of data that can be used for real-time monitoring of turbidity and other water quality variables using regression and machine learning (ML) methods. Recently, Sentinel-2 and Landsat series of satellites have been widely used to extract water turbidity data (Azad Hossain et al., 2021; Kong et al., 2025; Santos et al., 2025; Ma et al., 2025).

Azad Hossain et al. (2021) used Landsat 8 satellite image and in situ measurements to estimate turbidity of Tennessee River, USA applying regression-based numerical models. The nonlinear regression fit utilizing Band 4 (red) surface reflectance values of the Landsat 8 OLI sensor with $R^2 = 0.97$ and RMSE = 1.41 NTU provided accurate turbidity estimations. Memari et al. (2024) used ML, numerical computations, and satellite data to predict turbidity of Lake Erie in the USA reaching an accuracy of $R^2 = 0.93$. Ma et al. (2025) used Sentinel-2 data with fuzzy c-means method with a weighted blending CNN-RF deep learning model to predict turbidity in lakes and reservoirs of Northeast China. Their proposed method provided accurate turbidity estimations, with $R^2 = 0.900$ and RMSE=11.698 NTU.

Santos et al. (2025) employed Sentinel-2 spectral bands with the XGBoost model to estimate turbidity across Mississippi River stations. Their approach yielded turbidity estimates with $R^2 = 0.75$. Kong et al. (2025) implemented correlation analysis and Random Forest (RF) model to monitor turbidity of Los Angeles coastal waters. The RF model, with $R^2 = 0.632$, outperformed the correlation method, with $R^2 = 0.451$. Wu et al. (2025) conducted a comprehensive review of turbidity monitoring in coastal waters using satellite data and ML models.

A literature review revealed that great attention has recently been given to turbidity monitoring in water bodies. Various machine learning and regression models have been implemented to link in-situ measurements to satellite image band reflectance values.

The aim of this study was to monitor the turbidity of Gorgan Bay, Southeastern Caspian Sea using regression and machine learning models. The models were trained and validated using Landsat 8 image and turbidity measurements. Subsequently, the most accurate models were used to generate turbidity spatial maps to identify the turbidity gradients and hotspots across the bay.

2. Methodology

2.1. Study Area

The largest bay in the Caspian Sea, Gorgan Bay, is located southeast of the sea between latitudes 36°46' and 37°0' North and longitudes 53°25' to 54°6' East (Gharibreza et al., 2018). The Ashuradeh Channel connects the bay to Caspian Sea. The bay depth increases from west to east and toward Ashuradeh Island's southern regions, with an average depth of less than 1.5 meters and a maximum depth of 6.5 meters. The bay has a maximum length of 70 km and total area of approximately 400 km² (Kheirabadi et al., 2018). It was among the first wetlands to be registered under the Ramsar Convention for the Conservation of Wetlands in 1975.

2.2. In situ and Satellite Data

In this study, in situ turbidity measurements across the bay collected on September 13, 2020, by the Iranian National Institute for Oceanography and Atmospheric Science were used. The minimum and maximum turbidity within the bay were recorded as 0.98 FTU and 149.69 FTU, respectively. Approximately, 70% of the data was used to train the models and the remaining set was used to validate their performance. Landsat 8 image acquired on September 12, 2020 was also considered to extract link between actual turbidity and satellite image band reflectance values.

2.3. Methods

For turbidity monitoring, measured turbidity data was fitted to the reflectance values of different bands of Landsat 8 image. The fitting was performed in linear, polynomial, and exponential forms, generating regression equations capable of turbidity extraction using Band 1 to Band 7 reflectance data of Landsat 8 image. These regression fitting methods were considered due to their simplicity, that enables researchers to gain an initial view of the changes in water quality.

Subsequently, to achieve more accurate results, Random Forest (RF) machine learning was implemented. RF is a method developed by Breiman (2001). RF is an ensemble of decision trees used for classification and regression that provides a more stable and accurate prediction by voting or averaging the outputs. In this study, same to the regression fitting methods, RF model was also trained using the train subset and then validated against test data. The performance of all models was examined using Root Mean Squared Error (RMSE) and coefficient of determination (R^2) with their formula presented in Equation 1 and 2. The most accurate models were used for turbidity mapping across Gorgan Bay.

$$R^2 = \frac{\sum_{i=1}^{n}\left(WQ_{i(estimated)} - WQ_{i(mean)}\right)^2}{\sum_{i=1}^{n}\left(WQ_{i(observed)} - WQ_{i(mean)}\right)^2} \qquad (1)$$

$$RMSE = \sqrt{\frac{\sum_{i=1}^{n}\left(WQ_{i(observed)} - WQ_{i(estimated)}\right)^2}{n}} \qquad (2)$$

3. Results and Discussion

Figure (1) shows the results of fitting the actual turbidity values of the training data to various bands of Landsat 8 using linear fitting (left column), quadratic polynomial fitting (middle column), and exponential fitting (right column). The generated fitting equations from the three methods were then used to estimate the turbidity values at the test stations to evaluate the generalizability of these relationships in extracting turbidity in Gorgan Bay.

The linear, polynomial, and exponential regression equations obtained for extracting water turbidity values using the single-band fitting methods from Landsat 8, along with the corresponding goodness-of-fit criteria of R^2 and RMSE error of these methods for the test data, are summarized in Table (1). The highest accuracy of turbidity estimation was obtained using the blue, green, and red bands reflectance values. Among the three fitting methods, the linear fit using the green band reflectance data, with RMSE = 10.93 FTU and R^2=0.84, resulted in the most accurate turbidity estimations. The performance of the RF model for the test data is presented in Table (1) as well. It can be seen that this model, with RMSE = 9.54 FTU and R^2 = 0.93, provided the highest performance for turbidity estimations using green band reflectance data.

Table 1. The generated regression equations and performance of the models for turbidity estimation from Landsat 8 band reflectance values

Band	Band	Regression	Obtained Equation	R^2	RMSE
SR_B1	Ultra-Blue (Coastal aerosol)	Linear	$15.703\rho^{*} + 37.684$	0.43	13.60
		Polynomial	$-2291.8\rho^2 + 161.57\rho + 36.48$	0.66	18.76
		Exponential	$11.192e^{25.796\rho}$	0.60	11.29
		Random Forest	-	0.38	14.31
SR_B2	Blue	Linear	$361.9\rho + 25.71$	0.66	15.18
		Polynomial	$-13204\rho^2 + 1587.8\rho + 5.1389$	0.72	14.13
		Exponential	$\mathbf{5.9457e^{35.845\rho}}$	**0.54****	**11.13**
		Random Forest	-	**0.51**	**13.01**
SR_B3	Green	**Linear**	$\mathbf{725.23\rho - 15.068}$	**0.84**	**10.93**
		Polynomial	$-6692.7\rho^2 + 1672.4\rho - 42.931$	0.88	14.25
		Exponential	$0.9513e^{41.704\rho}$	0.61	11.23
		Random Forest	**-**	**0.93**	**9.54**
SR_B4	Red	Linear	$939.88\rho + 0.0268$	0.66	11.96
		Polynomial	$\mathbf{-13599\rho^2 + 2029.9\rho - 16.685}$	**0.72**	**14.06**
		Exponential	$2.1927e^{54.862\rho}$	0.47	13.92
		Random Forest	-	0.45	15.42
SR_B5	NIR	Linear	$-206.93\rho + 39.436$	0.32	20.34
		Polynomial	$-46420\rho^2 + 1431\rho + 36.354$	0.41	17.16
		Exponential	$17.346e^{22.399\rho}$	0.30	15.67
		Random Forest	-	0.46	14.59
SR_B6	SWIR1	Linear	$-658.86\rho + 42.138$	0.24	20.12
		Polynomial	$-320860\rho^2 + 5103.7\rho + 22.662$	0.28	19.17
		Exponential	$16.607e^{31.271\rho}$	0.24	16.29
		Random Forest	-	0.40	13.03
SR_B7	SWIR2	Linear	$354.97\rho + 35.962$	0.1	19.05
		Polynomial	$-847750\rho^2 + 12870\rho - 4.81$	0.07	19.42
		Exponential	$14.077e^{61.354\rho}$	0.10	16.60
		Random Forest	-	0.00	19.64

*; ρ denotes the surface reflectance of the Landsat-8 image bands

**; Bold values indicate the best performance of the corresponding method.

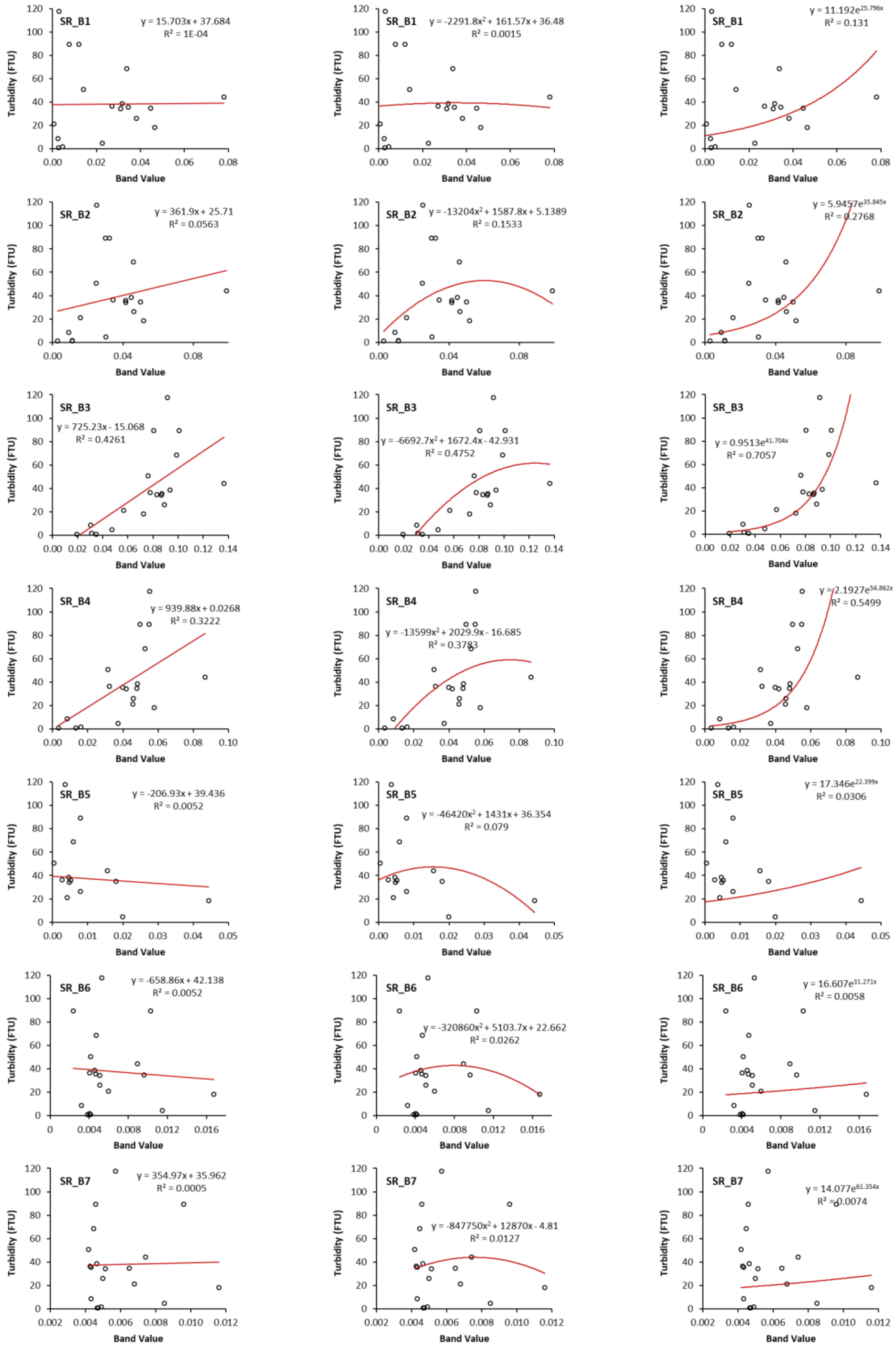

Figure 1. Regression plots of turbidity and reflectance values of Landsat 8 bands; linear fit (left column), polynomial fit (middle column), and exponential fit (right column).

The most accurate results of water turbidity estimation using linear, polynomial, exponential fitting methods, and the RF model are shown in Figure (2). This figure shows the scatter plots of estimated against measured water turbidity values at the test stations. The better performance of the RF model compared to the fitting methods is evident from this figure.

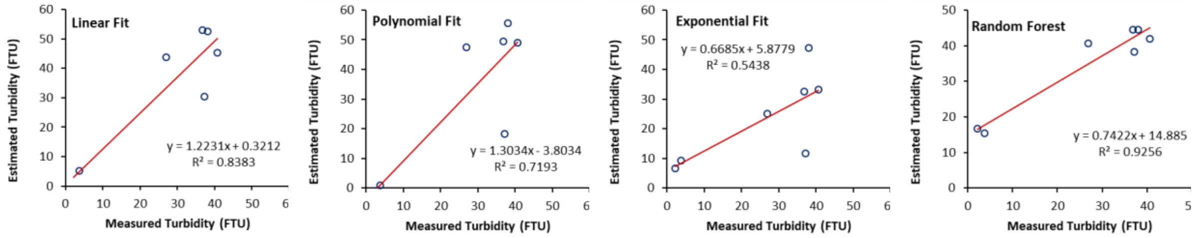

Figure 2. Scatter plots of estimated against actual water turbidity values at test stations by linear, polynomial, and exponential fitting and random forest model.

In the next step, the linear, polynomial, and exponential regression equations were used to produce Gorgan Bay turbidity distribution maps, which can be seen in Figure 3. The same turbidity spatial map was also obtained for the RF model. It can be seen that the exponential fitting method tends to provide lower estimates for turbidity values. In addition, the exponential method estimated very high turbidity values for some areas of the Gorgan Bay, which could be due to the exponential nature of the regression relationship obtained for this method. Therefore, considering the performance of this method at test stations, the upper limit of the output of this method was limited to 60 FTU to better display the results. The linear and polynomial methods provided relatively similar turbidity distribution patterns across the bay. The areas with high-level turbidity can be easily distinguished from the RF-generated turbidity map, showing the center and southeastern regions of the bay as high-level turbidity hotspots.

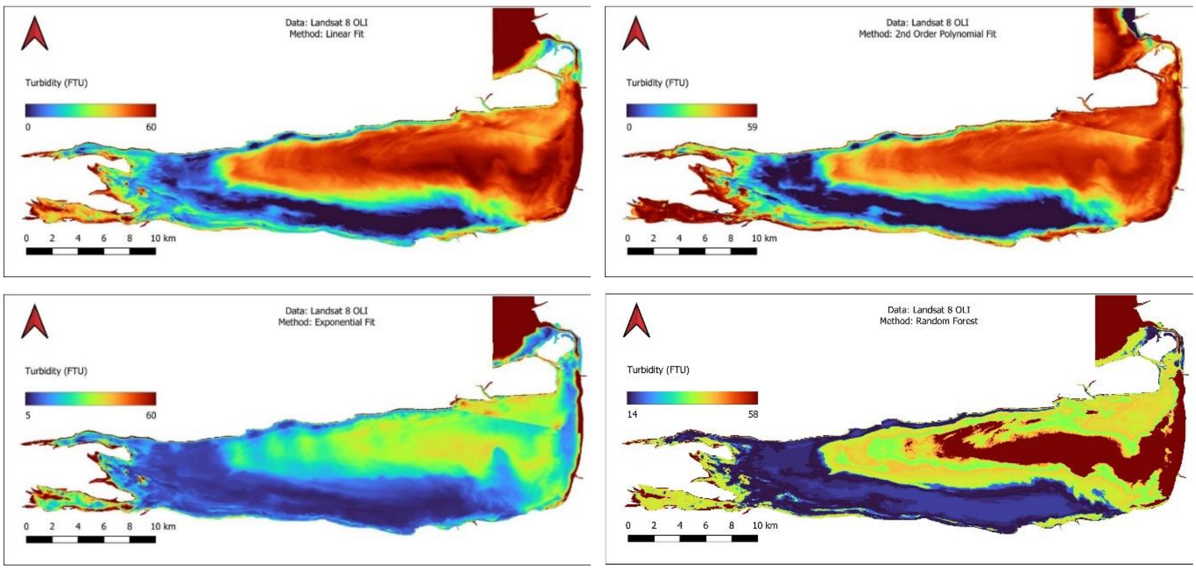

Figure 3. Gorgan Bay turbidity spatial maps by linear, polynomial, and exponential fitting and random forest model.

4. Conclusion

In the current research, the capability of simple regression fitting and machine learning for Gorgan Bay turbidity retrieval from Landsat 8 imagery was explored. The results show that the green, red, and blue bands of Landsat 8 band reflectance data provided the highest accuracy in estimating water turbidity with linear, polynomial, and exponential fitting, respectively. From the fitting methods, corresponding regression equations capable of estimating turbidity values from Landsat 8 band reflectance data were generated. These equations can be used as a fast method for real-time monitoring of turbidity in the bay.

Among the four models, the RF model provided the highest performance for estimating turbidity using green band reflectance data.

The turbidity distribution pattern across Gorgan Bay is almost similar for the two linear and polynomial fitting methods and shows an increase in turbidity values from west to east. In addition, the RF-generated turbidity maps enable the detection of high turbidity levels in the area near the confluence of the Qarasu River with Gorgan Bay, which is evidence for the large sediment load discharge from this river into Gorgan Bay.

The findings of this study demonstrate the capability of remote sensing data coupled with regression and machine learning approaches for water turbidity mapping. The outcome of this research can be used by water resource managers and policymakers to adjust conservation strategies to preserve Gorgan Bay water quality through continuous monitoring, enabling timely and cost-effective management practices.

References

Ayana, E. (2019). *Determinants of declining water quality*. World Bank Group.

Breiman, L. (2001). Random forests. *Machine learning*, *45*(1), 5-32.

Gharibreza, M., Nasrollahi, A., Afshar, A., Amini, A. and Eisaei, H., 2018: Evolutionary trend of the Gorgan Bay (southeastern Caspian Sea) during and post the last Caspian Sea level rise. *Catena*, *166*, pp.339-348.

Kheirabadi, H., Noori, R., Samani, J.M., Adamowski, J.F., Ranjbar, M.H. and Zaker, N.H., 2018: A reduced-order model for the regeneration of surface currents in Gorgan Bay, Iran. *Journal of Hydroinformatics*, *20*(6), pp.1419-1435.

Kong, Y., Jimenez, K., Lee, C. M., Winter, S., Summers-Evans, J., Cao, A., ... & Jay, J. A. (2025). Monitoring Coastal Water Turbidity Using Sentinel2—A Case Study in Los Angeles. *Remote Sensing*, *17*(2), 201.

Ma, Y., Chen, Q., Song, K., Yang, Q., Zheng, Q., & Ma, Y. (2025). An Optical Water Type-Based Deep Learning Framework for Enhanced Turbidity Estimation in Inland Waters from Sentinel-2 Imagery. *Sensors (Basel, Switzerland)*, *25*(20), 6483.

Ma, Y., Song, K., Wen, Z., Liu, G., Shang, Y., Lyu, L., ... & Hou, J. (2021). Remote sensing of turbidity for lakes in northeast China using Sentinel-2 images with machine learning algorithms. *IEEE Journal of Selected Topics in Applied Earth Observations and Remote Sensing*, *14*, 9132-9146.

Matos, T., Martins, M. S., Henriques, R., & Goncalves, L. M. (2024). A review of methods and instruments to monitor turbidity and suspended sediment concentration. *Journal of Water Process Engineering*, *64*, 105624.

Memari, S., Phanikumar, M. S., Boddeti, V., & N. Das, N. (2024). Turbidity assessment in coastal regions combining machine learning, numerical modeling, and remote sensing. *Journal of Hydroinformatics*, *26*(10), 2581-2600.

Santos, V., Rocha, P., & Gharabaghi, B. (2025). Evaluation of deep learning methods for forecasting turbidity in river networks using sentinel-2 remote sensing data. *Bahram, Evaluation of Deep Learning Methods for Forecasting Turbidity in River Networks Using Sentinel-2 Remote Sensing Data*.

Voichick, N., Topping, D. J., & Griffiths, R. E. (2018). False low turbidity readings from optical probes during high suspended-sediment concentrations. *Hydrology and Earth System Sciences*, *22*(3), 1767-1773.

Wang, M., Bodirsky, B. L., Rijneveld, R., Beier, F., Bak, M. P., Batool, M., ... & Strokal, M. (2024). A triple increase in global river basins with water scarcity due to future pollution. *Nature Communications*, *15*(1), 880.

Wu, Z., Pang, J., Li, J., Wang, Y., Ruan, J., Zhang, X., ... & Gao, Y. (2025). A review of remote sensing-based water quality monitoring in turbid coastal waters. *Intelligent Marine Technology and Systems*, *3*(1), 1-18.

Spatiotemporal Monitoring of Water Resources in the Helmand River Basin Using Satellite Data

Saeid. Hamzeh*[1], Eslam. Galehban[2], Seyed Kazem. Alavipanh[3]

[1] Department of Remote Sensing and GIS, Faculty of Geography, University of Tehran, *Corresponding Author: saeid.hamzeh@ut.ac.ir
[2] Department of Remote Sensing and GIS, Faculty of Geography, University of Tehran, galehban.eslam@ut.ac.ir
[3] Department of Remote Sensing and GIS, Faculty of Geography, University of Tehran, Salavipa@ut.ac.ir

Abstract

The management of transboundary water resources presents significant challenges, especially in regions with shared water bodies. This study focuses on the Helmand River Basin (HRB), shared by Iran and Afghanistan, where disputes over water allocation exist. The objective of this research is to analyze key historical drivers of water resources in the HRB over the past two decades, utilizing satellite and reanalysis datasets to monitor parameters such as reference evapotranspiration (ETo), precipitation, snow water equivalent (SWE), snow cover (SC), and land use/land cover (LULC). The results indicate that ETo has shown no significant long-term variation, with the lowest values observed in higher elevation areas. Precipitation patterns in the basin have exhibited considerable variability, with an increasing trend in precipitation, particularly after 2010. Snow cover has shown notable changes. Regarding land use, agricultural area in the basin has increased from 111,000 hectares in 2000 to 216,000 hectares in 2020, resulting in a 93.5% rise in agricultural water consumption. This growth in agricultural land and water use underscores the pressure exerted by human activities on the basin's water resources. Findings suggest that inefficient irrigation methods and the expansion of agricultural land, especially in the middle reaches of the basin, have contributed to a reduction in downstream water availability, intensifying water scarcity issues in the region.

Keywords: Transboundary basins, Gridded datasets, hydro political, Sustainability

1. Introduction

Sharing transboundary water resources presents significant challenges for riparian states, as more than half of the world's freshwater is found in shared bodies, with most of the global population depending on them (Albert et al., 2021). Over 300 treaties have been established to manage these resources, but non-compliance remains a key cause of disputes, particularly in regions like the Middle East, where population growth and diminishing water resources worsen the issue (Giordano et al., 2014). Disputes over shared water resources include the Tigris-Euphrates River (Turkey, Syria, Iraq), the Ganges River (India, Bangladesh), and the Mekong River (China, Laos, Cambodia, Thailand, Vietnam) (Cullen & Demenocal, 2000; Babel & Wahid, 2008). A similar situation exists in the Helmand River Basin (HRB), shared by Iran and Afghanistan, where ongoing disagreements over water allocation persist. The situation is further complicated by the basin's location in an arid region with limited water resources (Bidabadi & Afshari, 2020; Hussainzada et al., 2023). Despite the signing of a treaty between Iran and Afghanistan in 1973, non-compliance has led to water security issues and ecosystem collapse in the Sistan Delta. Afghanistan claims that climate change and changing precipitation patterns have significantly reduced renewable water resources, while Iran disagrees with this claim (Thomas et al., 2015). The lack of reliable data agreed upon by both countries has been a persistent issue, hindering informed decision-making and policy development.

Many countries fail to share transboundary water data regularly, and political challenges complicate the establishment of consensus on reliable data (Gerlak et al., 2011; Heggy et al., 2021). Remote sensing and reanalysis datasets provide valuable tools to address such challenges, offering reliable data for monitoring water resources, especially in areas where in-situ measurements are difficult to obtain (Veysi et al., 2024; Jafarpour et al., 2022). These datasets are particularly effective in data-scarce regions and can assist in resolving water disputes by providing objective, transparent information. This research aims to analyze key historical drivers of water resources in the HRB over the past two decades, focusing on parameters such as evapotranspiration, precipitation, snow water equivalent, snow cover, and land use/land cover (LULC) using gridded datasets. The study's significance lies in its comprehensive examination of all relevant parameters influencing water resources in the region.

2. Materials and Methods

Study Area:

The Helmand Basin, primarily located in Afghanistan, covers an area of 367,000 km², spanning latitudes 29°N to 35°N and longitudes 60°E to 69°E, with small portions in Iran and Pakistan (Fig. 1). Key rivers in the basin include the Helmand, Ghazni, Harout, Arghandab, and Farah Rivers, fed by rain and snowmelt from the Hindukush Mountains. The Helmand River, the longest international river in Afghanistan at 1050 km, experiences over 80% of its flow from February to June (Thomas and Kidd, 2015; 2017). The basin's elevation ranges from 4000 m in the northeast to 500 m in the southwest (Rashki et al., 2015).

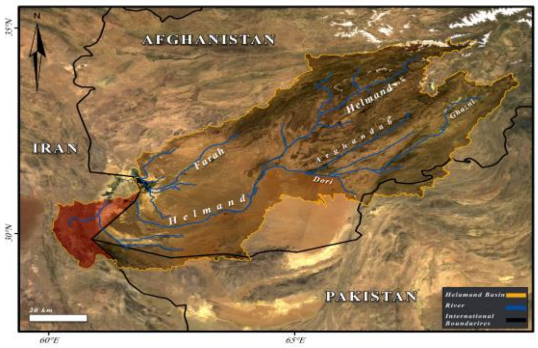

Figure 1 Location of Helmand's basin among three countries (Afghanistan, Iran, Pakistan)

Satellite Data and Preprocessing:

This research utilizes various datasets. The Land Use Land Cover (LULC) of the study area was evaluated using the MCD12Q1 product, while Reference Evapotranspiration (ETo) was estimated using ERA5 data (temperature, dew point, wind speed) from the Copernicus Climate Data Store (Allen et al., 1998). The FAO Penman-Monteith equation was applied to calculate ETo. Actual Evapotranspiration (ETa) was derived using the SSEBop algorithm, based on MODIS products for land surface temperature (LST) and albedo (Senay et al., 2013). For the SWE (snow water equivalent) and precipitation, data from CHIRPS and the FLDAS global model were used, resampled to 1 km resolution.

Statistical and Trend Analysis:

The Mann-Kendall test was applied to analyze trends in hydrological and meteorological data, detecting monotonic trends (increasing or decreasing) in time series. The Rainfall Anomaly Index (RAI) was also used to evaluate deviations in annual and monthly precipitation (Rooy et al., 1965; Fernandes et al., 2010).

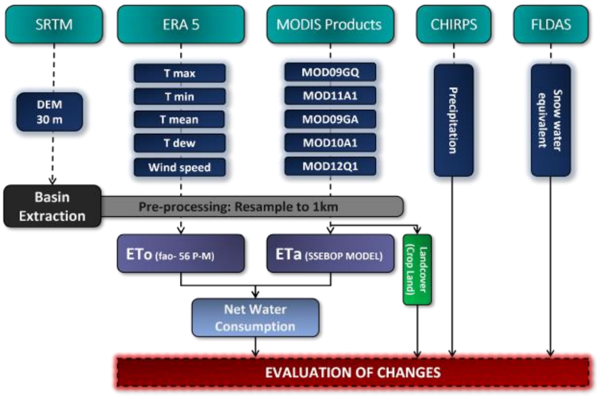

Figure 2 Conceptual framework of Research

3. Results

The annual time series of average reference evapotranspiration (ETo) values, calculated from the ERA5 dataset for the period 2000 to 2020, ranged from 303 to 3104 mm/year, following a normal distribution. Over the past two decades, ETo showed no significant changes, with the lowest values found in high-elevation areas (above 2500 meters), where temperatures are lower and snow cover limits evapotranspiration rates. High ETo values were recorded in the southwestern parts of the basin, particularly in the downstream regions, where the arid conditions exacerbate water limitations. These fluctuations in ETo have a notable impact on crop water requirements, especially given the region's vulnerability to water scarcity.

Precipitation patterns in the Helmand Basin showed considerable variability between 2000 and 2020. The highest recorded annual precipitation was 253 mm in 2019, while the lowest was 93 mm in 2000. February typically saw the highest monthly precipitation, while September experienced the lowest (Fig. 3). The region's eastern part, influenced by the summer monsoon from the Indian Ocean and Arabian Sea, saw fluctuating precipitation levels. The trends from 2004 to 2010 indicated an increase in precipitation, with significant drops observed in 2014 and 2015, yet overall, rainfall remained above average for most years. This precipitation variation is critical for the water resources in the basin, which are highly dependent on snowmelt from the mountains.

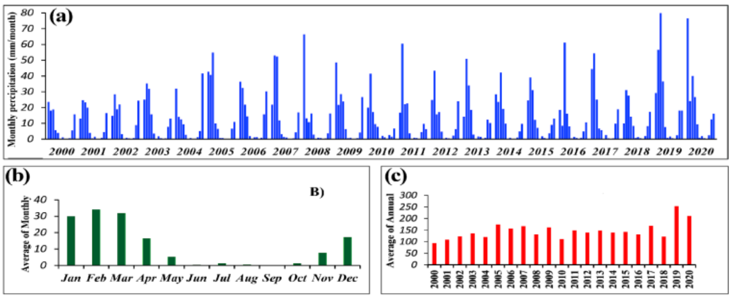

Figure 3: Time series of precipitation in the Helmand Basin from 2000 to 2020: (a) Monthly precipitation anomalies (mm/year), (b) Monthly average precipitation (mm/month), and (c) Annual average precipitation (mm/year).

Changes in snow cover (SC) were also notable, with no significant decline in the annual snow cover. However, certain years such as 2008 showed higher SC, and others like 2018 had lower SC. Snow cover typically peaks in December and disappears by late May, with a general decline in spring SC over the last 20 years. The snow season also ended earlier, and autumn snow cover showed an upward trend, influencing the timing and volume of snowmelt, which directly affects water availability in the basin. The snow water equivalent (SWE), which typically peaks in February, showed variability throughout the years. Although there were fluctuations, no significant long-term decrease was observed. The pattern of SWE trends mirrored snow cover trends, with a slight decrease observed from 2003 to 2013, followed by an upward trend after 2013. Agricultural land use in the basin increased dramatically from 111,000 ha in 2000 to 216,000 ha in 2020, a rise of 93.49%.

This expansion of cropland resulted in a significant increase in agricultural water consumption, from 1.5 BCM to 3.2 BCM. This growth in agricultural land and water use highlights the pressure human activities place on the basin's water resources. Despite this increase, the efficiency of irrigation practices remains a concern, with ETa closely linked to irrigation water use. The large discrepancy between actual water consumption and the cropland area suggests inefficient irrigation methods, which contribute to water scarcity and environmental degradation (Fig. 4). The analysis of precipitation versus actual evapotranspiration (P-ETa) and land use land cover (LULC).

Further highlights that the middle-reach croplands in the Helmand basin utilize a substantial proportion of the available water resources. This has resulted in limited water flow downstream, further stressing water availability in the region and impacting downstream communities. Careful management of land-use changes and agricultural practices is essential to ensure sustainable water resource usage and mitigate adverse effects on water flow. Statistical trend analysis using the Mann-Kendall test revealed a general decline in ETo, particularly in spring, while precipitation showed a significant upward trend across all seasons. The decrease in snow cover suggests shifts in precipitation patterns, while SWE showed no significant trends in either annual or seasonal scales (Fig. 5).

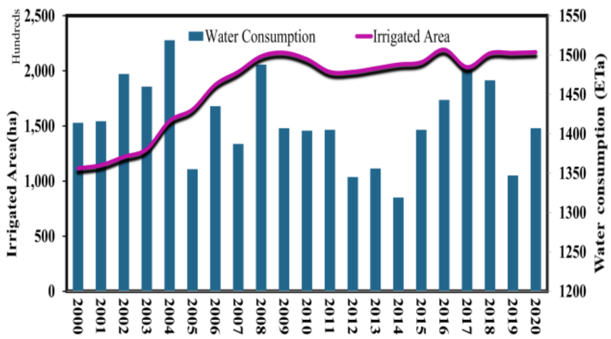

Figure 4: The value of Water consumption in cropland of the Helmand basin

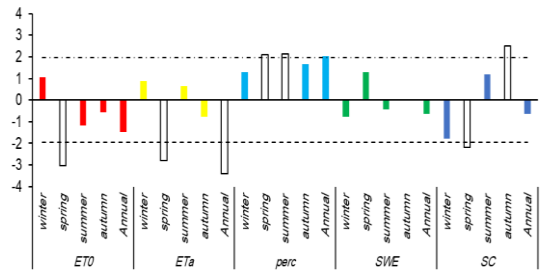

Figure 5: Seasonal and annual trend analysis of the Mann–Kendall test

4. Conclusion

This study highlights the status of water resources in the Helmand Basin, showing fluctuations in key parameters such as evapotranspiration (ETo), precipitation, snow cover (SC), and snow water equivalent (SWE) over the past two decades. While no significant decline in overall water availability was observed, a 93.5% increase in agricultural land and a rise in agricultural water consumption from 1.5 BCM to 3.2 BCM indicate that human activities are a major factor in reducing downstream water availability.The research emphasizes the importance of effective transboundary water management through cooperation between Iran and Afghanistan. The use of satellite-based and reanalysis datasets can provide objective tools for resolving water conflicts, even in the absence of agreed-upon hydrological data. Enhanced technical capacity for data collection and analysis is crucial, and fostering collaboration between institutes and universities in the region could lay the foundation for formal intergovernmental cooperation.

References

[1] Albert, J. S., Destouni, G., Duke-Sylvester, S. M., Magurran, A. E., Oberdorff, T., Reis, R. E., & Ripple, W. J. (2021). Scientists' warning to humanity on the freshwater biodiversity crisis. Ambio, 50(1), 85-94. https://doi.org/10.1007/s13280-020-01318-8.

[2] Giordano, M., Drieschova, A., Duncan, J. A., Sayama, Y., De Stefano, L., & Wolf, A. T. (2014). A review of the evolution and state of transboundary freshwater treaties. International Environmental Agreements: Politics, Law and Economics, 14(3), 245-264. https://doi.org/10.1007/s10784-013-9211-8.

[3] Cullen, H. M., & Demenocal, P. B. (2000). North Atlantic influence on Tigris–Euphrates streamflow. International Journal of Climatology: A Journal of the Royal Meteorological Society, 20(8), 853-863. https://doi.org/10.1002/1097-0088(20000630)20:8<853::AID-JOC497>3.0.CO;2-M.

[4] Babel, M.S. and Wahid, S.M. (2008), Freshwater Under Threat: South Asia – Vulnerability Assessment of Freshwater Resources to Environmental Change, UNEP, Nairobi.

[5] Bidabadi, F. S., & Afshari, L. (2020). Human right to water in the Helmand Basin: Setting a path for the conflict settlement between Afghanistan and Iran. Utrecht Law Review, 16(2). http://doi.org/10.36633/ulr.566.

[6] Hussainzada, W., Cabrera, J.S., Samim, A.T. et al. Water resource management for improved crop cultivation and productivity with hydraulic engineering solution in arid northern Afghanistan. Appl Water Sci 13, 41 (2023). https://doi.org/10.1007/s13201-022-01850-w.

[7] Thomas, V., & Varzi, M. M. (2015). A legal license for an ecological disaster: the inadequacies of the 1973 Helmand/Hirmand water treaty for sustainable transboundary water resources development. International Journal of Water Resources Development, 31(4), 499-518. https://doi.org/10.1080/07900627.2014.1003346.

[8] Gerlak, A. K., Lautze, J., & Giordano, M. (2011). Water resources data and information exchange in transboundary water treaties. International Environmental Agreements: Politics Law and Economics, 11(2), 179–199. https://doi.org/10.1007/s10784-010-9144-4.

[9] Heggy, E., Sharkawy, Z., & Abotalib, A. Z. (2021). Egypt's water budget deficit and suggested mitigation policies for the Grand Ethiopian Renaissance Dam filling scenarios. Environmental Research Letters, 16(7), 74022. https://doi.org/10.1088/1748-9326/ac0ac9.

[10] Veysi, S., Nouri, M., & Jabbari, A. (2024). Reference evapotranspiration estimation using reanalysis and WaPOR products in dryland Croplands. Heliyon, 10(4). DOI: 10.1016/j.heliyon. 2024.e26531.

[11] Jafarpour, M., Adib, A., & Lotfirad, M. (2022). Improving the accuracy of satellite and reanalysis precipitation data by their ensemble usage. Applied Water Science, 12(9), 232. https://doi.org/10.1007/s13201-022-01750-z.

[12] Thomas, D. C., & Kidd, F. J. (2017). On the margins: enduring pre-modern water management strategies in and around the registan desert, Afghanistan. Journal of Field Archaeology, 42(1), 29-42. https://doi.org/10.1080/00934690.2016.1262188.

[13] Rashki, A., Kaskaoutis, D. G., Francois, P., Kosmopoulos, P. G., & Legrand, M. (2015). Dust-storm dynamics over Sistan region, Iran: Seasonality, transport characteristics and affected areas. Aeolian Research, 16, 35-48. https://doi.org/10.1016/j.aeolia.2014.10.003.

Thermal Monitoring of Sand Dunes using Landsat Time Series: A Case Study of the Rig-e Jen Sand Sea in Central Iran

Erfan Motaghiyan[1] Ata Abdollahi Kakroodi[2], Seyed Kazem Alavipanah[3]
[1]University of Tehran, erfan.motaghiyan@ut.ac.ir
[2]University of Tehran, a.a.kakroodi@ut.ac.ir
[3]University of Tehran, salavipa@ut.ac.ir

Abstract

Long-term thermal monitoring of sand dunes is essential for deciphering arid landscape responses to climate change and surface-atmosphere energy fluxes. However, multi-decadal, spatially explicit analyses of Land Surface Temperature (LST) in sand seas remain scarce. This study bridges this gap by conducting a 35-year spatiotemporal trend analysis of LST for the Rig-e Jen sand Sea in Central Iran. We processed a multi-sensor Landsat time-series (TM, ETM+, OLI/TIRS) from 1989 to 2024, deriving LST using a consistent single-channel algorithm . The annual and seasonal LST trends were rigorously qantified using the non-parametric Mann-Kendall test, complemented by linear regression and analysis of key statistical parameters (e.g., mean, variance, extremes). The results reveal a significant asymmetric thermal pattern between the hottest and coolest dune surfaces. Over the study period, maximum LST shows a weak but statistically significant positive trend ($\tau = 0.068$, $p = 0.0066$; slope = 0.149 °C yr^{-1}), whereas minimum LST exhibits a stronger and more consistent increase ($\tau = 0.207$, $p < 0.0001$; slope = 0.588 °C yr^{-1}). Additional seasonal Mann–Kendall analysis supports persistent surface warming of both extremes, particularly for minimum LST during winter ($\tau = 0.327$; slope = 0.623 °C yr^{-1}) and summer ($\tau = 0.329$; slope = 0.799 °C yr^{-1}), indicating a progressive reduction in intra-dune thermal contrast. These findings point to a systematic upward shift of the dune's thermal baseline, with cooler surfaces warming more rapidly than the hottest surfaces, potentially altering surface energy fluxes and near-surface atmospheric conditions. This study provides the first long-term empirical evidence of thermal change in the Rig-e Jen Desert, establishing a methodological baseline for integrating multi-sensor LST time series in arid climate research. The observed minimum LST trend underscores the sensitivity of hyper-arid dune systems to regional and global climate change.

Keywords: Land Surface Temperature (LST), Landsat Time Series, Remote Sensing, Rig-e Jen, Sand Dunes

1. Introduction

Hyper-arid sand dune ecosystems, such as the Rig-e Jen erg within the Dasht-e Kavir watershed of central Iran, offer critical insights into climate-driven changes in surface thermal regimes and land-atmosphere energy interactions. These systems are particularly suitable for LST analysis due to their minimal vegetation cover and relatively homogeneous surface composition, which simplify emissivity estimation and reduce thermal heterogeneity within satellite pixels. Land Surface Temperature (LST) is a key parameter for characterizing the water and energy balance of the Earth's surface (Zheng et al., 2024). It is recognized as an **Essential Climate Variable (ECV)**. The thermal dynamics of the Earth's surface follow distinct annual and diurnal cycles (Pérez-Planells & Göttsche, 2023). In hyper-arid environments, LST is crucial for modeling hydrological signatures such as soil moisture (Song et al., 2023).

Large sand seas (ergs) are critical indicators of landscape response to climatic shifts (Abbasi et al., 2019). Their extreme remoteness makes *in-situ* monitoring infeasible, establishing satellite-based thermal infrared (TIR) remote sensing as the only viable method for achieving spatially explicit, multi-decadal LST monitoring (Romaguera et al., 2018). The Landsat archive is uniquely positioned to provide the consistent, moderate-resolution time series essential for such climatological analysis (Tahooni et al., 2023).

While LST trends have been studied in various environments, including high-mountain regions (Aguilar-Lome et al., 2019), long-term thermal analysis of major desert sand seas is scarce. The Rig-e Jen, a vast, remote sand sea in the Dasht-e Kavir basin of Central Iran, represents a pristine natural laboratory largely free of anthropogenic modifications (Abbasi et al., 2025).

A key hypothesis in climate change science is the presence of **asymmetric surface warming**, wherein **Minimum temperatures rise faster than Maximum temperatures**, leading to a reduction in the Diurnal Temperature Range (DTR). This study constructs a 35-year (1989–2024) Landsat-based time series of extreme (maximum and minimum) LST for the Rig-e Jen Sand Sea to:

1. Generate a consistent long-term LST record;
2. Quantify temporal trends using non-parametric and regression-based methods; and
3. Evaluate whether surface warming rates differ between extreme maximum and minimum surface temperatures.

2. Study Area

The Rig-e Jen (also spelled Rig-e Jinn) is an extensive and highly remote sand sea situated in the western sector of the Dasht-e Kavir, one of the principal desert basins of central Iran (Fig. 1). The area falls within a hot desert climate (Köppen–Geiger BWh), marked by hyper-arid conditions, extremely low and irregular precipitation, and strong year-round solar radiation. Geomorphologically, Rig-e Jen is an active erg system composed of large barchan, transverse, and topographic dune complexes (Abbasi et al., 2019).

The region’s extreme dryness, negligible vegetation cover, and consistently clear skies—especially during the summer—make it an exceptional natural setting for long-term thermal infrared (TIR) remote sensing. Moreover, its pronounced isolation from urban centers, infrastructure, and agricultural activity ensures that detected thermal patterns primarily reflect regional climatic processes rather than anthropogenic land-use change. This combination of remoteness, atmospheric clarity, and geomorphic uniformity makes Rig-e Jen an ideal case study for multi-decadal LST trend analysis.

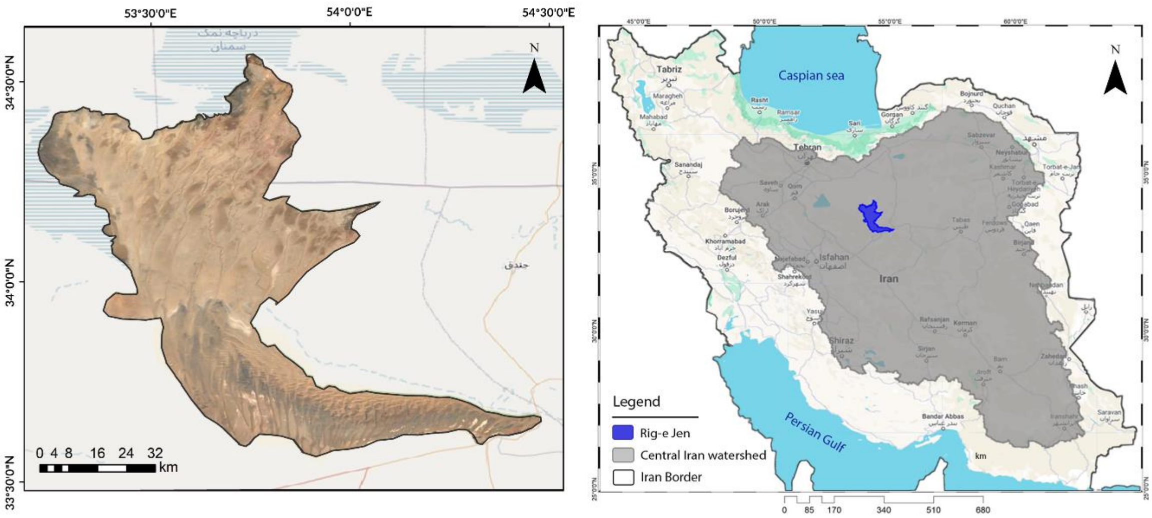

Figure 1. Location and detailed view of the Rig-e Jen sand sea in central Iran. Right side: Overview map showing Iran's national boundary, the Central Iran hydrological basin extent, and the location of the Rig-e Jen dune field over an OpenStreetMap (OSM) basemap. Left side: Close-up of the Rig-e Jen erg with a 2021 Landsat RGB composite overlaid on an OSM basemap.

3. Methodology

This study employed a multi-decadal Landsat LST time series (1989–2024) to examine long-term thermal dynamics in the Rig-e Jen Sand Sea. Surface temperature data were derived from Collection 2 Level-2 products of Landsat 5 TM, Landsat 7 ETM+, Landsat 8 OLI/TIRS, and Landsat 9 OLI/TIRS. All initial preprocessing was performed in Google Earth Engine (GEE), which ensured consistent handling of multi-sensor datasets within a unified computational environment.

Cloud- and shadow-contaminated pixels were excluded using the sensor-specific QA_PIXEL bitmask, and thermal bands were converted to LST using the Collection 2 scaling coefficients. Image collections were filtered to the Rig-e Jen Sand Sea and aggregated at 16-day intervals. For each interval, a median composite was generated to minimize residual cloud contamination and reduce scene-level variability. The resulting mosaics were clipped to the boundary of the Rig-e Jen Sand Sea and exported at 30 m spatial resolution.

To characterize extreme thermal behavior, pixel-level LST values from each composite were ranked, and the three highest (extreme maximum) and three lowest (extreme minimum) values were extracted per scene. This ranking approach minimizes influence of noise and preserves true extreme behavior.

These ranked extremes form the basis of the annual and seasonal extreme-temperature time series used in the subsequent analyses.

Post-processing, temporal aggregation, and statistical evaluation—including trend estimation and visualization—were conducted in Python (NumPy, Pandas, SciPy, Matplotlib) and QGIS. These tools enabled quality control, integration of multi-sensor outputs, and computation of long-term LST trends for the Rig-e Jen Sand Sea.

4. Results and Discussion

4.1 Trends in Extreme Land Surface Temperatures (1989–2024)

Figure 2 presents the 16-day aggregated time series of extreme maximum and minimum LST values across the Rig-e Jen Sand Sea. Table 1 summarizes the corresponding Mann–Kendall (MK) and linear regression statistics. Both metrics show statistically significant long-term surface warming. The extreme maximum LST exhibits a modest but significant upward trend ($\tau = 0.068$; $p = 0.0066$) with a linear slope of 0.149 °C yr^{-1}, though the low R^2 (0.011) reflects strong inter-annual variability.

The extreme minimum LST shows a much stronger and highly significant increase ($\tau = 0.207$; $p < 0.0001$), with a slope of 0.588 °C yr^{-1} and higher explained variance ($R^2 = 0.109$). This indicates that the coldest observed surface conditions in each composite have risen more rapidly and consistently than the hottest conditions.

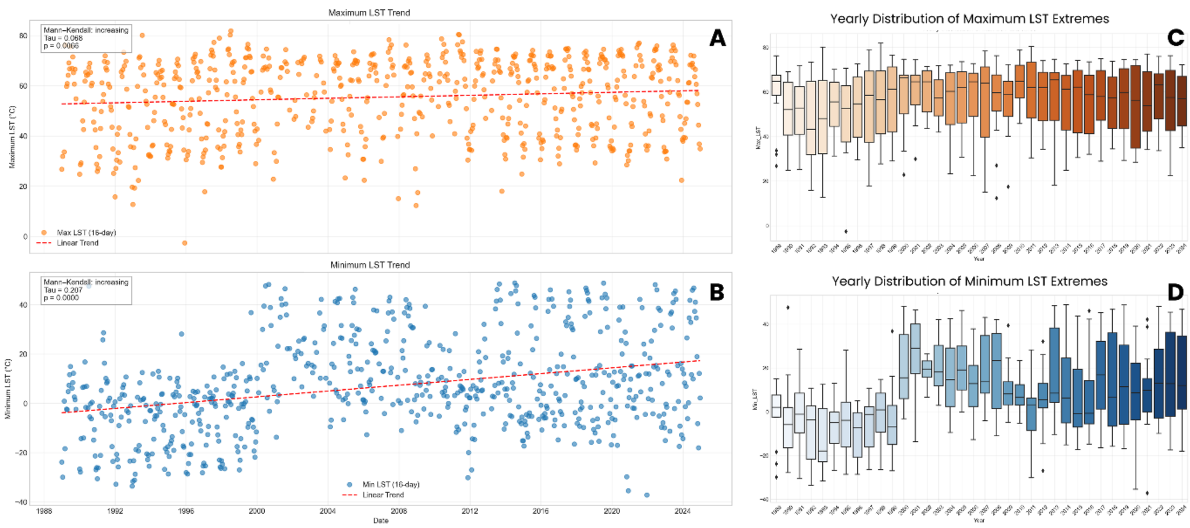

Figure 2. Time series and yearly distributions of extreme Land Surface Temperature (LST) values in the Rig-e Jen Sand Sea from 1989 to 2024. (**A**) Extreme maximum LST (orange points) with linear regression (red dashed line). (**B**) Extreme minimum LST (blue points) with linear regression. (**C**) Yearly boxplot distribution of maximum LST extremes. (**D**) Yearly boxplot distribution of minimum LST extremes.

4.2 Distributional Behavior of Extreme Temperatures

The weaker trend for extreme maximum LST is consistent with large fluctuations caused by episodic heat events, indicating substantial dispersion in the upper envelope of the time series. In contrast, the stronger trend for extreme minimum LST reflects a more coherent upward shift in the lower bound of the temperature distribution over time. Together, these results show that the overall thermal regime of the Rig-e Jen Sand Sea has warmed, with the lower-end extremes increasing more steadily than the upper-end extremes.

Table 1. Mann–Kendall and linear regression statistics for extreme maximum and minimum LST time series (1989–2024) in the Rig-e Jen Sand Sea.

Linear Regression				Mann-Kendall		
Type	Slope (°C/year)	R^2	p-value	Mann-Kendall Trend	Mann-Kendall Tau	Mann-Kendall p
Maximum LST	0.149	0.011	0.006	increasing	0.068	0.006
Minimum LST	0.588	0.109	2.5×10^{-19}	increasing	0.207	2.2×10^{-16}

4.3 Implications for Hyper-Arid Desert Climate Sensitivity

The faster rise in extreme minimum LST suggests that the coldest surface conditions of the sand sea have become less frequent or less intense over the past 35 years. This shift may influence dune surface energy balance, sediment thermal behavior, and broader thermal sensitivity in hyper-arid landscapes. The consistent increase in both extremes highlights the responsiveness of the Rig-e Jen Sand Sea to long-term climatic warming.

5. Conclusion

This study used a 35-year Landsat record to assess extreme LST trends in the Rig-e Jen Sand Sea, revealing significant surface warming in both temperature extremes. Maximum LST increased modestly (0.15 °C yr^{-1}), while minimum LST rose nearly four times faster (0.59 °C yr^{-1}), indicating pronounced asymmetric surface warming.

These findings underscore the value of long-term satellite records for detecting subtle climate signals in remote deserts. Future work could further dissect the seasonal behavior of the extreme LST trends and expand the analysis to other vast sand seas in Central Iran, such as the Lut Desert, to assess the regional consistency of this asymmetric surface warming pattern.

References

Abbasi, H. R., Opp, C., Groll, M., Rohipour, H., & Gohardoust, A. (2019). Assessment of the distribution and activity of dunes in Iran based on mobility indices and ground data. *Aeolian Research*, *41*, Article 100539. https://doi.org/10.1016/j.aeolia.2019.07.005

Aguilar-Lome, J., Espinoza-Villar, R., Espinoza, J. C., Rojas-Acuña, J., Willems, B. L., & Leyva-Molina, W. M. (2019). Elevation-dependent warming of land surface temperatures in the Andes assessed using MODIS LST time series (2000–2017). *International Journal of Applied Earth Observation and Geoinformation*, *77*, 119–128. https://doi.org/10.1016/j.jag.2018.12.013

Pérez-Planells, L., & Göttsche, F.-M. (2023). Combined modelling of annual and diurnal land surface temperature cycles. *Remote Sensing of Environment*, *299*, Article 113892. https://doi.org/10.1016/j.rse.2023.113892

Romaguera, M., Vaughan, R. G., Ettema, J., Izquierdo-Verdiguier, E., Hecker, C. A., & van der Meer, F. D. (2018). Detecting geothermal anomalies and evaluating LST geothermal component by combining thermal remote sensing time series and land surface model data. *Remote Sensing of Environment*, *204*, 534–552. https://doi.org/10.1016/j.rse.2017.10.003

Song, P., Zhao, T., Zhang, Y., & He, Q. (2023). Conversion of satellite passive microwave signals to land surface “skin” temperature for extremely dry deserts. *Remote Sensing of Environment*, *299*, Article 113857. https://doi.org/10.1016/j.rse.2023.113857

Tahooni, A., Kakroodi, A. A., & Kiavarz, M. (2023). Monitoring of land surface albedo and its impact on land surface temperature (LST) using time series of remote sensing data. *Ecological Informatics*, *75*, Article 102118. https://doi.org/10.1016/j.ecoinf.2023.102118

Zheng, X., Guo, Y., Zhou, Z., & Wang, T. (2024). Improvements in land surface temperature and emissivity retrieval from Landsat-9 thermal infrared data. *Remote Sensing of Environment*, *315*, Article 114471. https://doi.org/10.1016/j.rse.2024.114471

Analysis of Spatial Distribution Pattern of Emergency Evacuation Centers in Tehran

Habibollah. Fasihi [1], Zeinab. Tahmasi [2]
[1] Associate Professor, Department of Geography and Urban Planning, Faculty of Geographical Sciences, Kharazmi University, Tehran, Iran, fasihi@khu.ac.ir
[2] Master's student, Department of Geography and Urban Planning, Faculty of Geographical Sciences, Kharazmi University, Tehran, Iran, z.tahmasi2000@gmail.com

Abstract

Emergency evacuation centers are recognized as temporary shelters and safe havens designed to protect citizens during various natural and human-induced hazards. These centers typically include public spaces such as parks, educational buildings, sports halls, or renovated areas, with their primary objective being to reduce population vulnerability to catastrophic events. In this context, Tehran, as the capital and most significant city in Iran, is exposed to various hazards, including earthquakes and floods. Geological predictions indicate a high probability of an earthquake exceeding 7 Richter in Tehran. Furthermore, Tehran's high population density, high building density, the presence of dilapidated structures in some areas, narrow passages that can become blocked during disasters, and traffic problems make emergency response and service delivery extremely challenging during earthquakes and similar hazards. These issues underscore, more than anything else, the necessity of emergency evacuation centers and equitable access for all citizens to these facilities. Therefore, the present study aims to analyze the spatial distribution pattern of emergency evacuation centers in Tehran. The data used in this research were collected from the Tehran Municipality in 2021. Spatial analysis techniques such as standard deviational ellipse, mean center, Moran's spatial autocorrelation, and hotspot analysis employed for data analysis. The research findings indicate that the highest concentration of emergency evacuation centers is in the northern, northwestern, and some central areas of Tehran, while the lowest concentration is in the southern areas of the city. Additionally, the study results reveal an imbalance between the distribution of emergency evacuation centers and the distribution of population density in Tehran.

Keywords: Spatial Pattern, Spatial Distribution, Emergency Evacuation Centers, Tehran City

1. Introduction

Emergency evacuation centers are defined as temporary shelters or safe havens designed to protect urban residents from natural disasters such as floods, earthquakes, storms, or human-induced crises like terrorist attacks. These centers typically comprise public spaces such as parks, educational buildings, sports halls, or renovated facilities, utilized for temporary accommodation, provision of basic medical care, and management of mass evacuations [1]. Within urban planning frameworks, these centers are integral to urban resilience systems, with their primary objective being to mitigate population vulnerability to catastrophic events [2].

Appropriate spatial distribution of these centers is a key factor in achieving comprehensive population coverage and optimizing evacuation [1]. In metropolitan areas, improper distribution can lead to congestion, evacuation delays, and increased vulnerability [3]. In the context of passive defense, the distribution of emergency evacuation centers, based on indicators such as accessibility to military facilities, road width, and building quality, addresses resilience against human crises. At the metropolitan scale, focusing on sub-centers to disperse central density fosters positive interactions between centers [4]. Without proper distribution, disasters such as urban floods, earthquakes, or terrorist attacks will have more devastating effects [5], [6].

Iran, as one of the world's high-risk countries, is exposed to a wide range of natural, human-induced, and complex hazards. According to national assessments, Iran faces over 70 types of hazards annually, including natural disasters like earthquakes, floods, droughts, and landslides, as well as human-induced hazards such as traffic accidents, fires, building collapses, and intentional explosions [7]. Among these, Tehran, as the megacity and capital, has a very high-risk profile, with an earthquake exceeding magnitude 7 highly anticipated. Furthermore, high population density, the presence of non-standard and unsafe buildings, narrow passages, traffic problems, and difficulties in accessibility during hazards [8], [9], more than anything else, highlight the necessity of emergency evacuation centers and equitable access for all citizens to these facilities. For these reasons, the present study analyzes the spatial distribution pattern of emergency evacuation centers within Tehran. The main research question is whether emergency evacuation centers are equitably distributed across Tehran and if their distribution aligns with population density.

2. Materials and Methods

The present study is applied research based on its objective, employing a descriptive-analytical method. Data and information were collected using a library research approach. The data analyzed in this study were gathered from the official website of the Tehran Municipality in 2021. For data analysis, spatial statistical methods such as mean center, standard deviational ellipse, Moran's spatial autocorrelation, and hotspot analysis utilized. For data analysis, first, the overall distribution of emergency evacuation centers across the 22 districts of Tehran Municipality described and analyzed. Subsequently, using spatial analysis methods at the neighborhood level of Tehran, the spatial distribution pattern of emergency evacuation centers was analyzed. The study area in this research encompasses the administrative and political boundaries of Tehran, with an area of over 616 square kilometers and a population of 9,067,826. Administratively, Tehran is divided into 22 districts, 125 sub-districts, and 353 neighborhoods [10].

3. Results

The investigation into the number of emergency evacuation centers in Tehran reveals that, according to 2021 statistics, Tehran possesses a total of 2367 designated centers or spaces for emergency evacuation during hazards such as earthquakes and other potential risks in the city. Tehran is divided into 22 urban districts managed by the Tehran Municipality. Among these districts, District 5 has the highest number of emergency evacuation centers, with 229 centers. It is followed by District 2 with 186 centers and District 1 with 176 centers. Conversely, District 9 has the fewest emergency evacuation centers, with 52 centers. It is followed by District 13 with 59 centers and District 16 with 69 centers. The distribution of emergency evacuation centers across the 22 municipal districts of Tehran is presented in Figure 1.

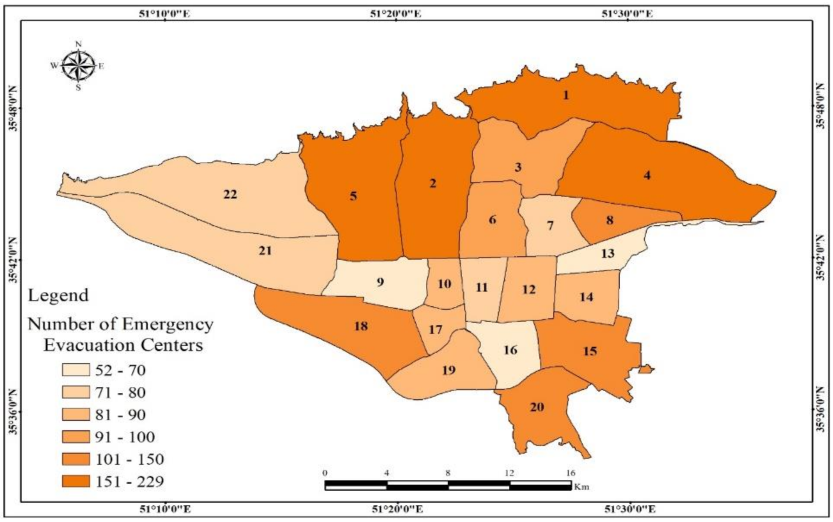

Figure 1. Distribution of emergency evacuation centers across 22 districts of Tehran city

For further examination of the direction and main extent of the spatial distribution of emergency evacuation centers across Tehran, the mean center and directional distribution (standard deviation ellipse) employed. The results indicate that the dispersion of emergency evacuation centers in Tehran has an east-west orientation, and its mean center or central gravity point is located within the southern part of District 6, on the northern border of District 11 of the Tehran Municipality. The directional distribution and mean center of emergency evacuation centers in Tehran are shown in Figure 2.

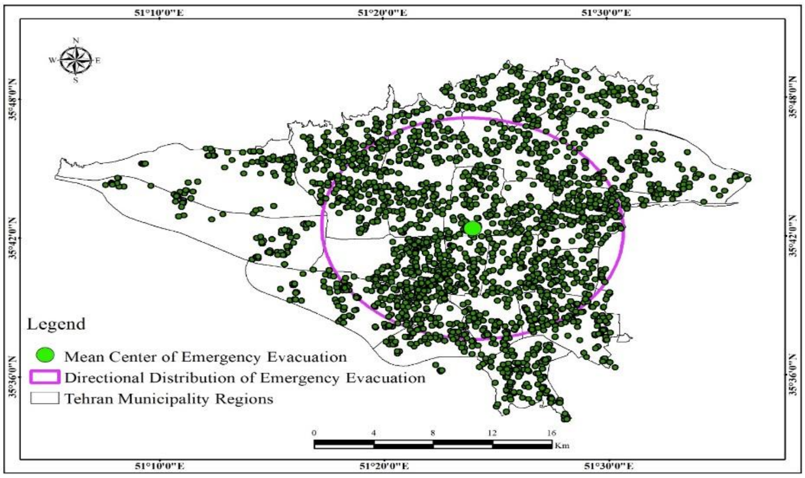

Figure 2. Directional distribution and mean center of emergency evacuation centers

To investigate the presence or absence of a clustered spatial pattern among the data related to emergency evacuation centers in Tehran, spatial autocorrelation (Moran's I) test was used. The output of this index is a value between -1 and +1. When Moran's I is greater than zero and closer to 1, it indicates a clustered pattern in the spatial data. When the output value of Moran's I is less than zero and closer to -1, it indicates a dispersed and non-clustered pattern in the spatial data. When the output value of Moran's I is close to zero, it indicates a random spatial distribution pattern of the data. Furthermore, in the graphical output, clustered, random, and dispersed patterns of the data can generally be distinguished. The results of the spatial autocorrelation test for emergency evacuation centers show that the Moran's I value is 0.50 and the Z-score is 6.77. As indicated in the graphical output, emergency evacuation centers at the neighborhood level in Tehran exhibit a clustered spatial pattern. The results of Moran's spatial autocorrelation are shown in Figure 3 (right).

Hotspot analysis was employed to identify hot and cold clusters, i.e., areas of spatial concentration of high and low values of emergency evacuation centers at the neighborhood level of metropolitan Tehran.

This method examines each feature along with other features located in its vicinity. A single feature alone cannot create a statistically significant hot or cold cluster; for a feature to be considered a significant hot or cold cluster, both the feature itself and its neighboring features must be similar to it to be statistically significant in spatial statistics. In this study, as shown in the map below (Figure 4, left), the blue areas represent the concentration of low values of emergency evacuation centers and are identified as cold clusters. The red areas represent the concentration of high values of emergency evacuation centers and are identified as hot clusters. The results of the hotspot analysis for emergency evacuation centers indicate that a large primary hot cluster has formed in the northern, northwestern, and some central neighborhoods of Tehran. This area is, in fact, the concentration of the highest number of emergency evacuation centers. Additionally, a primary cold cluster has been identified in the southern areas of Tehran, indicating the lowest number of emergency evacuation centers in this area.

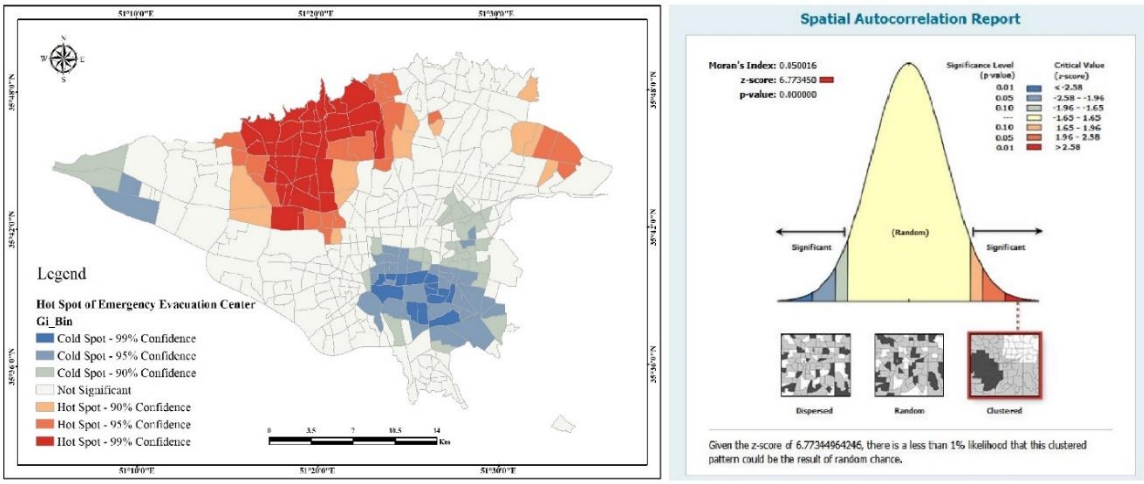

Figure 3. Spatial autocorrelation (right) and hotspot analysis (left) of emergency centers

To align the spatial dispersion and concentration pattern of emergency evacuation centers with the spatial pattern of population density, the distribution of population density at the neighborhood level in Tehran was investigated. For this purpose, the clustered nature of the spatial pattern of population density data was first examined using Moran's spatial autocorrelation. The results of the spatial autocorrelation test for population density at the neighborhood level in Tehran indicate that the Moran's I index value is 0.62 and the Z-score is 27.12. As evident in the graphical output, the spatial distribution of population density at the neighborhood level in Tehran exhibits a clustered spatial pattern. The results of Moran's spatial autocorrelation for population density are shown in Figure 4 (right).

For identifying hot and cold clusters, i.e., areas of spatial concentration of high and low population density values at the neighborhood level in Tehran, hotspot analysis was utilized. As shown in the map below (Figure 4, left), the blue areas represent the concentration of neighborhoods with low population density values and are identified as cold clusters. The red areas represent the concentration of neighborhoods with high population density values and are identified as hot clusters. The results of the hotspot analysis for population density indicate that two hot clusters have formed in the southern and eastern parts of Tehran, which are the concentration points for neighborhoods with the highest population density. Additionally, some cold clusters have been identified in a scattered manner in the northern, western, and southwestern parts of Tehran, representing the concentration points for neighborhoods with the lowest population density in Tehran.

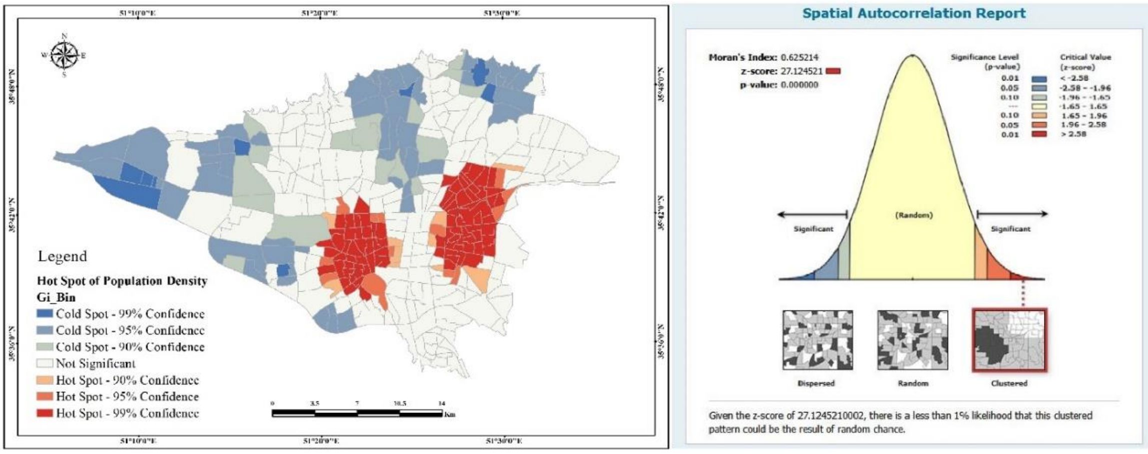

Figure 4. Spatial autocorrelation (right) and hotspot analysis (left) of population density

4. Conclusion

The Based on the findings, Tehran had 2367 emergency evacuation centers in 2021. The highest number of these centers is concentrated in the northern and northwestern parts of the city, particularly in Districts 5, 2, and 1. Conversely, the southern districts, including Districts 9, 13, and 16, have the fewest emergency evacuation centers. The mean center and standard deviation ellipse analysis revealed that the spatial dispersion of emergency evacuation centers in Tehran has a predominant east-west orientation, with its center of gravity located in the southern part of District 6 and the northern border of District 11.

The Moran's I spatial autocorrelation test results further indicate that the spatial distribution of emergency evacuation centers across the city exhibits a significant clustered pattern. Hotspot analysis also revealed the presence of a large hot cluster in the northern, northwestern, and central areas of the city, and a cold cluster in the southern parts of Tehran. In contrast, a similar analysis for population density showed that the highest population density is concentrated in the southern and eastern areas of Tehran. Therefore, it can be concluded that the spatial pattern of emergency evacuation centers does not align with the population density pattern in Tehran, and there is indeed a type of spatial injustice and imbalance in the distribution of safety and relief facilities.

In summary, the research findings indicate that the southern and eastern areas of Tehran, which have the highest population density and consequently the highest vulnerability during crises, are in a less favorable situation regarding access to emergency evacuation centers. This highlights the necessity of reviewing the policies for locating and distributing emergency evacuation centers to achieve spatial justice and enhance urban resilience. Based on the results, it is suggested that future scientific and executive activities consider: reviewing the siting of emergency evacuation centers; employing multi-criteria decision-making models within a GIS environment; paying attention to social vulnerability indicators (income, age, health status, housing quality, and access to urban services); developing multi-purpose and safe urban spaces; continuous monitoring and updating of spatial and demographic data; and simultaneously enhancing public awareness and education.

References

[1] Qiu, J., Tan, H., Yuan, S., Lv, C., Wang, P., Cao, S., & Zhang, Y. (2024). Selection of urban-flood-shelter locations based on risk assessment. *Water-Energy Nexus*, *7*, 151-162.

[2] Jiao, H., & Feng, S. (2024). Towards resilient cities: Optimizing shelter site selection and disaster prevention life circle construction using GIS and supply-demand considerations. *Sustainability*, *16*(6), 2345.

[3] Zuo, J., Shi, J., Li, C., Mu, T., Zeng, Y., & Dong, J. (2021). Simulation and optimization of pedestrian evacuation in high-density urban areas for effectiveness improvement. *Environmental Impact Assessment Review*, *87*, 106521.
[4] Hu, C., Liu, W., Jia, Y., & Jin, Y. (2019). Characterization of territorial spatial agglomeration based on POI data: A case study of Ningbo City, China. *Sustainability*, *11*(18), 5083.
[5] Loucks, D. P. (2015). Debates-Perspectives on socio-hydrology: Simulating hydrologic-human interactions. *Water Resources Research*, *51*(6).
[6] Hamza-Lup, G. L. (2006). *Sensor-based computing techniques for real-time traffic evacuation management*. University of Central Florida.
[7] Soltani, A., Alaedini, F., Shamspour, N., & Ahmadi Marzaleh, M. (2021). Hazard assessment of Iran Provinces based on the Health Ministry Tool in 2019. *Iranian Red Crescent Medical Journal*, *23*(1), e204.
[8] Afsari, R., Nadizadeh Shorabeh, S., Bakhshi Lomer, A. R., Homaee, M., & Arsanjani, J. J. (2023). Using artificial neural networks to assess earthquake vulnerability in urban blocks of Tehran. *Remote Sensing*, *15*(5), 1248.
[9] Shamsipour, A., Jahanshahi, S., Mousavi, S. S., Shoja, F., Golenji, R. A., Tayebi, S., ... & Sharifi, A. (2024). Assessing and mapping urban ecological resilience using the loss-gain approach: A case study of Tehran, Iran. *Sustainable Cities and Society*, *103*, 105252.
[10] Tehran Municipality. (2021). Emergency evacuation centers and population data.

Downscaling Gridded Precipitation to High Resolution over Türkiye's Mediterranean Region Using a Rule-Based Cubist Model

Enes Hisam[1], Elif Sertel[2], Dursun Zafer Seker[2]
[1] Istanbul Technical University, Graduate School, Geomatics Engineering Program, Maslak, 34469 Istanbul, Turkey; khafagy20@itu.edu.tr
[2] Istanbul Technical University, Faculty of Civil Engineering, Geomatics Engineering Department, Maslak, 34469 Istanbul, Turkey (sertele@itu.edu.tr, seker@itu.edu.tr)

Abstract

Accurate and high-resolution precipitation information is critical for climate research, drought monitoring, and water resource management. However, most global gridded precipitation products are limited by their coarse resolution (0.1°–0.25°), reducing their effectiveness in local and regional studies. This work downscales monthly precipitation to 0.04° over the Mediterranean region of Türkiye by combining satellite- and reanalysis-based precipitation products with ground-based observations and land surface characteristics, including elevation, NDVI, land surface temperature, and distance from the sea. A rule-based Cubist model was trained and validated using monthly precipitation records from 193 meteorological stations between 2017 and 2021. Eight precipitation datasets (PERSIANN-CCS, PERSIANN-CDR, PDIR-Now, CHIRPS, GSMaP MVK v7, GSMaP Gauge v7, IMERG v6, ERA5) were employed, both individually and in combination with land surface variables. Independent testing for 2016 demonstrated strong agreement between downscaled maps and observations (PCC > 0.79, RMSE < 39 mm, MAE < 24 mm). The results highlight Cubist's potential for producing high-resolution precipitation datasets to better support regional climate and hydrological applications.

Keywords: Gridded precipitation, Satellite-based precipitation, Reanalysis, Cubist

1. Introduction

Precipitation is a key driver of hydrological and ecological processes and is fundamental for water resources management, drought monitoring, and climate impact assessments. Reliable information on the spatial and temporal variability of rainfall is particularly important in regions where water scarcity, floods, or droughts can cause substantial socio-economic impacts. The Mediterranean region of Türkiye is one of these sensitive areas, with strong topographic gradients, pronounced seasonality, and frequent dry periods linked to increased wildfire risk.

Global satellite-based and reanalysis precipitation products such as PERSIANN, CHIRPS, GSMaP, IMERG, and ERA5 provide continuous coverage over large regions and long time periods, and are widely used in climate and hydrological studies [1-4]. However, their native spatial resolutions typically range from 0.1° to 0.25°, which is often too coarse for local and basin-scale applications, especially in mountainous terrain where precipitation varies strongly over short distances. In such regions, dense rain gauge networks are rarely available, and even when many stations exist, they cannot fully capture fine-scale spatial variability.

Statistical downscaling offers a practical way to bridge the scale gap between coarse gridded products and local information. In this approach, relationships are learned between large-scale precipitation fields and high-resolution auxiliary variables such as topography, land surface temperature (LST), and vegetation indices [5-7]. Among the various machine learning models, the Cubist algorithm is particularly attractive. It builds rule-based regression trees with linear models at the leaves, allowing it to describe nonlinear relationships in a structured and interpretable way. Cubist has been successfully applied in environmental and geospatial applications, including temperature mapping, soil moisture downscaling, evapotranspiration estimation, and precipitation enhancement [8–12].

Existing Cubist-based precipitation studies often rely on a single gridded product, such as TMPA or PERSIANN CDR, and focus on improving that dataset using land surface predictors and gauge data

[9], [11]. In contrast, multi-product approaches that merge several precipitation datasets have been shown to reduce individual product weaknesses and leverage complementary strengths [13], [14]. This is particularly relevant for the Mediterranean region of Türkiye, where a previous evaluation revealed substantial uncertainties among satellite and reanalysis products, especially in complex topography.

In this work, we develop a Cubist-based downscaling framework for the Mediterranean region of Türkiye that:

1. Uses eight satellite-based and reanalysis products as coarse-resolution precipitation inputs.
2. Integrates land surface characteristics (elevation, NDVI, day/night LST, distance from the sea) to capture sub-grid variability.
3. Trains and validates the model using monthly precipitation observations from 193 meteorological stations for 2017–2021, and tests on an independent year (2016).

We focus on producing 0.04° monthly precipitation maps suitable for regional climate and hydrological applications, and we assess the gain obtained by adding land surface predictors to Cubist relative to using gridded precipitation products alone.

2. Materials and Methods

2.1 Study Area

The study area is the Mediterranean region in southern Türkiye, extending along the Mediterranean Sea in the south and the Aegean Sea in the west (Fig. 1 in the journal paper). The region is dominated by complex and rugged topography: the Toros Mountains run roughly west–east parallel to the coastline, while the Amanos range in the east extends north–south. Between mountain ranges and coastline, narrow coastal plains host major agricultural, industrial, and touristic activities.

Annual precipitation varies approximately between 580 and 1300 mm, with most rainfall occurring during winter months and very low rainfall in summer. This strong seasonality, combined with high temperatures, leads to frequent droughts and a high risk of forest fires. The region includes several large hydrological basins and important urban centers such as Antalya, making reliable precipitation information crucial for water management, hazard assessment, and socio-economic planning.

2.2 Precipitation Data

2.2.1 Rain Gauge Stations

Monthly precipitation measurements from 193 rain gauge stations were obtained from the Turkish State Meteorological Service (MGM). These stations are distributed across the region, covering both coastal and inland mountainous areas. The dataset spans January 2016 to September 2021.

For model development, we used:

- Training period: January 2017 – June 2020 (42 months)
- Validation period: July 2020 – September 2021 (15 months)
- Testing period: January 2016 – December 2016 (12 months)

Training and validation sets were used to fit the Cubist model and tune its hyperparameters, while 2016 was kept completely independent to evaluate model generalization and downscaling performance.

2.2.2 Gridded Precipitation Products

We used eight satellite-based and reanalysis products as coarse-resolution precipitation inputs:

- PERSIANN-CCS (0.04°, 1 h latency; satellite only)
- PERSIANN-CDR (0.25°, long-term climate data record)
- PDIR-Now (0.04°, near-real-time)
- CHIRPS (0.05°, gauge-calibrated, long-term)

- GSMaP MVK v7 (0.1°, satellite-based)
- GSMaP Gauge v7 (0.1°, gauge-adjusted)
- IMERG v6 (0.1°, satellite + gauge)
- ERA5 (0.25°, global reanalysis)

These products were aggregated to monthly totals over the Mediterranean region. During training and validation, values at the native resolution of each product were extracted at the rain gauge locations using a point-to-pixel approach, avoiding additional uncertainties from interpolating station data to grids.

For the 2016 test, all gridded products were resampled to a common spatial resolution of 0.04° using bilinear interpolation. The Cubist model predictions were produced on that 0.04° grid, and then evaluated against station measurements for the same year.

2.3 Land Surface Characteristics

To capture local controls on precipitation, we included several land surface variables:

- Elevation: from SRTM DEM (30 m), aggregated to the relevant scales.
- Land surface temperature (LST): monthly daytime and nighttime LST from MODIS MOD11C3 (0.05°), derived using a split-window algorithm.
- NDVI: monthly NDVI from MODIS MOD13A3 (1 km), commonly used to describe vegetation conditions.
- Distance from the sea (DfS): computed in GIS as the distance from each location to the nearest coastline segment.

For the training and validation periods, these variables were extracted directly at station locations. For the 2016 prediction maps, they were prepared on the 0.04° grid (DEM and DfS as static variables; LST and NDVI as monthly variables).

2.4 Cubist Model

Cubist is a rule-based regression algorithm that partitions the predictor space into regions defined by if–then rules and fits a multiple linear regression model in each region. The model therefore combines:

- Decision tree-like splits that capture nonlinear interactions, and
- Local linear relationships that preserve interpretability and extrapolation features.

Cubist can use committees (ensembles of rule sets) and neighbor corrections to improve accuracy. In this study, Cubist models were implemented using standard settings with hyperparameters (e.g., number of committees, minimum cases per rule) tuned through cross-validation on the 2017–2021 dataset.

2.5 Experimental Design

We considered two types of predictor sets for the Cubist model:

1. P-only models:
    - Each gridded precipitation product used individually as the main predictor, or
    - A multi-product combination (Comb1) that stacks the eight products as separate predictors.
2. P + Land models:
    - Same as above, but augmented with elevation, LST (day/night), NDVI, and distance from the sea.

- ✓ **Comb1:** eight precipitation products only.
- ✓ **Comb1_land:** eight precipitation products plus land surface characteristics.

The models were trained on 2017–June 2020, validated on July 2020–September 2021, and then applied to predict monthly precipitation for 2016 on the 0.04° grid. Performance on the independent test year was evaluated at the 193 station locations.

2.6 Evaluation Metrics

We used three standard metrics:

- Pearson correlation coefficient (PCC): measures linear association between observed and predicted monthly precipitation.
- Root mean square error (RMSE, mm): emphasizes larger errors.
- Mean absolute error (MAE, mm): robust average error magnitude.

Metrics were computed at station level for the 12 months of 2016 and then summarised across all stations. As noted in the abstract, all downscaled configurations achieved PCC > 0.79, RMSE < 39 mm, and MAE < 24 mm in the independent test.

3. Results

3.1 Overall Downscaling Performance

Both Comb1 and Comb1_land substantially improved agreement with station data relative to the original coarse products. Table 1 summarises the performance of the Cubist model for these two configurations in 2016.

Table 1. Performance of Cubist for Comb1 and Comb1_land (independent test year 2016).

No	Input	Cubist		
		MAE (mm)	RMSE (mm)	PCC
1	Comb1	**23.63**	**39.86**	**0.79**
2	Comb1_land	**22.89**	**38.40**	**0.81**

The multi-product Cubist model with land surface variables (Comb1_land) provided the best overall performance, reducing MAE and RMSE compared to Comb1 and increasing PCC from 0.79 to 0.81. These values are consistent with the ranges quoted in the abstract and demonstrate that the model can reproduce monthly precipitation variability under a relatively dry year (2016) with good skill.

When individual products were used instead of the multi-product combination (not shown here), the downscaled fields generally outperformed their respective original inputs, but the gains were more modest and varied by product. This supports the idea that combining several datasets leverages complementary strengths and mitigates individual weaknesses.

3.2 Effect of Land Surface Predictors

Comparing Comb1 vs. Comb1_land highlights the contribution of land surface information:

- Elevation strongly improved representation of orographic enhancement along the Toros and Amanos mountain chains.
- Distance from the sea helped to better capture coastal–inland rainfall gradients.
- LST and NDVI provided additional context related to surface energy and vegetation, which in turn affect local precipitation regimes.

The gain in PCC from 0.79 to 0.81, together with the reduction in error metrics, may appear modest numerically but is meaningful considering the complexity of the region and the already reasonable skill of the Comb1 model. Importantly, the spatial structure of precipitation fields is visibly enhanced when land surface variables are included, showing sharper and more realistic gradients.

4. Conclusion

This study presents a Cubist-based statistical downscaling approach to generate 0.04° monthly precipitation estimates over Türkiye's Mediterranean region by merging multiple satellite- and reanalysis-based products with land surface data and gauge observations.

The main findings for the Cubist model are:

- Downscaled products show strong agreement with independent station observations in 2016, with PCC > 0.79, RMSE < 39 mm, and MAE < 24 mm.
- The multi-product combination (Comb1) clearly benefits from incorporating land surface characteristics, with Comb1_land achieving PCC = 0.81, RMSE = 38.4 mm, and MAE = 22.9 mm.
- Land surface variables, particularly elevation, LST, and distance from the sea, play an important role in resolving local precipitation patterns in complex mountainous terrain.

The results confirm that Cubist is a robust tool for precipitation downscaling based on multiple gridded products and auxiliary land surface data. Future work will extend this framework to:

- Evaluate performance across multiple years representing dry, normal, and wet conditions;
- Explore daily or sub-daily downscaling for flood and extreme-event applications;
- Incorporate explainable AI outputs (e.g., SHAP) more systematically to guide variable selection and product combinations.

Overall, the study provides a practical methodology for developing high-resolution precipitation datasets in regions where station density is limited and complex topography challenges traditional interpolation methods.

References

[1] G. J. Huffman et al., "The Global Precipitation Measurement (GPM) mission," *Meteorological Applications*, vol. 18, pp. 334–353, 2011.
[2] C. Funk et al., "The climate hazards infrared precipitation with stations—a new environmental record for monitoring extremes," *Scientific Data*, vol. 2, 2015.
[3] T. Kubota et al., "Global Satellite Mapping of Precipitation (GSMaP) products in the GPM era," in *Satellite Precipitation Measurement*, Adv. Global Change Res., vol. 67, Springer, 2020.
[4] H. Hersbach et al., "The ERA5 global reanalysis," *Q. J. R. Meteorol. Soc.*, vol. 146, pp. 1999–2049, 2020.
[5] X. Chen et al., "Prediction of maize yield at the city level in China using multi-source data," *Remote Sensing*, vol. 13, 2021.
[6] S. Chen et al., "Spatial downscaling methods of soil moisture based on multisource remote sensing data," *Water*, vol. 11, 2019.
[7] C. Chen, Q. He, and Y. Li, "Downscaling and merging multiple satellite precipitation products and gauge observations using random forest," *Journal of Hydrology*, vol. 632, 2024.
[8] T. Appelhans et al., "Evaluating machine learning approaches for interpolation of monthly air temperature at Mt. Kilimanjaro," *Spatial Statistics*, vol. 14, pp. 91–113, 2015.
[9] Z. Ma et al., "A methodological framework to retrospectively obtain downscaled precipitation estimates over the Tibetan Plateau," *Remote Sensing*, vol. 10, 2018.
[10] Z. Ma et al., "Downscaling PERSIANN-CDR over China using Cubist and land surface characteristics," *Remote Sensing*, 2019.
[11] D. Althoff et al., "ETo-Brazil: A daily gridded reference evapotranspiration data set for Brazil," *Water Resources Research*, vol. 56, 2020.
[12] J. T. Walton, "Subpixel urban land cover estimation: Comparing Cubist, random forests, and support vector regression," *Photogramm. Eng. Remote Sens.*, vol. 74, pp. 1213–1222, 2008.
[13] O. M. Baez-Villanueva et al., "RF-MEP: A novel random forest method for merging gridded precipitation products and ground-based measurements," *Remote Sensing of Environment*, vol. 239, 2019.
[14] L. Zhang et al., "Merging multiple satellite-based precipitation products and gauge observations using a double machine learning approach," *Journal of Hydrology*, vol. 594, 2021.

[15] E. Hisam et al., “Comprehensive evaluation of satellite-based and reanalysis precipitation products over the Mediterranean region in Turkey,” *Advances in Space Research*, vol. 71, pp. 3005–3021, 2022.

A Geoinformatics-Driven Conceptual Framework for Dust Hazard Assessment

Masoud Soleimani [a, b], Ali Darvishi Boloorani [a, b, c*], Fatemeh Amiri [a, b], Nastaran Nasiri [b, d], Najmeh Neysani Samany [a, b], Kan Huang [e], Ali Al-Hemoud [f]

[a] Department of Remote Sensing and GIS, Faculty of Geography, University of Tehran, Tehran, Iran

[b] Research Institute for Development of Space Science, Technology, and Applications, University of Tehran, Iran

[c] GeoAI Environmental Engineering Consultancy L.L.C, Abu Dhabi, UAE

[d] Faculty of Civil, Water and Environmental Engineering, Shahid Beheshti University, Tehran, Iran

[e] Center for Atmospheric Chemistry, Department of Environmental Science and Technology, Fudan University, Shanghai, China

[f] Environment and Life Sciences Research Center, Kuwait Institute for Scientific Research, Kuwait City, Kuwait

*Corresponding authors: ali.darvishi@ut.ac.ir

Abstract

This study develops a geoinformatics framework for regional dust hazard assessment by integrating multi-decadal remote sensing (MODIS-AOD) and climatic (TerraClimate) data (2000–2025) in Tehran and neighboring provinces. Six standardized parameters—mean and variability of AOD, precipitation, wind speed, and maximum/minimum temperature—were combined using weighted linear combination. Weights were derived subjectively via AHP and objectively via PCA eigenvalues. Resulting hazard maps, classified into five levels and validated against visually interpreted MODIS dust hotspots, show highest hazards in Qom, Semnan, and Tehran, with PCA-based maps better matching observed hotspots and reducing reliance on expert judgment. Mazandaran exhibits the lowest hazard levels. The PCA-based approach offers a robust, objective tool for regional dust risk assessment and management.

Keywords: Dust storms, Hazard mapping, Geoinformatics, Remote sensing.

1. Introduction

Dust storms are an increasing environmental hazard with significant impacts on public health, economic activities, and social systems (Darvishi Boloorani et al., 2023a). Their frequency and intensity have risen in recent decades due to prolonged droughts, desiccation of inland water bodies, and degradation of wetlands that act as dust-emitting surfaces (Middleton, 2019; Darvishi Boloorani et al., 2024), leading to degraded air quality and increased risks in arid and semi-arid regions (Darvishi Boloorani et al., 2023b). Reliable dust hazard mapping is therefore essential for risk-oriented environmental assessments and disaster risk management (Middleton & Al-Hemoud, 2024). Dust hazard maps support environmental governance by identifying high-risk zones and guiding mitigation strategies (Yang et al., 2015; Darvishi Boloorani et al., 2021). Most studies rely on Multi-Criteria Decision-Making (MCDM) methods, particularly the Analytic Hierarchy Process (AHP), which depend on subjective expert judgment and parameter weighting (Darvishi Boloorani et al., 2023c; Wang et al., 2024). To overcome these limitations, this study applies Principal Component Analysis (PCA) to derive objective, data-driven weights directly from environmental variables, offering a statistically robust and operationally simple alternative (Rahman et al., 2015; Basu et al., 2022). The study focuses on Tehran and surrounding provinces, where dust exposure has increased in recent years. Long-term remote sensing and climatic data, including Aerosol Optical Depth (AOD), precipitation, wind speed, and temperature extremes, are integrated to generate a reliable and bias-free dust hazard map using PCA (Karami et al., 2017; Vukovic Vimic et al., 2021).

2. Materials and Methods

This study applied a multi-stage workflow including data acquisition, preprocessing, parameter standardization using min–max normalization, weight derivation using AHP and PCA, computation of a Hazard Composite Index (HCI), classification using the natural-breaks method, and validation against ground-truth data. The workflow is illustrated in Fig. 1.

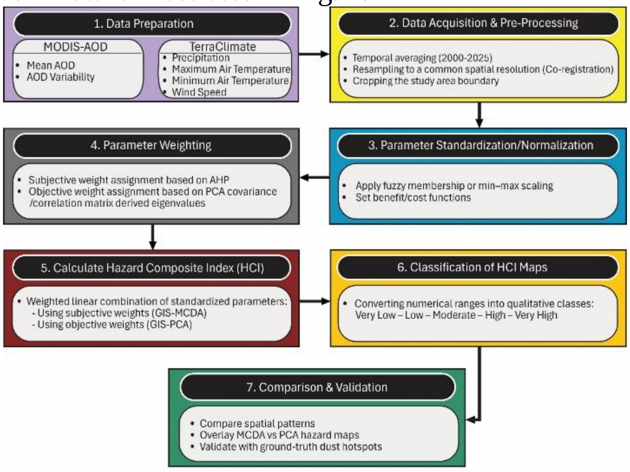

Figure 3. Conceptual workflow of the study for dust hazard mapping, illustrating the main stages from data acquisition and preprocessing, through parameter standardization, weighting (AHP and PCA), hazard composite index computation, classification, and validation.

2.1. Study Area

The study covers Tehran Province and parts of six neighboring provinces (Alborz, Qazvin, Qom, Semnan, Mazandaran, and Markazi) (Fig. 2), reflecting the transboundary nature of dust storms. Tehran hosts over 16.6% of Iran's population on ~0.8% of the land, with socio-economic and administrative significance. The region shows high climatic heterogeneity, from semi-arid Tehran (~230 mm annual precipitation) to humid Mazandaran (800–1000 mm), and arid southern/eastern provinces with extensive dust sources.

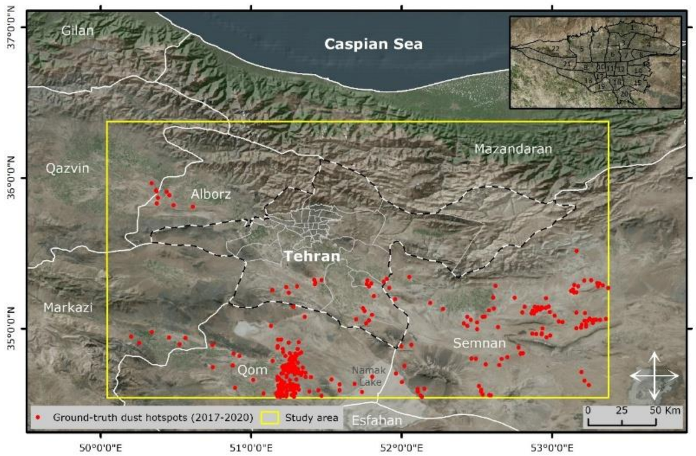

Figure 4. Study area showing Tehran Province and the six neighboring provinces included in the analysis, highlighting key geographic and climatic features relevant to regional dust hazard assessment.

2.2. Data and Pre-Processing

Remote sensing datasets were used due to limited observational stations. AOD from MODIS-Terra/Aqua (2000–2025) represented long-term dust conditions (Rashki et al., 2021; Papi et al., 2022), with variance/mean capturing temporal variability. Additional variables—precipitation, maximum/minimum temperature, and wind speed—were obtained from TerraClimate (2000–2024) (Abatzoglou et al., 2018). Data were processed in Google Earth Engine, resampled to 1-km resolution, clipped to the study area, and validated against 2017–2020 dust hotspots, which were generated through visual interpretation of satellite images from sub-daily MODIS imagery (Darvishi Boloorani et al., 2023d) (Fig. 2).

To prepare the parameters for the subsequent weighting analyses, all variables were normalized to a 0–1 scale according to their influence on dust hazard, ensuring higher values consistently indicate greater hazard potential, using max-based (Eq. 1) scaling for positively related parameters and min-based (Eq. 2) scaling for negatively related ones.

$$x_{Normalized} = \frac{x - x_{min}}{x_{max} - x_{min}} \quad \text{Eq. (1)}$$

$$x_{Normalized} = \frac{x_{max} - x}{x_{max} - x_{min}} \quad \text{Eq. (2)}$$

where x is the original value of the input parameter, and x_{min} and x_{max} represent the minimum and maximum values of that parameter, respectively.

2.3. Weighting Approaches

Weights for six dust-related parameters were derived using AHP (Saaty, 1980), based on expert pairwise comparisons, and PCA, based on data variance. AHP captures subjective expert judgment, aggregated from 20 specialists, while PCA objectively assigns weights from principal components explaining dataset variance. Comparing AHP- and PCA-based weights enables evaluation of both expert knowledge and data-driven contributions for the HCI.

2.4. Hazard Composite Index (HCI)

2.4.1. MCDM-based HCI

At this stage, the dust hazard was mapped by computing a weighted linear combination (WLC) of the standardized parameters to produce the dust HCI. The dust hazard index based on the MCDM (AHP) approach was calculated using Eq. 3:

$$HCI_{MCDM} = \sum_{i=1}^{6} w_i \, . \, x_i \quad \text{Eq. (3)}$$

where w_i is the weight of each parameter derived from the AHP model, and x_i is the corresponding standardized input parameter.

2.4.2. PCA-based HCI

For the PCA-based HCI, a similar WLC approach was applied. The key difference is that, instead of the original input parameters, the retained principal components were used, and their corresponding eigenvalues served as weights (Eq. 4):

$$HCI_{PCA}(x) = \sum_{i=1}^{n} \left(\frac{\lambda_i}{\sum_{k=1}^{n} \lambda_k}\right) PC_i(x) \quad \text{Eq. (4)}$$

where λ_i is the eigenvalue of principal component i, and $PC_i(x)$ is the normalized score of principal component i at location x. According to this formulation, a higher λ_i indicates a greater contribution of the corresponding component–and its associated parameters–to the overall dust HCI.

2.4.3. Classification

In this step, the dust HCIs derived from both the MCDM and PCA approaches were classified into five categories: Very Low, Low, Moderate, High, and Very High. Classification was performed using the Natural Breaks (Jenks) method in ArcMap, which minimizes within-class variance while maximizing between-class variance. This method is particularly suitable for datasets with non-uniform or skewed distributions, such as hazard indices. The resulting class boundaries were then used to generate the final HCI classification maps.

2.5. Comparison and validation

Hazard is not directly measurable, making validation of dust HCI maps challenging. To evaluate map performance, 296 dust hotspots from 2017–2020 were identified through visual interpretation of MODIS Terra/Aqua true-color images (RGB_{143}) (Darvishi Boloorani et al., 2023d) and used as independent validation data (Fig. 2). For each HCI map—derived from either MCDM- or PCA-based weighting—the number of hotspots falling within High and Very High hazard classes was quantified. These dust hotspots represent locations where observed dust emissions interact with environmental factors such as wind, precipitation, and temperature, providing a relative measure of the accuracy of the generated hazard maps (Al-Hemoud et al., 2024).

3. Results and Discussion

3.1. Spatial distribution of input parameters

Spatial patterns of mean AOD, AOD variability, precipitation, wind speed, and temperatures are shown in Fig. 3. Highest mean AOD and variability occur in Qom, Semnan, and southern Tehran, aligning with known dust hotspots, while Mazandaran shows Very Low values due to humid climate and vegetation. Precipitation is highest in northern Alborz and Mazandaran, but low in Semnan, Qom, and southeast Tehran, promoting dust potential. Wind speeds are elevated in Tehran, Qom, and Qazvin, and temperature patterns follow elevation gradients, with moderate conditions in Tehran.

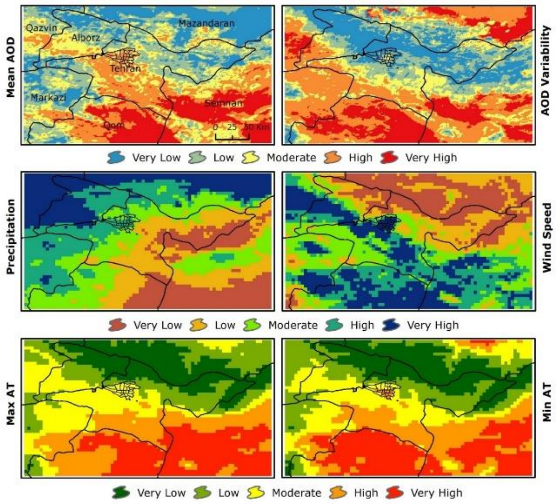

Figure 5. Spatial distribution of input parameters in study area.

3.2. MCDM-based Weighting

The AHP-based MCDM approach was applied to derive weights for six dust-related parameters. The aggregated expert judgments (CR < 0.1) indicate logical consistency. Mean MODIS-AOD (0.36) and mean wind speed (0.30) are the dominant contributors, accounting for 66% of the total weight, reflecting their primary role in dust occurrence and intensity (Table 1). AOD variability has a moderate influence (0.14), while mean precipitation plays a minor mitigating role (0.10). Mean maximum and minimum temperatures are least influential (0.05 each). Overall, AHP highlights that dust hazard is mainly driven by dust load and wind, with other climatic factors as secondary contributors.

Table 1. Weights obtained through pairwise comparison of criteria based on the AHP method.

Criteria	Weight
AOD	0.36
AOD variability	0.14
Precipitation	0.10
Wind speed	0.30
Maximum air temperature (T_{Max})	0.05
Minimum air temperature (T_{Min})	0.05
Total	1.00

3.3. PCA-based Weighting

The PCA-based weighting extracted orthogonal components capturing dominant variability patterns among six dust-related parameters. PC-1, PC-2, and PC-3 explain most of the variance (3.6, 1.7, 0.5; 36%, 14%, 10%) (Table 2), while PC-4 to PC-6 contribute minimally. Spatial patterns of the PCA components (Fig. 4) reveal latent structures, including a pronounced north–south gradient in PC-1 and localized contrasts highlighted by PC-2 and PC-3, which are not evident from individual parameter maps. Normalized eigenvalues serve as objective weights, with PC-1 (0.36) and PC-2 (0.14) having the highest influence, providing a data-driven alternative to subjective AHP weighting. PCA-derived hazard patterns align closely with observed dust hotspots in Tehran, Qom, Semnan, and parts of southern Alborz and Markazi, improving spatial coherence and capturing combined parameter effects. Overall, PCA enhances detection of underlying environmental gradients, reduces reliance on expert judgment, and offers a robust framework complementary to AHP for dust hazard assessment.

Table 2. Calculated eigenvalues for different components based on the PCA-correlation matrix.

Component	Eigenvalue	Normalized eigenvalue
PC-1	3.6	0.36
PC-2	1.7	0.14
PC-3	0.5	0.10
PC-4	0.2	0.30
PC-5	0.2	0.05
PC-6	0.1	0.05
Total	6.3	1.00

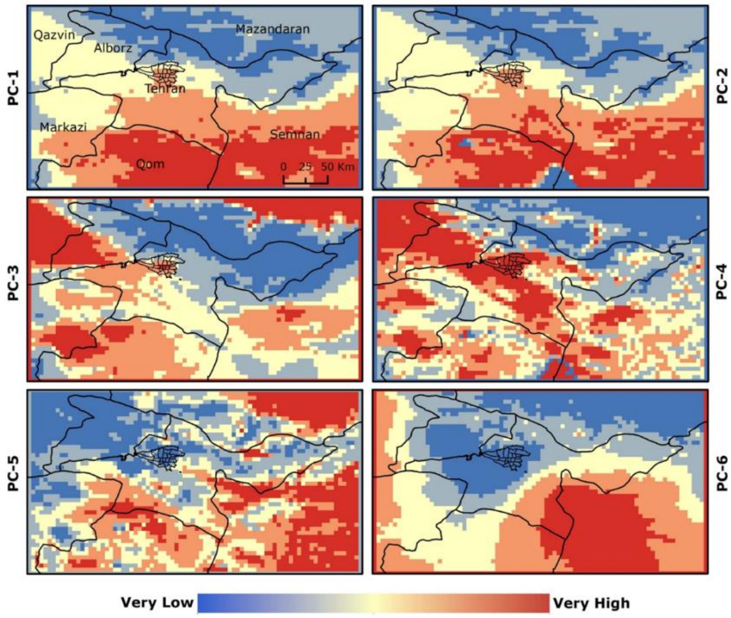

Figure 4. Principal components derived from the orthogonal combination of input dust hazard parameters.

3.4. Dust Hazard Composite Index Maps

Dust HCI maps from MCDM- and PCA-based weighting, classified into five hazard levels, are shown in Fig. 5. Both maps align in Very Low and Low classes, but differ in Moderate to Very High categories. HCI-MCDM captured 92.56% of dust hotspots in High and Very High classes, while HCI-PCA captured 96.28%, showing slightly superior performance for the PCA-based approach.

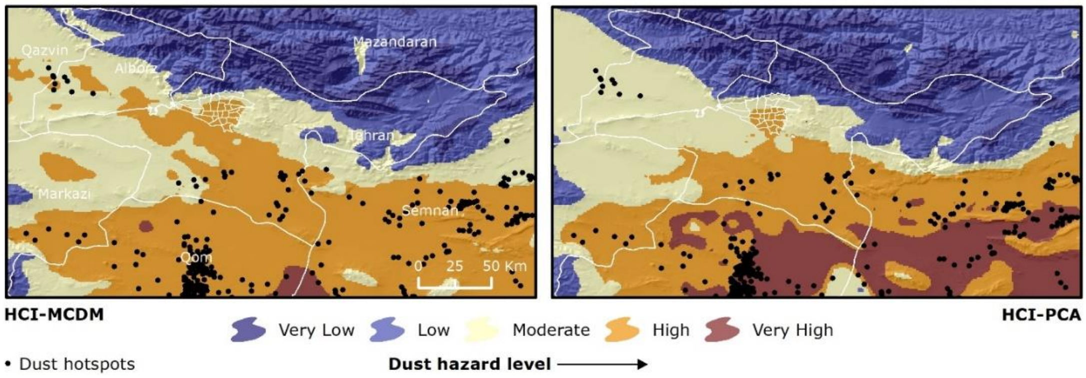

Figure 5. Spatial distribution of the dust Hazard Composite Index (HCI) maps for the study area, classified into five classes (Very Low to Very High), generated using MCDM-based weighting and PCA-based weighting approaches.

3.5. Evaluation of the provincial distribution of dust hazard levels

Fig. 6 shows the proportion of each province in five dust hazard classes based on HCI-MCDM (Fig. 6a) and HCI-PCA (Fig. 6b). Both approaches identify Qom (~85%) and Semnan (>45%) as the most affected regions, but HCI-MCDM underestimates Very High hazard areas compared to HCI-PCA (Qom: 3% vs. >30%; Semnan: 2% vs. >50%). Mazandaran remains dominated by Low and Very Low hazards due to its humid climate and dense vegetation. Tehran shows ~44% High and Very High hazard, with 39% (under HCI-MCDM)–44% (under HCI-PCA) in Moderate class, indicating a transitional regime influenced by population density. Qazvin and Markazi are mainly Moderate, while Alborz shows slight overestimation by HCI-MCDM (~4% High). Overall, PCA-based weighting captures larger, more realistic hazard extents, particularly in major dust source areas, highlighting its superior sensitivity and suitability for regional dust risk assessment and management.

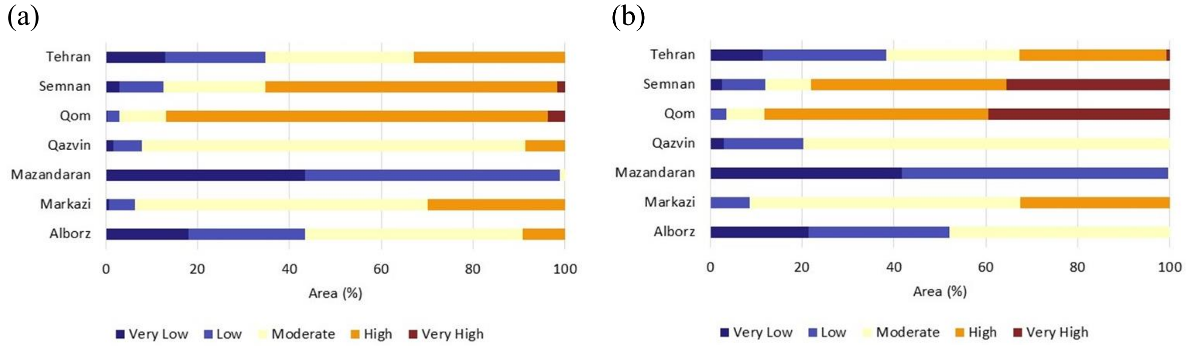

Figure 6. Provincial share (%) of dust hazard classes in the study area boundary: a) HCI-MCDM, b) HCI-PCA.

4. Conclusion

The study shows that PCA-based objective weighting outperforms AHP-based MCDM in capturing spatial dust hazard patterns across Tehran and neighboring provinces. Validation against visually interpreted dust hotspots confirms higher accuracy and reduced uncertainty with PCA. The resulting dust hazard maps provide a practical framework for identifying high-hazard zones and support decision-making in risk management, land-use planning, environmental protection, and public health, particularly in Tehran, Qom, and Semnan. Spatial analysis highlights a concentration of High and Very High hazards in the arid provinces of Semnan and Qom, which act as persistent dust sources affecting surrounding regions. In contrast, Mazandaran exhibits predominantly Low/Very Low hazard due to its humid climate and dense vegetation. These findings emphasize spatial inequalities in dust vulnerability and underscore the need for targeted governance, land management, surface stabilization, and regional cooperation in dust mitigation policies.

References

Abatzoglou, J. T., Dobrowski, S. Z., Parks, S. A., & Hegewisch, K. C. (2018). TerraClimate, a high-resolution global dataset of monthly climate and climatic water balance from 1958–2015. Scientific data, 5(1), 1-12.

Al-Hemoud, A., Naghibi, A., Hashemi, H., Petrov, P., Kamal, H., Al-Senafi, A., ... & Darvishi Boloorani, A. (2024). Dust source susceptibility in the lower Mesopotamian floodplain of Iraq. Remote Sensing Applications: Society and Environment, 36, 101355.

Basu, T., Das, A., & Pal, S. (2022). Application of geographically weighted principal component analysis and fuzzy approach for unsupervised landslide susceptibility mapping on Gish River Basin, India. Geocarto International, 37(5), 1294-1317.

Darvishi Boloorani, A., Nasiri, N., Soleimani, M., Papi, R., Neysani Samany, N., Amiri, F., & Al-Hemoud, A. (2024). Climate Change, Dust Storms, and Air Pollution in the MENA Region. In Climate Change and Environmental Degradation in the MENA Region (pp. 327-343). Cham: Springer Nature Switzerland.

Darvishi Boloorani, A., Papi, R., Soleimani, M., Al-Hemoud, A., Amiri, F., Karami, L., ... & Mirzaei, S. (2023d). Visual interpretation of satellite imagery for hotspot dust sources identification. Remote Sensing Applications: Society and Environment, 29, 100888.

Darvishi Boloorani, A., Shorabeh, S. N., Samany, N. N., Mousivand, A., Kazemi, Y., Jaafarzadeh, N., ... & Rabiei, J. (2021). Vulnerability mapping and risk analysis of sand and dust storms in Ahvaz, IRAN. Environmental Pollution, 279, 116859.

Darvishi Boloorani, A., Soleimani, M., Neysani Samany, N., Bakhtiari, M., Qareqani, M., Papi, R., & Mirzaei, S. (2023c). Assessment of rural vulnerability to sand and dust storms in Iran. Atmosphere, 14(2), 281.

Darvishi Boloorani, A., Soleimani, M., Papi, R., Neysani Samany, N., Teymouri, P., & Soleimani, Z. (2023a). Sources, drivers, and impacts of sand and dust storms: a global view. In Dust and health: Challenges and solutions (pp. 31-49). Cham: Springer International Publishing.

Darvishi Boloorani, A., Soleimani, Z., Teymouri, P., Neysani Samany, N., Soleimani, M., & Papi, R. (2023b). Microbiology of sand and dust storms and the effects on human health in Iran and other Persian Gulf countries. In Dust and health: challenges and solutions (pp. 157-186). Cham: Springer International Publishing.

Karami, S., Ranjbar, A., Mohebalhojeh, A. R., & Moradi, M. (2017). A rare case of haboob in Tehran: observational and numerical study. Atmospheric Research, 185, 169-185.

Middleton, N. (2019). Variability and trends in dust storm frequency on decadal timescales: Climatic drivers and human impacts. Geosciences, 9(6), 261.

Middleton, N., & Al-Hemoud, A. (2024). Sand and dust storms: recent developments in impact mitigation. Sustainability, 16(16), 7121.

Papi, R., Kakroodi, A. A., Soleimani, M., Karami, L., Amiri, F., & Alavipanah, S. K. (2022). Identifying sand and dust storm sources using spatial-temporal analysis of remote sensing data in Central Iran. Ecological Informatics, 70, 101724.

Rahman, M. R., Shi, Z. H., Chongfa, C., & Dun, Z. (2015). Assessing soil erosion hazard-a raster based GIS approach with spatial principal component analysis (SPCA). Earth Science Informatics, 8(4), 853-865.

Rashki, A., Middleton, N. J., & Goudie, A. S. (2021). Dust storms in Iran–Distribution, causes, frequencies and impacts. Aeolian Research, 48, 100655.

Saaty, T. L. (1980). The analytical hierarchy process, planning, priority. Resource allocation. RWS publications, USA.

Vukovic Vimic, A., Cvetkovic, B., Giannaros, T. M., Shahbazi, R., Sehat Kashani, S., Prieto, J., ... & Terradellas, E. (2021). Numerical simulation of Tehran dust storm on 2 June 2014: A case study of agricultural abandoned lands as emission sources. Atmosphere, 12(8), 1054.

Wang, W., He, S., Guo, H., Abuduwaili, J., Samat, A., De Maeyer, P., & Van de Voorde, T. (2024). Sand and dust storm risk assessment in arid central Asia: implications for the environment, society, and agriculture. International Journal of Disaster Risk Science, 15(5), 703-718.

Yang, H., Zhang, X., Zhao, F., Wang, J. A., Shi, P., & Liu, L. (2015). Mapping sand-dust storm risk of the world. In World atlas of natural disaster risk (pp. 115-150). Berlin, Heidelberg: Springer Berlin Heidelberg.

GIS-Based Spatial and Seasonal Analysis of Air Pollution–Related Diseases in Ahvaz, Northern Persian Gulf

Rahimeh Rostami[6], Najmeh Neisani Samani[7]*, Meysam Argani[8] , Ali Darvishi Boloorani[9], Neamatollah Jaafarzadeh Haghighi Fard[10]

[1] Department of Remote Sensing and GIS, Faculty of Geography, University of Tehran, Tehran, Iran, Rahimeh.rostami@ut.ac.ir

[2] Department of Remote Sensing and GIS, Faculty of Geography, University of Tehran, Tehran, Iran, nneysani@ut.ac.ir

[3] Department of Remote Sensing and GIS, Faculty of Geography, University of Tehran, Tehran, Iran

[4] Department of Remote Sensing and GIS, Faculty of Geography, University of Tehran, Tehran, Iran

[5] Environmental Technologies Research Center, Medical Basic Sciences Research Institute, Ahvaz Jundishapur University of Medical Sciences, Ahvaz, Iran Jaafarzadeh-n@ajums.ac.ir n.jaafarzad@gmail.com

Abstract

This study examines the spatiotemporal dynamics of eye, skin, respiratory, cardiovascular, and cancer diseases in Ahvaz, Iran, over the period 2015–2019 by integrating Geographic Information System (GIS)-based spatial analysis with time-series data evaluation. Patient records obtained from municipal healthcare centers were standardized per 10,000 residents in each district to ensure comparability across space and time. Spatial patterns of disease incidence were analyzed using Kernel Density Estimation (KDE) and the Getis–Ord Gi* hotspot technique to delineate statistically significant clusters and seasonal variations in health outcomes. The findings indicate that respiratory and eye diseases exhibit higher spatial densities during warmer months, whereas cardiovascular disorders are more prevalent during colder periods. Skin-related diseases demonstrate inconsistent seasonal trends, while cancer occurrences remain relatively stable throughout the study years. Statistically significant hotspots (95–99% confidence level) were primarily concentrated in the central and eastern zones of Ahvaz. The study underscores the value of GIS-based spatial analytics as a decision-support tool for identifying vulnerable urban areas and formulating evidence-driven public health interventions.

Keywords: Geographic Information System (GIS); Hotspot analysis; Air pollution; Ahvaz; Seasonal analysis

1. Introduction

In recent decades, rapid urbanization and severe air pollution in Iranian megacities—particularly Ahvaz, one of the most polluted cities nationally and globally—have posed major public health challenges. Airborne particulate matter in Ahvaz frequently exceeds international standards [3,4], contributing to higher rates of chronic diseases such as respiratory, cardiovascular, and ocular disorders. While previous studies have highlighted the impact of environmental pollution and climate on disease distribution [2,4], few have simultaneously analyzed multiple disease categories at the urban scale across all seasons using advanced spatial methods.

This study conducts a seasonal and spatial assessment of five disease groups—ocular, dermatological, respiratory, cardiovascular, and cancer—in Ahvaz. By combining GIS and Python-based analyses, it aims to identify disease patterns, health hotspots, and their relationships with environmental factors.

2. Study Area and Data

Ahvaz, the capital city of Khuzestan Province, encompasses an area of about 250 km² and is characterized by a hot and arid climate. It records some of the highest average concentrations of particulate matter pollution nationwide [3,4]. Major contributors to the city's poor air quality include emissions from oil refineries, steel manufacturing plants, heavy urban traffic, and frequent dust storms originating from surrounding deserts. The geographic extent of the study area is depicted in Figure 1.

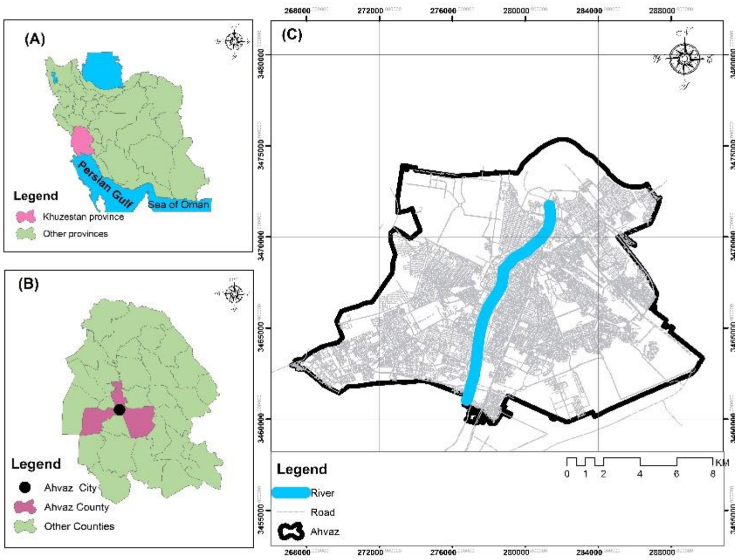

Figure 6 Study area

Disease-related information was collected from municipal health centers covering a five-year period between 2015 and 2019 (corresponding to 1394–1398 in the Iranian calendar). The dataset comprises the number of reported cases, classified by disease category and by temporal variables such as month and season. The geographic coordinates of each health center were transformed into the Universal Transverse Mercator (UTM) coordinate system (EPSG:32639). Subsequently, disease incidence rates were standardized per 10,000 inhabitants based on the population of the respective administrative districts.

3. Research Methodology

The analytical framework of this study consisted of two primary components:

1. **Temporal Analysis:**
   Monthly variations in disease incidence were examined using Python-based data visualization tools. Time-series plots were generated to identify temporal fluctuations and seasonal trends across the different disease categories. These charts provided insights into recurring seasonal patterns for most of the examined conditions.

2. **Spatial Analysis:**
   Spatial patterns of disease occurrence were investigated annually and seasonally within a Geographic Information System (GIS) environment. Initially, Kernel Density Estimation (KDE) was applied to illustrate the overall spatial distribution of patient density. Subsequently, the Getis–Ord Gi* spatial statistic [1] was employed to detect statistically significant clusters of high (hotspots) and low (cold spots) disease incidence at confidence levels of 90%, 95%, and 99%.

This combined approach enabled the identification of spatially non-random clusters of disease distribution. Separate thematic maps were generated for each year and season to visualize and interpret the evolving spatial and temporal dynamics of health outcomes.

4. Results and Discussion

4.1Temporal Analysis

The time-series analysis (Figure 2) revealed that the central districts of Ahvaz recorded the highest number of patients, reaching approximately 3,500 cases annually. A general upward trend in overall disease incidence was observed throughout the study period from 2015 to 2019 (1394–1398). Among the examined disease categories, respiratory illnesses displayed the most pronounced temporal variability, with several peaks occurring during the winter and spring months. In contrast, ocular diseases exhibited their maximum rise during the summer season. Cardiovascular diseases showed the highest incidence in colder months, indicating a potential association between lower temperatures and the aggravation of cardiac-related symptoms.

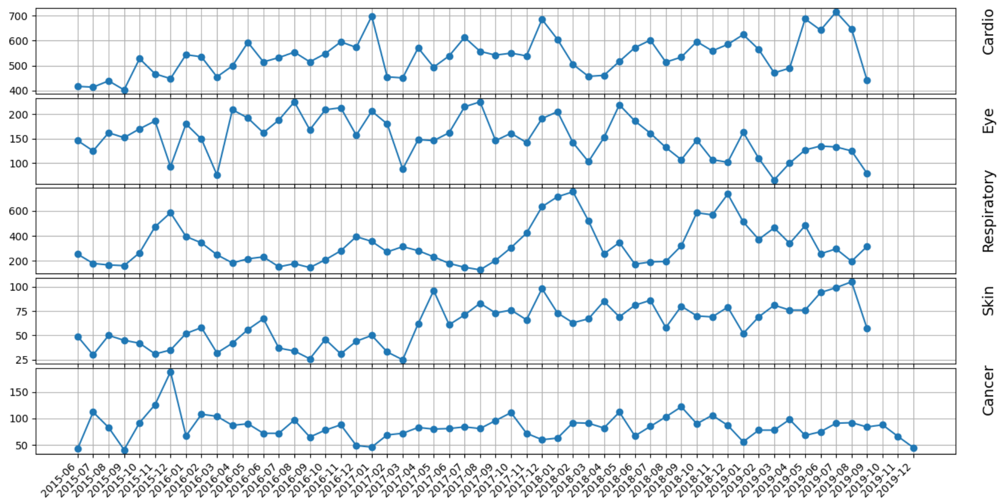

Figure 7 Time series trends and frequency distribution of diseases across different blocks of Ahvaz (2015–2019 / 1394–1398)

4.2 Spatial Analysis

The spatial analysis indicated that the highest concentrations of disease were predominantly located in the central and eastern districts of Ahvaz. Statistically significant hotspots at the 99% confidence level were consistently identified in these areas across all seasons and years (Figure 3).

- **Cardiovascular diseases:** Hotspots remained stable during the colder months, with high levels of statistical confidence.
- **Respiratory diseases:** Displayed the broadest spatial distribution, with hotspots primarily concentrated in industrial sectors.
- **Ocular diseases:** Showed persistent clustering in central urban areas throughout the year.
- **Dermatological diseases:** Exhibited seasonal variability in spatial distribution, reflecting fluctuating patterns across different times of the year.

Conversely, the northern and peripheral districts generally corresponded to cold spots, indicating areas of lower disease prevalence relative to the rest of the city.

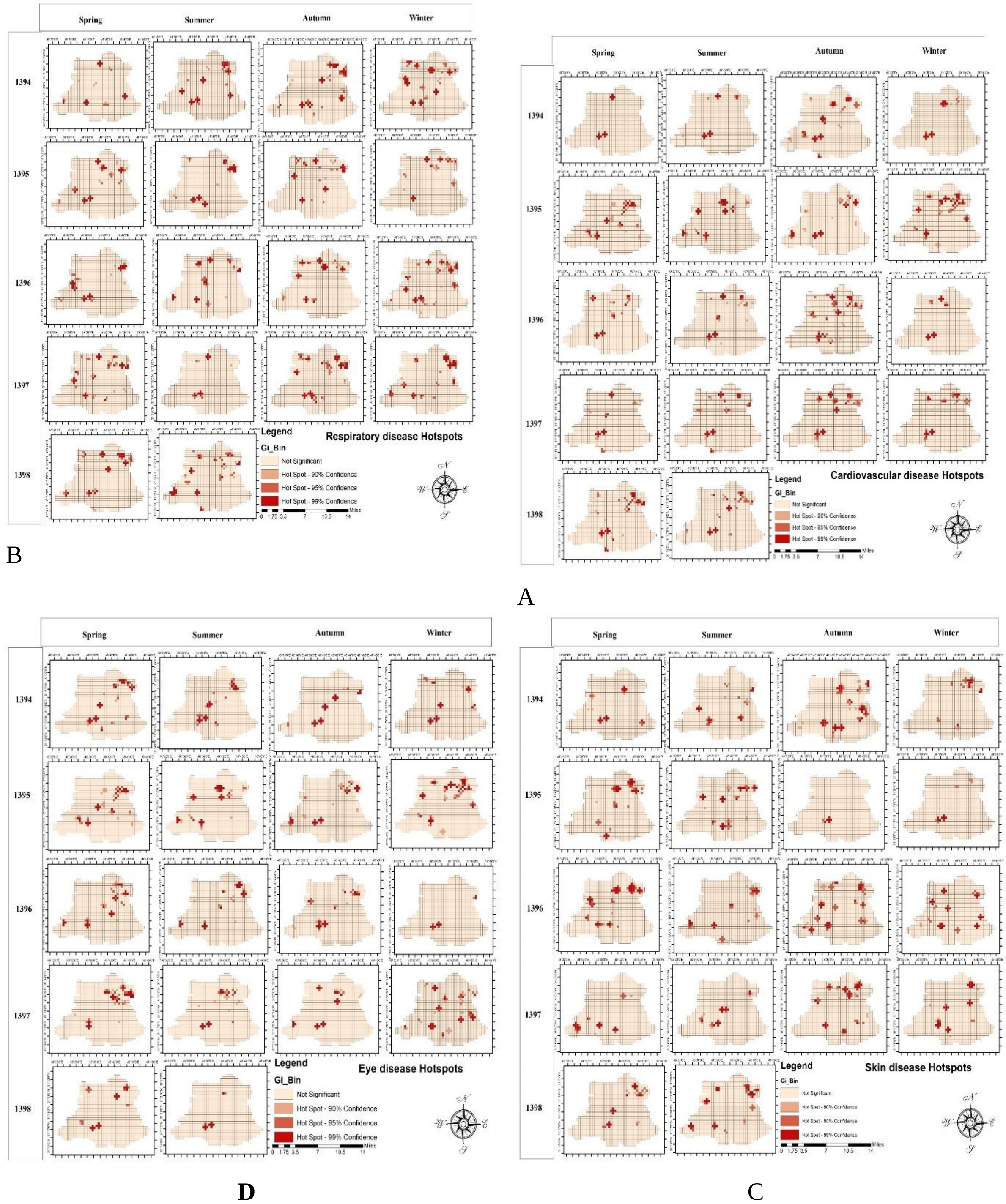

Figure 8: Seasonal hotspot maps of diseases in Ahvaz
(a) Cardiovascular diseases (b) Respiratory diseases (c) Ocular diseases (d) Dermatological diseases

4.3 Cancer Distribution

The spatial assessment of cancer cases identified consistently stable hotspots throughout all seasons (Figure 4). Additionally, frequency analysis of different cancer types revealed notable disparities in prevalence: certain cancer categories, with over 800 reported cases, occurred significantly more frequently than others, which had fewer than 200 cases (Figure 5). This uneven distribution underscores the importance of examining specific risk factors associated with the more prevalent cancer types in the region.

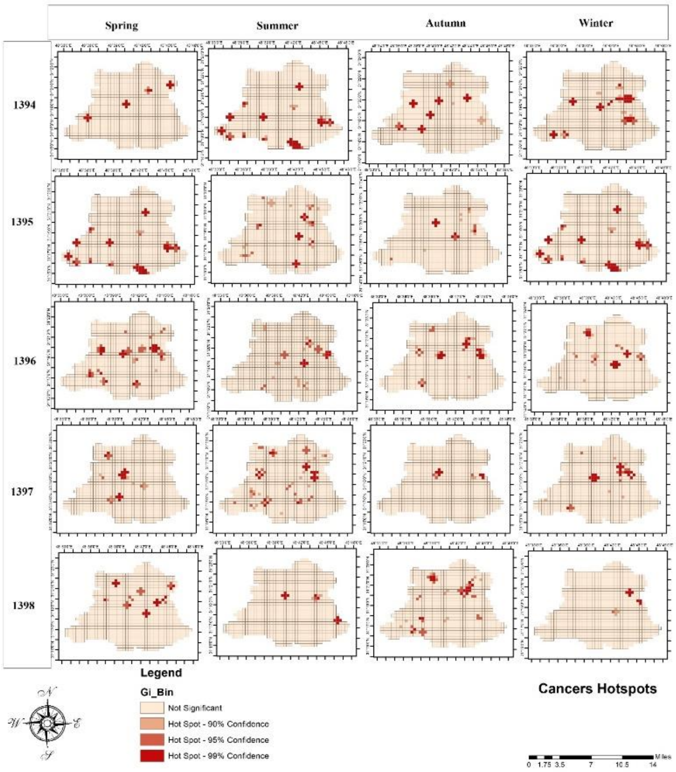

Figure 4: Seasonal hotspot maps of cancer in Ahvaz

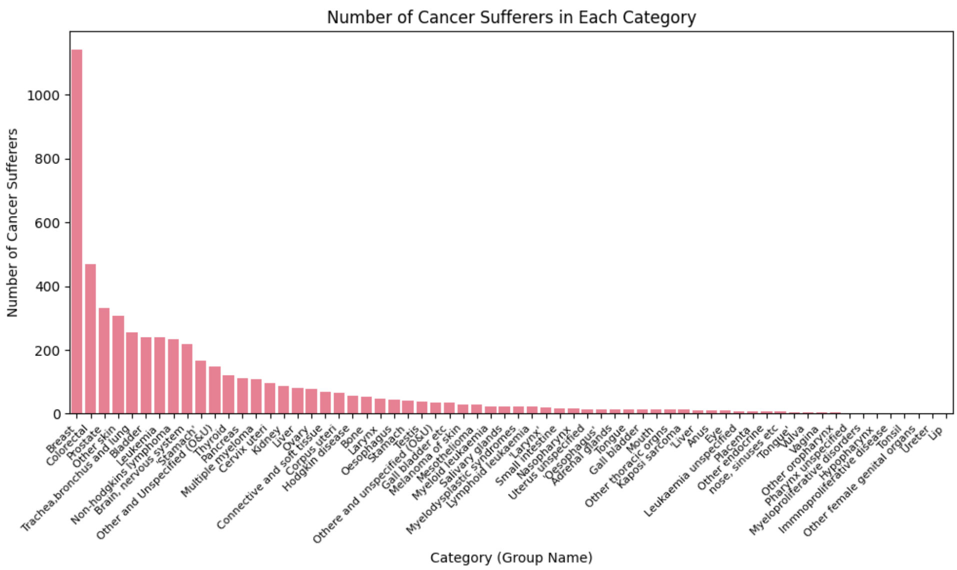

Figure 5: Frequency distribution of cancer types in Ahvaz (2015–2019 / 1394–1398)

5. Conclusion

This study highlights the utility of integrating Geographic Information Systems (GIS) with Python-based analysis to investigate the seasonal and spatial distribution of diseases in an urban environment [4]. Clear seasonal patterns were identified, including elevated incidences of ocular and respiratory diseases during warmer months, increased cardiovascular cases in colder periods, and a relatively stable spatial distribution of cancer throughout the year. High-confidence hotspots were primarily located in the central and eastern districts of Ahvaz, overlapping with regions characterized by elevated pollution levels and high population density [3,4]. These findings emphasize that incorporating spatial analysis into urban health planning can facilitate the identification of high-risk areas, improve the strategic allocation of healthcare resources, and inform evidence-based policies aimed at reducing the public health impacts of air pollution [3,4].

References

1. Ord, J. K., & Getis, A. (1995). *Local spatial autocorrelation statistics: Distributional issues and an application.* Geographical Analysis, 27(4), 286–306.

2. Chen, W., & Chen, X. (2020). *Spatiotemporal analysis of air pollution and health impacts in urban areas.* Environmental Research, 183, 109–118.

3. Hamidi, M., Shamsipour, A., & Daryabari, M. (2025). *A case study of Ahvaz, a highly polluted city*. *Scientific Reports (Nature)*, 15, Article 57634. https://www.nature.com/articles/s41598-025-07634-x

4. Goodarzi, B., Azimi Mohammadabadi, M., Jonidi Jafari, A., & Naddafi, K. (2023). *The spatial distribution of PM2.5 and heavy metals in Ahvaz city. Environmental Monitoring and Assessment*, 195(8), 987–1002. https://www.researchgate.net/publication/374845356

Spatial-Temporal Monitoring of Salt Storms in Lake Urmia Using Satellite Data and Climatic Variables

Ali Sadeghi, Mina Azimipanah*
*Department of Remote sensing & GIS, Faculty of Geography, University of Tehran, Tehran, Iran

Abstract
In recent years, the significant decline in the water level of Lake Urmia has led to an increased frequency of salt storm events, exacerbating environmental and health-related impacts across the region. This study aims to conduct a spatial-temporal analysis of salt storm occurrences within the Lake Urmia, utilizing satellite-derived data and climatic variables. To achieve this, data from MODIS, Landsat-8, and ERA5-Land were employed over the period from 2015 to 2025 by using Google Earth Engine cloud platform. Key indices and parameters, including the Normalized Difference Water Index (NDWI), Modified Normalized Difference Water Index (MNDWI), Land Surface Temperature (LST), Aerosol Optical Depth (AOD) at 0.47 and 0.55 micrometers, and Ångström Exponent (AE), were extracted. Additionally, climatic variables such as wind speed, dominant wind, and wind direction from ERA5-Land datasets were integrated to assess climate conditions influencing the initiation and transport of salt particles. Results indicate that the reduction in the moist surface area of the lakebed, coupled with an increase in Land Surface Temperature, contributes to the development of unstable atmospheric conditions, thereby enhancing the frequency and spatial extent of salt storm impacts. Overall, this study provides critical insights into the pivotal role of diminishing water coverage in Lake Urmia and regional climatic variables in intensifying salt storm frequency. The outcomes of this research hold significant potential for informing strategic planning to mitigate associated health and environmental crises.

Keywords: Salt Storms - Lake Urmia - Remote Sensing - Climatic Variables- Aerosol Optical Depth

1. Introduction
In the last several decades, Lake Urmia has confronted a sharp decline in water level and has been facing a severe crisis, being one of the largest hypersaline lakes in the world and the most important water body in Iran (Sharifi Isaloo, 2025). The main reasons for this reduction include climate change, dam construction, excessive extraction of groundwater, and the expansion of agriculture that uses a great deal of water (AghaKouchak et al., 2015). As a result, large parts of the lakebed have completely dried out and caused salt storms. Salt storms refer to wind-driven movements of saline particles, which develop a serious threat to the environment and public health in this area (Shadkam et al., 2018). In this context, despite several restore attempts, no comprehensive spatiotemporal monitoring and multivariate analysis of these storms, especially at the critical period from 2015 to 2025, has been performed so far. The purpose of this work is to study and monitor salt storms in the Lake Urmia with a multivariate approach based on Landsat-8 satellite imagery, environmental indices, and climatic data.

2. Data and Methods
The study area is Lake Urmia, which is located in northwestern Iran. The lake, about 120 km long and 50 km wide, once covered an area of more than 5,000 km² and was one of the largest permanent hypersaline lakes in the world. Due to the sharp decline in water level, Lake Urmia's desiccated bed has become the primary source of salt storms in the region. This study incorporated both satellite and climatic datasets. Landsat-8 imagery, with a spatial resolution of 30 meters and a 16-day revisit cycle, was used for the calculation of land surface indices. In this respect, MODIS (Terra/Aqua), MCD19A2.061, MODIS Terra and Aqua combined Multi-angle Implementation of Atmospheric Correction (MAIAC) Land Aerosol Optical Depth (AOD), images at 1,000 meters spatial resolution were also used to monitor spatiotemporal variations in surface indices and suspended particulate matter (Lyapustin et al., 2022). The ERA5-Land reanalysis data on daily wind speed and direction with a spatial resolution of 11132 meters were applied to analyze the meteorological conditions that contribute to the formation and transport of salt storms (Muñoz-Sabater et al., 2024). Normalized Difference

Water Index (NDWI) is utilized to identify and distinguish water bodies from non-water surfaces, especially in conditions of significant water-level fluctuation. In the present study, NDWI has been adopted for monitoring the reduction in the water surface area and detecting the gradual trend of drying that Lake Urmia has undergone. This index makes it possible to trace seasonal and annual changes in water extent for long-term periods. Modified Normalized Difference Water Index (MNDWI) ,replaces the Near-Infrared (NIR) band with the Shortwave Infrared (SWIR) band, resulting in a better accuracy for the detection of water in areas with saline or bright sediment surfaces (Xu. H, 2006). In the present research, MNDWI was employed to more precisely separate the water surface from saline and desiccated lakebeds, hence making possible an accurate estimation of the remaining water surface area in Lake Urmia. The land surface thermal condition is represented by Land Surface Temperature (LST). Its rise in arid regions denotes an increase in surface heating, thermal instability, and a rise in the potential for salt particle uplift. In this paper, LST data were used to investigate how the surface temperature over the lakebed is related to the strength of the salt storm events.

$$LST = \frac{K2}{\ln K_1/L_\lambda + 1}$$

Aerosol Optical Depth (AOD) can represent the concentration of atmospheric suspended particles and is widely utilized to assess the intensity and frequency of dust and salt aerosols. This study used daily MODIS data in analyzing the airborne particulate matter emanating from the desiccated bed of Lake Urmia. Ångström Exponent (AE) index works as a quantitative indicator of the relative size distribution of atmospheric aerosols. In general, AOD values are high and AE values are low on salt storm events, reflecting the dominance of coarse saline particles. In this paper, AE was used to discriminate between salt storms and other types of aerosols, such as desert dust or urban pollution (Ångström, 1929).

$$AE = \frac{\log(\frac{AOD_{\lambda_1}}{AOD_{\lambda_2}})}{\log\frac{\lambda_1}{\lambda_2}}$$

Climatic variables, mainly wind speed and direction, are the main factors responsible for the uplift and transportation of saline particles from the desiccated bed of Lake Urmia. Data for the mentioned parameters were taken from the ERA5-Land reanalysis database. Wind data analysis indicates that wind speed represents the main driver of aeolian erosion, while wind direction identifies the main dispersion pathways of the particles. Dominant winds are responsible for the transportation of saline aerosols toward residential areas around the lake. Satellite data processing and analysis were done using Google Earth Engine (GEE), while is a powerful cloud-based platform designed for large-scale processing, analysis, and visualization of remote sensing data.

3. Results

NDWI maps from 2015 to 2025 shows the continued decline of the water surface and the progressive drying of Lake Urmia. The central and southern parts of the lake, with the lowest values of NDWI, have turned into active centers of wind erosion and uplift of salt particles. At the same time, the northern basin, due to the retreat of its marginal waters, has also developed areas with high susceptibility to salt storm formation.

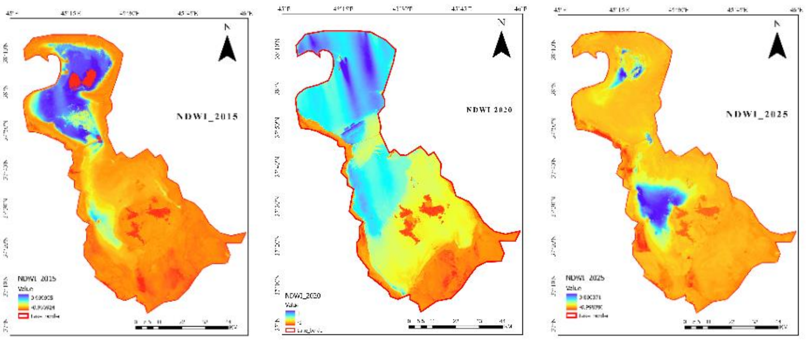

Figure1. NDWI maps of Lake Urmia from 2015 to 2025, showing the decline of water surface and progressive drying.

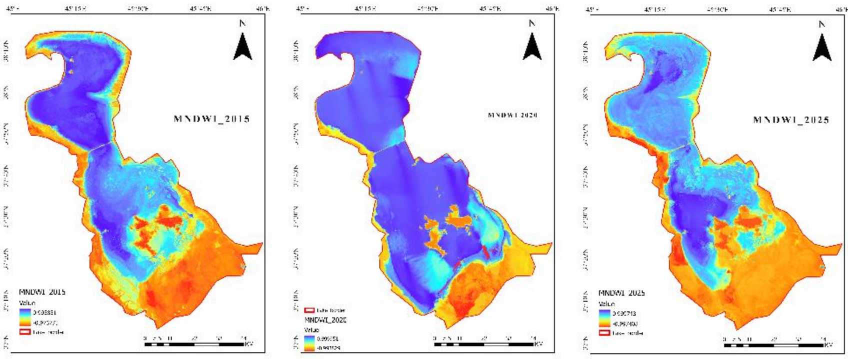

Figure 2. MNDWI maps modified with the SWIR band; accurately delineating the boundary between water and the saline lakebed.

MNDWI mapping from 2015 to 2025 represents the drying trend of Lake Urmia more precisely than NDWI. Negative values of MNDWI point to the expansion of dry and saline areas, mainly in its central and southern parts that have increased rapidly since 2020. On the other hand, the northern basin is relatively stable, though a decrease in surface moisture is also identifiable.

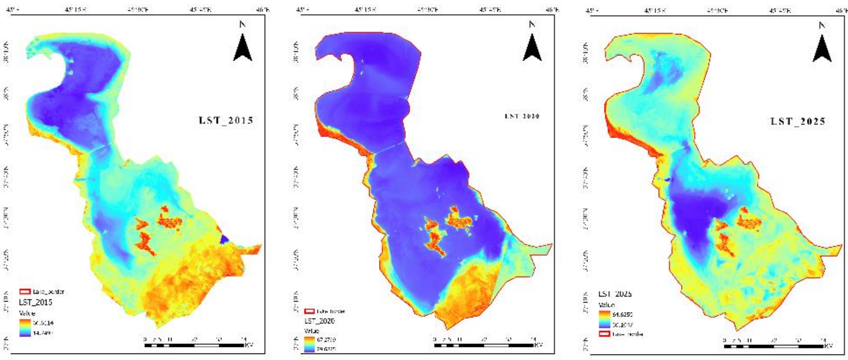

Figure 3**.** Land Surface Temperature (LST) map for the period 2015–2025; a noticeable increase in surface temperature is observed over the dried bed in the central and southern parts of the lake.

Comparison of the LST maps reveals that, in the course of recession, the central and southern regions of Lake Urmia have undergone considerable surface heating. While, in 2015, major parts of it were covered by water and thus showed low temperatures, from 2021 to 2023, when its bed got dry, the surface temperature of these areas reached circa 63-67°C, more than 20°C higher compared to adjacent water bodies. The high surface temperatures of the dry lakebed create strong thermal gradients in the lower atmosphere, enhancing thermal instability and thus allowing for the development of salt storms.The spatial analysis with AOD and AE filters demonstrated the following:

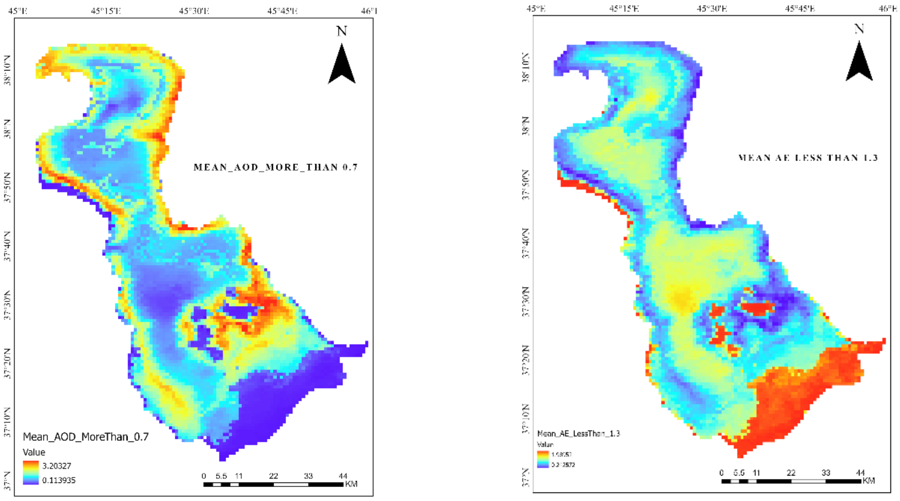

Figure 4. Left: Mean AOD > 0.7 for identifying areas with the highest concentration of suspended saline particles. Right: Mean AE < 1.3, indicating the presence of coarse saline particles in the atmosphere.

In contrast, the mean maps indicate that the primary centers of salt storm activity, with high AOD values >0.7, are located in the southern and central regions of Lake Urmia, especially around the Shahid Kalantari Bridge. Meanwhile, low AE values (<1.3) in these regions illustrate that the aerosols originate within the basin and primarily comprise coarse saline particles, rather than external dust or anthropogenic pollutants. The orientation and frequency of wind directions are analyzed in this section for the study basin to corroborate the role of wind in the transportation of saline particles identified previously by AOD and AE data (Sethi et al., 2021).

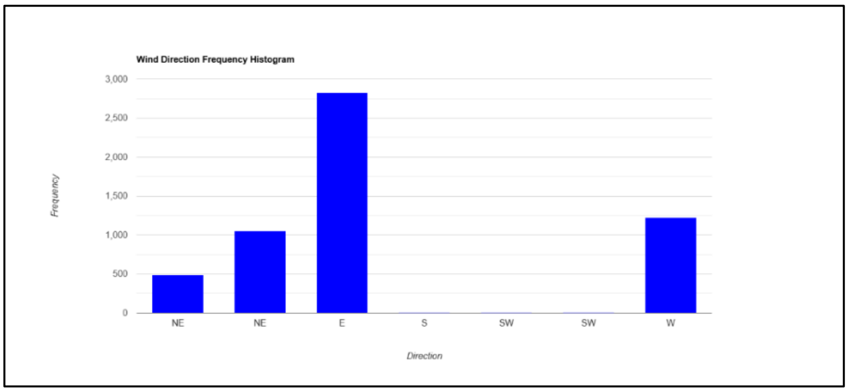

Figure 5. Dominant wind directions in the Lake Urmia over (2015-2025), showing pathways for the transport of saline particles.

The wind direction maps indicate that the easterly winds are the most dominant in the region, followed by westerly and northeasterly winds. The central and southern parts of the dried lakebed are mainly influenced by the prevailing easterly winds, while the northwest tends toward NE winds and the northern and eastern margins show scattered influences of W and NW winds. These patterns delineate the main pathways for the uplift and transport of saline particles.

4. Conclusion

The progressive decline in the water level of Lake Urmia from 2015 to 2025 has resulted in major variations in surface, thermal, and atmospheric characteristics. Increases in LST indicate enhanced thermal instability, which facilitates the uplift of surface particles. Meanwhile, increasing AOD values together with decreasing AE values indicate a strengthening of coarse-grained salt storm activity. The dominant easterly and northeasterly winds will shift these particles to the west and northwest, with impacts on the residential and agricultural areas around the lake. In other words, the crisis of Lake

Urmia is simultaneously generated by three main factors: the saline particle source, thermal instability, and wind forces.

References

1. AghaKouchak, A., Norouzi, H., Madani, K., Mirchi, A., Azarderakhsh, M., Nazemi, A., ... & Hasanzadeh, E. (2015). Aral Sea syndrome desiccates Lake Urmia: Call for action. Journal of Great Lakes Research, 41(1), 307–311.
2. Ångström, A. (1929). On the atmospheric transmission of sun radiation and on dust in the air. Geografiska Annaler, 11(2), 156-166.
3. Lyapustin, A., & Wang, Y. (2022). MODIS/Terra+Aqua Land Aerosol Optical Depth Daily L2G Global 1km SIN Grid V061 [Data set]. NASA Land Processes Distributed Active Archive Center. https://doi.org/10.5067/MODIS/MCD19A2.061 Date Accessed: 2025-11-11.
4. Muñoz Sabater, J., Comyn-Platt, E., Hersbach, H., Bell, B., Berrisford, P., Biavati, G., Horányi, A., Muñoz Sabater, J., Nicolas, J., Peubey, C., Radu, R., Rozum, I., Schepers, D., Simmons, A., Soci, C., Dee, D., Thépaut, J-N., Cagnazo, C., Cucchi, M. (2024): ERA5-land post-processed daily-statistics from 1950 to present. Copernicus Climate Change Service (C3S) Climate Data Store (CDS)
5. Sethi, D., Radhakrishnan, S. R., Sharma, C., Mishra, S. K., & Jaswant. (2021). Aerosol optical properties over Delhi during a dust event in summer 2014: Plausible implications. Indian Journal of Physics, 95(3), 2531–2540.
6. Shadkam, A., Ara, H., Nikou, S., & Zamzami, S. (2018, February). *The effect of Lake Urmia water level decline on the expansion of salt marshes and occurrence of salt storms (Case study: Northeastern Lake Urmia region)*. In *Proceedings of the 4th National Conference on Wind Erosion and Dust Storms*, Yazd, Iran.
7. Sharifi Isaloo, A. (2025). Dryness of Lake Urmia in Iran and its impact on farmers displacement. In *Climate Change Resilience Across Societal Contexts (Energy, Climate and the Environment 32)* (pp. 247–264). Springer.
8. Xu, H. (2006). Modification of normalised difference water index (NDWI) to enhance open water features in remotely sensed imagery. International Journal of Remote Sensing, 27(14), 3025–3033.

Evaluating Connectivity Levels of Public Transportation Stops in Istanbul

Esra Gizem. Uğur[1], Zaide. Duran[2]
[1]Istanbul Technical University, ugure5@itu.edu.tr
[2]Istanbul Technical University, duranza@itu.edu.tr

Abstract
The demand for transportation systems is growing with the increasing population and expanding urban areas, making it essential to improve transportation infrastructure in a more efficient, integrated, and sustainable manner. The integration of transportation systems has great importance in terms of enabling different modes of public transport to operate in harmony, facilitating transfer opportunities, and allowing passengers to travel from one point to another with ease. In this context, various studies have shown that integration increases both user satisfaction and the rate of public transport usage. This integration can be achieved by connecting different public transportation lines and making transfers. This study aims to measure the connectivity levels of the most used and the least used M7 metro stations in Istanbul. The study was conducted in the QGIS environment using open source road network and public transportation stop data. Simplified Connectivity Index (SCI) was developed by considering the speed, passenger capacity, frequency, working hours, and distance to the origin point of all lines that can be accessed within a defined service area for the M7 metro stations accepted as the origin point. As a result of the study, SCIO values were found to be strongly correlated with the number of direct transfers, passenger count, and non-bus stops; moderately correlated with the number of different modes and lines.

Keywords: Connectivity, Accessibility, Public Transportation, GIS, Network Analysis

1. Introduction

The primary issue with car-dependent cities is traffic congestion and the environmental impacts caused by it. The use of private vehicles leads to an increase in greenhouse gas emissions that cause climate change. The time lost due to traffic congestion reduces economic productivity, lowers individuals' quality of life, and negatively affects their health (Miller et al., 2016). Furthermore, it has been determined that the road infrastructures built for automobiles are more costly and have lower economic efficiency than the infrastructure expenditures made for other alternative transportation modes (Schiller et al., 2010).

According to the IMM&ARUP (2022), out of the 4.3 million motor vehicles in Istanbul, 3 million are automobiles. Istanbul, where 153 hours per person are lost annually due to traffic congestion, was ranked as the 4th most congested city in the world. For this reason, traffic congestion is stated to be one of the main factors that reduces quality of life (IMM&ARUP, 2022). When the 2021 emission distribution by sectors in Istanbul is examined as shown in Figure 2.2, 64% of emissions result from energy consumption, 28% from transportation, and 8% from waste production (İbik, 2024). Accordingly, the transportation sector is the second largest contributor to emissions, therefore one of the main causes of air pollution and climate change.

99% of transportation-related greenhouse gas emissions originate from motorized road vehicles, while 1% come from rail and maritime transportation (IMM&ARUP, 2022). The statistics and numerical data provided in the IMM&ARUP (2022) indicate that Istanbul's current transportation system is car-dependent. Miller et al. (2016) examined five studies in the field of sustainable transportation and grouped the main sustainability goals in these studies under four main headings. The four main headings he defined for sustainability goals are as follows: environment, social, economic, and system effectiveness. Since integrated public transportation systems increase network coverage, they improve urban accessibility, encourage the use of public transportation, reduce emissions from private vehicle use, ensure social equity in terms of mobility, provide a more economical transportation method, and increase economic productivity by reducing traffic congestion.

Integration is conducted to increase the number of accessible public transportation locations in ways that are comfortable, safe, fast, and affordable. The shift from private vehicles to public transport will be increased by enabling the integration of multiple lines, increasing passenger capacity, and ensuring the synchronization of modes, thereby improving the efficiency of the system. Initially, the connectivity between two stops was measured through centrality methods based on graph theory. These methods help to quickly and easily analyze the current state of lines and stops; however, since they do not take into account the essential characteristics of public transportation lines, they produce limited results in terms of realism. For this reason, connectivity indices that take into account both the characteristic features of lines and travel demand and that can offer more realistic results have been developed.

Table 1 summarizes key studies that developed node connectivity indices for public transportation networks.

Study	Evaluation Criteria	Node Connectivity Formula
Park&Kang, 2011	Capacity, Speed, Node-Last Stop Distance	$P_{ln} = \alpha . C_l . \beta . V_l . \gamma . D_{ln}$
Mishra et al. 2012	Capacity, Speed, Frequency, Working Hours, Node-Last Stop Distance, Number of Employed People and Households, Transfer Acceptance Rate	$P_{l,n}^o = \alpha . C_l . \beta . V_l . \gamma . D_{l,n} . \delta . A_{l,n} . \varepsilon . T_{l,n}$
Hadas et al. 2013	Speed, Frequency, Walking Distance and Speed, Waiting Time	-
Sarker et al. 2015	Capacity, Speed, Frequency, Working Hours, Node-Last Stop Distance, Number of Employed People and Households	$P_{l,n}^o = \left[\left(\frac{\alpha_l . C_l}{100}\right) . \left(\frac{\beta_l . V_l}{100}\right) . \left(\gamma_l . D_{l,n}^o\right) . \left(\delta_l . A_{l,n}\right)\right]$
Psaltoglou&Calle, 2018	Capacity, Speed, Frequency, Working Hours, Node-Last Stop Distance, Land Use, Street Width, Population Density	$ECI_n^{t1} = CI_n . \left(\frac{A_n^{t1}}{A_{average}}\right)$
Sipetas et al. 2024	Capacity, Speed, Node-Destination Distance	$P_{l,n}^o = \alpha C_l . \beta V_l . \gamma D_{d,n}^o$

Overall, these studies emphasize improving user experience and transit efficiency by integrating service attributes and spatial characteristics into connectivity assessments. When all of the mentioned connectivity indices are examined, it becomes clear that the main indicators are the passenger capacity, speed of the transit vehicle, and the distance between the origin and the destination.

2. Materials and Methods

Within the scope of this study, the area to be analyzed is the M7 Yıldız–Mahmutbey metro line's most used and least used 6 stations. The M7 line, consisting of 17 stations between Yıldız and Mahmutbey (Metro Istanbul, n.d.). In its current form, the M7 metro provides transfers to four different public transportation modes: metro, bus rapid transit (BRT), tram, and bus. Transfers to other lines can be made directly from the Mecidiyeköy, Kağıthane, Alibeyköy, Karadeniz Mahallesi, and Mahmutbey stations. Figure 1 presents information about the lines that can be accessed from M7 stations.

Figure 1. Information on the lines accessible from M7 stations.

According to the dataset titled “Passenger and Passage Numbers by Rail System Stations – 2023”, published on the Istanbul Metropolitan Municipality (IMM) Open Data Platform, the M7 metro line is used by 273.439 passengers daily. Based on this data, approximately 7% of rail system users in Istanbul travel on the M7 line. For all these reasons, the M7 metro line is one of the major rail system lines in Istanbul and was selected as the study area.

In the study, the road network was obtained from OSM (Open Street Map), and the rail system and bus stops were obtained from the IMM Open Data Platform. Data on frequency, speed, passenger capacity, and operating hours of the lines are required. Since passenger capacity and speed vary by mode, not by line, data were gathered from the official websites of IETT for bus and BRT, Metro Istanbul for rail systems, and Istanbul Airport for the M11 metro line operated by TCDD. Passenger capacities were calculated by averaging the values. As operating hours and frequencies vary between lines, they were individually retrieved by querying each line separately through the relevant websites.

The frequency of a public transport line is calculated by dividing the total number of daily trips by the number of daily operating hours. In this study, lines are grouped by frequency and working hours. Figure 2 shows actual frequency values and working hours of lines.

Transit Lines	Frequency Values
Metrobus (BRT)	40
M2 Haciosman-Yenikapi Line	12
M3 Bakirkoy-Kayasehir Line	6
M11 Gayrettepe-Istanbul Airport Line	3
T4 Topkapi-Mescid-i Selam Line	10
T5 Eminonu-Alibeykoy Line	6
Ferry	2

Public Transportation Modes	Working Hours
Metrobus (BRT)	24
Tram (LRT)	18
Metro (M2 and M3)	18
Metro (M11)	19

Figure 2. Actual frequency values and working hours of lines

The criteria addressed in the reviewed connectivity studies were compiled, and the Simplified Connectivity Index ($SCI_{l,n}$) was developed (Uğur, 2025). As the first step in measuring node connectivity, the following evaluation criteria were identified: the speed, capacity, frequency, operating hours of the transit line passing through the stop, and the distance between two stops.

V represents speed, C represents capacity, F represents frequency, H represents operating hours, and D represents distance. “α, β, γ, δ, ε“ are normalization coefficients, defined as the inverse of the total value that each criteria can take. l represents the transit line, n represents node and O represent the destination/origin (which is M7 metro station). Equation 1 represents the measurement method.

$$SCI_{l,n} = \alpha V_l * \beta C_l * \gamma F_l * \delta H_l * \varepsilon D_{n,O} \qquad (1)$$

All the criteria in the $SCI_{l,n}$ index have equal importance, do not directly affect each other, and have quantitative values. Therefore, the criteria weights were assumed to be equal and set to 1.
In this study, İstanbul’s average walking speed was considered to be 1.33 m/s, and the optimal transfer walking time was taken as 8 minutes. Based on these values, walking distance intervals were defined

as 0–4 minutes (0–320 m), 5–8 minutes (321–640 m), and 9–12 minutes (641–960 m). The stops were then classified according to their walking distance from the origin station. Stops located closer to the origin were given higher scores, whereas those located farther away received lower scores. The criteria shown in the equation 1 and the values they can take are presented in Table 2.

A service area analysis was conducted to define walking distances of 320, 640, and 960 meters with the stations of the M7 line were considered as origin points by QGIS. In the second step, metrobus (BRT), bus, tram, and other metro stops within these walking distances were identified. The bus lines passing through these stops were identified by using Google Maps.

The connectivity value of each stop (SCI_s- Stop Simplified Connectivity Index) is calculated by taking the average of the $SCI_{l,n}$ values of all bus lines passing through the selected stop. The average connectivity value of all stops within 960 meters defines the connectivity value of the M7 metro station (SCI_O - Origin Simplified Connectivity Index). Equation 2 calculates the SCI_s values of the stops which are connected to the origin stop, and Equation 3 calculates the SCI_O value of the origin station.

$$SCI_s = \frac{\sum_l^L SCI_{l,n}}{L} \qquad (2), \qquad SCI_O = \frac{\sum_s^S SCI_s}{S} \qquad (3)$$

In the equation 2 and 3, the total number of lines passing through the stop s is defined as L, and the total number of stops within the walking distance of 960 meters is defined as S, and O defines the origin which is M7 metro station.

Table 2. The criteria shown in equation 1 and the values they can take are presented.

Criteria	Criteria Groups	Criteria Values	Criteria	Criteria Groups	Criteria Values
Walking Distance (D)	0-320 m (0-4 min) 321-640 m (5-8 min) 641-960 m (9-12 min)	960 640 320	Frequency (F)	0-3 min (60-20 freq) 4-6 min (19-10 freq) 7-10 min (9-6 freq) 11-15 min (5-4 freq) 16-20 min (3 freq) 20-30 min (2 freq) 30-60 min (1 freq)	20 10 6 4 3 2 1
Passenger Capacity (C)	Bus: 100 Metrobus: 160 Metro and Tram: 1115 Dentur:315 CityLines(Ferry):1650	100 160 1115 315 1650	Working Hours (H)	0-6 Hours 7-12 Hours 13-18 Hours 19-24 Hours	6 12 18 24
Vehicle Speed (V)	Bus and Metrobus: 30 Tram: 20 M11 Metro: 70 Metro: 40 Ferry: 13	30 20 70 40 13			

3. Results

The road network and stop data were used to perform the service area analysis. Taking the six M7 stations as origin points, there are 178 bus stops, 10 rail system stops, 4 BRT stops, and 116 lines located within a 960-meter walking distance. Figure 3 shows the service area analysis.

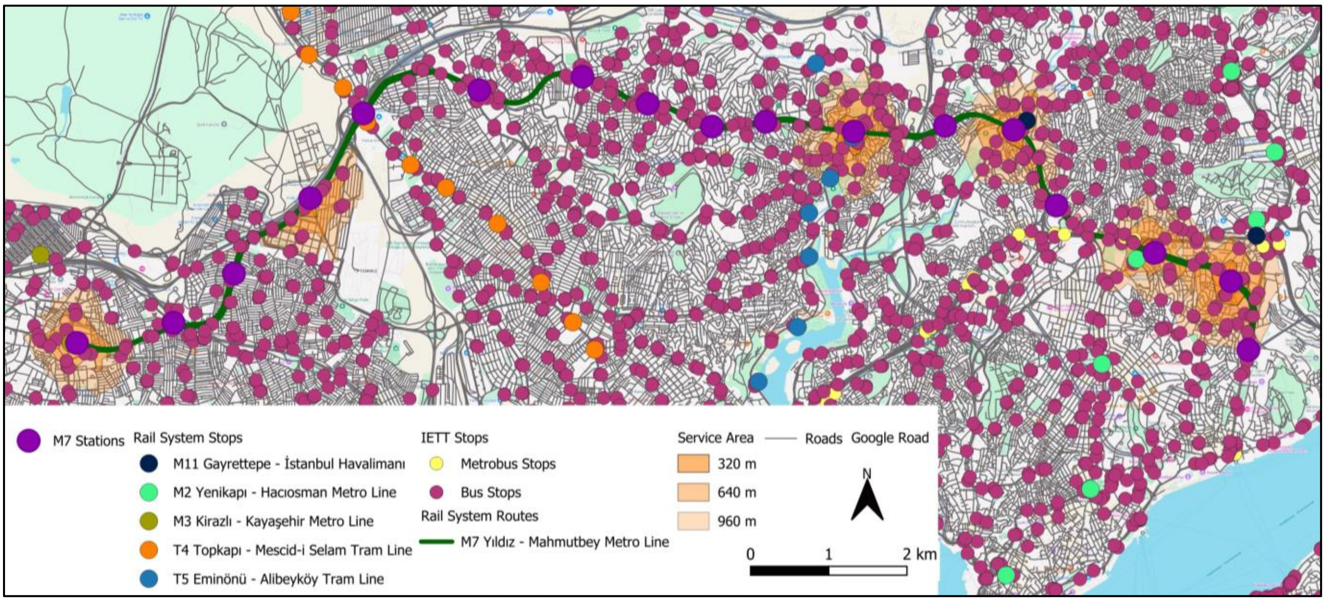

Figure 3. Results of the service area analysis.

After determining the distances between stations and stops through the service area analysis, the connectivity values of nodes of the lines, stops, and M7 stations were calculated by the SCI method. The $SCI_{l,n}$ values of the lines were calculated separately for both outbound and inbound directions. 3 includes information about the SCI_O values, allowing direct transfer, passenger counts, connected stops and lines of the M7 stations. Stations that allow direct transfers were assigned the value of 1, other stations got 0 to compare the direct transfers criteria with the other quantitative criteria.

Table 3. Quantitative criteria.

Station Name	Passenger Count	Direct Transfer	Non-bus Stops	Different Mode	Different Lines	SCI_O Values
Mecidiyekoy	64548	1	4	3	76	0.00010700
Mahmutbey	27547	1	2	2	18	0.00006249
Kagithane	26951	1	2	2	21	0.00005770
Fulya	1707	0	3	3	60	0.00002810
Yildiz	7404	0	0	1	26	0.00001470
Tekstilkent	5001	0	0	1	14	0.00001255

The SCI_O values range from 0.00010700 to 0.00001255. From highest to lowest, the stations are Mecidiyekoy, Mahmutbey, Kagithane, Fulya, Yildiz, Tekstilkent. Although Fulya station is the least used station, it surpasses two other stations because there are metrobus and metro line within walking distance.

The Pearson correlation coefficient between SCI_O values and stations with direct transfer is 0.87; with passenger count, it is 0.97; with the number of non-bus stops, it is 0.81; with the number of different modes, it is 0.67 and with the number of different lines, it is 0.56. SCI_O values have a strong relationship with making a direct transfer, passenger count, the number of stops of modes other than buses. It is found that the SCI_{O} value has a moderate linear relationship with the number of different lines and modes.

4. Conclusion

Within the scope of this study, a method has been developed to easily measure the connectivity levels of stops currently in use or under construction without requiring complex data. The method was applied using the open-source GIS software QGIS. The criteria of the developed $SCIl, n$ index are the passenger capacity, speed, frequency, operating hours of the line, and the distance between two stops. Both direct transfer options and non-bus modes within the service area contribute to higher station connectivity. In addition, the very strong correlation observed between passenger volumes and SCI_{O} values indicates that the developed method effectively captures the level of integration between stations. In further research, the developed index can be expanded by integrating data on land use, population, employment, and income, which determine travel demand, as well as data on transfer ease. This way, the connectivity level can be measured more realistically.

References

[1]Miller, P., de Barros, A. G., Kattan, L., & Wirasinghe, S. C. (2016). Public transportation and sustainability: A review. KSCE Journal of Civil Engineering, 20(3), 1076–1083. https://doi.org/10.1007/s12205-016-0705-0

[2]Schiller, P. L., Bruun, E. C., and Kenworthy, J. R. (2010). An Introduction to Sustainable Transportation: Policy, planning, and implementation, Earthscan, Washington DC.

[3]IMM&ARUP. (2022). Istanbul Sustainable Urban Mobility Plan SUMP.

[4]İbik, T. (2024). Sürdürülebilir Kent İçi Ulaşım ve CO2 Emisyonu: İstanbul İli Örneği. Yönetim ve Ekonomi Dergisi, https://doi.org/10.18657/yonveek.1482257 31(3), 597–622.

[5]Park, J., & Kang, S. C. (2011). A Model for Evaluating the Connectivity of Multi Modal Transit Networks. Transportation Research Board 90th Annual Meeting.

[6]Mishra, S., Welch, T. F., & Jha, M. K. (2012). Performance indicators for public transit connectivity in multi-modal transportation networks. Transportation Research Part A: Policy and https://doi.org/10.1016/j.tra.2012.04.006 Practice, 46(7), 1066–1085.

[7]Hadas, Y. (2013). Assessing public transport systems connectivity based on Google Transit Journal of Transport https://doi.org/10.1016/j.jtrangeo.2013.09.015 Geography, 33, 105–116.

[8]Sarker, A. A., Mishra, S., & Welch, T. F. (2015). A Model Framework for Analyzing Public Transit Connectivity and Its Application in a Large-scale Multi-modal Transit Network. https://www.researchgate.net/publication/313974830

[9]Psaltoglou, A., & Calle, E. (2018). Enhanced connectivity index – A new measure for identifying critical points in urban public transportation networks. International Journal of Critical Infrastructure https://doi.org/10.1016/j.ijcip.2018.02.003 Protection, 21, 22–32.

[10]Sipetas, C., Huang, Z., & Espinosa Mireles de Villafranca, A. (2024). Evaluation Framework for Multi-Modal Public Transport Systems Based on Connectivity and Transfers at Stop Level. Transportation https://doi.org/10.1177/03611981241231963 Research Record.

[11]Metro Istanbul. (n.d.). M7 Yıldız–Mahmutbey metro line. Retrieved May 12, 2025, from https://www.metro.istanbul/Hatlarimiz/HatDetay?hat=M7

[12]Uğur, E. G. (2025, June). Assessing connectivity levels of public transportation stops: A case study of Istanbul [Master's thesis, Istanbul Technical University]. Council of Higher Education Thesis Center. https://tez.yok.gov.tr/UlusalTezMerkezi/

PROCEEDINGS BOOK OF THE10th INTERCONTINENTAL GEOINFORMATION DAYS

29 - 30 NOVEMBER 2025

Tehran, IRAN

MERSIN UNIVERSITY - ENGINEERING FACULTY
DEPARTMENT OF GEOMATICS ENGINEERING

ISBN: 978-625-5604-32-3